FACULTY OF ENGINEERING
AND ARCHITECTURE

Ultra-Compact and Low-Threshold Nano-Ridge Lasers Epitaxially Grown on Silicon

Zhongtao Ouyang

Doctoral dissertation submitted to obtain the academic degree of
Doctor of Photonics Engineering

Supervisors
Prof. Dries Van Thourhout, PhD - Prof. Geert Morthier, PhD
Department of Information Technology
Faculty of Engineering and Architecture, Ghent University

August 2025

GHENT
UNIVERSITY

ISBN 978-94-93464-11-7
NUR 926, 959
Wettelijk depot: D/2025/10.500/71

Members of the Examination Board

Chair

Prof. Filip De Turck, PhD, Ghent University

Other members entitled to vote

Prof. Zeger Hens, PhD, Ghent University
Prof. Yuqing Jiao, PhD, Technische Universiteit Eindhoven, the Netherlands
Prof. Huiyun Liu, PhD, University College London, United Kingdom
Prof. Günther Roelkens, PhD, Ghent University

Supervisors

Prof. Dries Van Thourhout, PhD, Ghent University
Prof. Geert Morthier, PhD, Ghent University

Acknowledgements

Reflecting on the past five years of my research and life in Ghent, countless unforgettable memories come to mind. This period has profoundly shaped my understanding of what I need in life and the person I aspire to become.

I feel fortunate to have been part of the Photonics Research Group, a family bound by shared purpose and mutual support. In Chinese Taoist culture, this connection is often seen as destiny—a thread linking people, events, and opportunities. With this in mind, I want to express my heartfelt gratitude to everyone who has been part of my journey.

All began with an interview with my promoter, Prof. Dries Van Thourhout. Before the interview, I was a mix of excitement and nerves. It marked the gateway to a new world—a foreign land, a different language, and a once-in-a-lifetime opportunity. I vividly remember Dries's stern expression as he posed challenging questions. At that moment, he seemed like an immovable obstacle, though in reality, he is quite slim. Despite my less-than-stellar performance, I was fortunate to receive his offer, a turning point in my life.

Working with Dries has been an inspiring experience. His confidence, dedication to science, and genuine care for his students left a lasting impression. Contrary to the notion that he is a man of few words, I found him to be warm and humorous, often sharing jokes and funny emotions that helped us bond. These small moments transformed our professional relationship into a genuine friendship.

Dries has been instrumental in my development, both technically and personally. Beyond imparting research skills, he taught me the importance of confidence. His insights at critical moments and guidance toward other resources were invaluable. Whenever I knocked on his door with questions, he would stop his work to offer clear and thoughtful answers. Thank you, Dries, for your time and mentorship. Working under your supervision has been an exceptional experience.

The challenging nano-ridge project was made manageable thanks to the support of the IMEC team. Bernardette, your exceptional nano-ridges were the foundation of many of our projects. Our brief but lively discussions inspired me to appreciate the significance of our work.

To all the professors in the Photonics Research Group, thank you for fostering a thriving research community. Your contributions have made the group stronger and more renowned. In the cleanroom, Steven, Liesbet, and Muhammad, your guidance during training helped me fabricate functional lasers. Clemens, your ability to resolve any lab issue was truly magical. To my colleagues, your friendly conversations and camaraderie brought joy to both my work and life in Ghent.

My Chinese colleagues provided invaluable support throughout this journey. Yanlu, Haolan, Jing, Yuting, and Yujie, your shared experiences eased my transition into the Ph.D. program. To Biwei, Yujie, Xiujun, Yang, TingTing, Yufei, Chonghuai, Xiangfeng, Hong, Chupao, Xin, Chenming, and others, thank you for the warmth of shared moments—whether through badminton, swimming, Chinese food parties, or travel. These connections made living nearly 10,000 km away from home warm and more comforting.

I am also grateful to my friends Yiping, Chao, Luis, Jacob, Nacho, Marina, and my roommates Ziqi, Baihong, Yumiao, Wenbin, Jiangfeng and Zhiheng, for giving me a sense of belonging and enriching my life in Ghent.

Lastly, my deepest gratitude goes to my family. To my wife, thank you for your unwavering support, patience, and sacrifices during these six years apart. To my parents, thank you for your unconditional love and for giving me the freedom to pursue my dreams. To my younger brother, thank you for your advice, support, and for helping with family matters during challenging times.

Gent, May 2025
Zhongtao Ouyang

Contents

List of Figure

List of Table

List of Acronyms

A

AFM	Atomic Force Microscope
APBs	Antiphase Boundaries
ART	Aspect Ratio Trapping
aSi	Amorphous Silicon

B

BCB	Benzocyclobutene

C

CES	Consumer Electronics Show
CMOS	Complementary Metal-Oxide-Semiconductor
Cryo.	Cryogenic Temperature
CW	Continuous-Wave

D

DBR	Distributed Bragg Reflector
DFB	Distributed Feedback

DI Water	Deionised Water

E

EBL	Electron-Beam Lithography
EL	Electroluminescence
ELO	Epitaxial Lateral Overgrowth
Er	Erbium

F

FDE	Finite Difference Eigenmode
FIB-SEM	Focused Ion Beam - Scanning Electron Microscopy
FOM	Figure of Merit
FP	Fabry-Pérot

G

GaAs	Gallium Arsenide
Ge	Germanium

H

HSQ	Hydrogen Silsesquioxane

I

ICP-RIE	Inductively Coupled Plasma Reactive Ion Etching
In	Indium

InGaAs	Indium Gallium Arsenide
IPA	Isopropyl Alcohol

K

KOH	Potassium Hydroxide

L

LART	Lateral Aspect Ratio Trapping
$LiNbO_3$	Lithium Niobate

M

MOCVD	Metal-Organic Chemical Vapor Deposition
MOVPE	Metal-Organic Vapor Phase Epitaxy

N

NRE	Nano-Ridge Engineering

O

OEICs	Opto-Electronic Integrated Circuits
QSFP	Quad Small-Factor Pluggable

P

PC	Photonic Crystal
PECVD	Plasma-Enhanced Chemical Vapor Deposition
PICs	Photonic Integrated Circuits

PL	Photoluminescence
PZT	Lead Zirconate Titanate

Q

QD	Quantum Dot
QW	Quantum Well

R

R.T.	Room Temperature
RIE	Reactive Ion Etching

S

Si PICs	Silicon Photonic Integrated Circuits
SAG	Selective Area Growth
SEM	Scanning Electron Microscope
SG	a grating on the side of the nano-ridges / sidewall grating
SGL	the sidewall grating laser cavity
SiN_x	Silicon Nitride
SiO_x	Silicon Oxide
SMSR	Side-Mode Suppression Ratio
SoC	System-On-Chip
SOI	Silicon-On-Insulator

T

TASE	Template-Assisted Selective Epitaxy
TDD	Threading Dislocation Density
TDs	Threading Dislocations
TMAH	Tetramethylammonium Hydroxide
TRPL	Time-Resolved Photoluminescence
TG	a grating on top / top grating
TGL	top grating laser cavity

V

VCSELs	Vertical-Cavity Surface-Emitting Lasers
VLSI	Very-Large-Scale Integration

Samenvatting

1 Introductie

Silicium gebaseerde fotonische geïntegreerde circuits die diverse optische componenten zoals hoog-efficiënte roosterkoppelingen, snelle fotodetectoren en geavanceerde modulatoren op een gemeenschappelijk substraat combineren, worden op dit moment uitgebreid bestudeerd en toegepast in verschillende technologische domeinen. Voor hun realisatie wordt gebruik gemaakt van de goed ontwikkelde processen uit de halfgeleiderindustrie wat ze kostenefficiënt maakt. Ondanks de enorme vooruitgang in het onderzoeksveld blijft het ontbreken van een hoogwaardige geïntegreerde laser een belangrijke belemmering voor verdere ontwikkeling van silicium gebaseerde fotonische chips. III-V halfgeleiders met een directe bandgap zijn veelbelovende kandidaten voor de realisatie van een praktische en compacte lichtbron, maar de integratie ervan op silicium blijft een uitdaging vanwege het grote vershil in roosterconstante. Verschillende hybride en heterogene integratietechnieken, zoals flip-chip bonding, wafer bonding en transfer printing, worden onderzocht om deze uitdaging aan te pakken. Hoewel deze methoden toepasbaar zijn voor een breed scala aan materialen en componenten, introduceren ze extra processtappen, wat de compatibiliteit met bestaande productieprocessen beperkt.

Een veelbelovend alternatief is de hetero-epitaxiale groei van III-V materialen op silicium. Geavanceerde technieken zoals oppervlaktereconstructie, Ge/GeSi virtuele substraten, defectfilterlagen en lokale groeimethoden zijn voorgesteld om defecten te minimaliseren. Imec stelde recent een alternatieve aanpak voor, de nano-ridge engineering techniek, die de groei van hoogwaardige III-V materialen op silicium met een dunne bufferlaag mogelijk maakt, wat voordelen biedt op het gebied van schaalbaarheid, integratiedichtheid en kosten.

Binnen eerder onderzoek binnen onze groep werden reeds distributed feedback (DFB) lasers gedemonstreerd met geëtste roosters en metalen roosters, die optisch gepompt werden. Echter, deze caviteiten vertoonden een lage koppelingsefficiëntie, waardoor lange caviteiten ($>$100 µm) en hoge laserdrempels nodig waren. Dit proefschrift richt zich op innovatieve laserontwerpen om deze beperkingen aan te pakken, met de nadruk op het verkleinen van de lengte van de caviteit en het verlagen van de laserdrempels, wat de integratie van de lasers met hoge dichtheid mogelijk maakt, en tot een laag energieverbruik zou moeten leiden.

2 Resultaten

Ons werk richtte zich op de ontwikkeling van compacte, laagdrempelige optisch gepompte nano-ridge lasers. Voortbouwend op eerder onderzoek naar de optische eigenschappen van nano-ridge materialen, hebben we met succes een λ/4-verschoven, index-gekoppelde distributed feedback (DFB) laser met een amorfe silicium (aSi) rooster gedemonstreerd. Dit ontwerp behaalde een onderdrukking van de zijmodes van $>$35 dB en een laserdrempel van 7,84 kW/cm^2 voor 130 µm lange caviteiten. Deze drempel is ongeveer vijf keer lager dan die van apparaten met een geëtst rooster binnen de nano-ridge. De verlaagde drempel is te danken aan het vermijden van verliespaden voor de ladingsdragers, veroorzaakt door oppervlakte-defecten en plasma-geïnduceerde schade, die inherent zijn aan het fabricageproces van geëtste roosters.

Om de voetafdruk verder te minimaliseren, hebben we een nieuw compact lasercaviteitsontwerp ontwikkeld waarbij een aSi-roosterkoppeling aan de zijkanten van de nano-ridge wordt geïntegreerd, in plaats van op de bovenkant. Deze innovatieve configuratie maakt nauwkeurige controle mogelijk over de interactie tussen de lasermodus en het rooster, waardoor fijnafstemming van zowel de nano-ridge breedte als de roosterdikte mogelijk is voor het bereiken van hoog-Q factor resonanties, zelfs in caviteiten van slechts 20 µm.

In tegenstelling tot conventionele geëtste roosters, die vaak leiden tot materiaaldegradatie, behoudt ons gedeponeerde aSi-rooster de structurele integriteit, wat zorgt voor stabiele optische prestaties. Onder gepulste optische pompwerking werd een laserdrempel van $\sim$ 9.9 kW/cm^2 gemeten voor een DFB-laser met een compacte 16 µm caviteit (100 perioden). De emissiespectra bevestigden éénmoduswerking, met een zijmodussuppressieverhouding van meer dan 24 dB.

Daarnaast werd een apodized fotonicakristalcaviteit met geëtste gaten door de gehele nano-ridge voorgesteld om de laserdrempels verder te verlagen en de voetafdruk te verkleinen. Het fabriceren van diepgeëtste fotonicakristalcaviteiten brengt specifieke uitdagingen met zich mee, met name bij het bereiken van nauwkeurige etsing en effectieve passivering van de actieve regio. Diepe etsing door de nano-ridge vereist zeer gecontroleerde gasstroomdynamiek, aangezien het proces extreem gevoelig is voor milieuvariaties in hoog-aspect-verhouding gaten (geëtste diepte/gatdiameter). Door geoptimaliseerde ICP-etskracht, RF-kracht, kamerdruk en gasstromen, werden verticale zijwandgaten met succes gefabriceerd via een complex etsenrecept.

Ondanks het behalen van nauwkeurige etsing, faalden passiveringsexperimenten met $(NH_4)_2S$—uitgevoerd onder verschillende temperaturen, concentraties en blootstellingstijden—in het volledig herstellen van de schade aan kwantumputten veroorzaakt door het etsproces, wat uiteindelijk de optische efficiëntie beïnvloedde. Dit leidde tot verdere verkenning van ondiepe fotonicakristalontwerpen, die een betere kwantumputintegriteit bieden, terwijl de effectieve lichtopsluiting behouden blijft. Toch werd met het diep etsen proces met succes fotonicakristal spiegels met hoge reflectiviteit gedefinieerd, wat een sterke potentie aantoont voor fotonverzameling in enkele-foton lichtbronnen.

Latere ontwerpen maakten gebruik van ondiepe etsing, waarbij werd gestopt bij de eerste kwantumputlaag zonder diepere lagen te penetreren, om de actieve regio te behouden. Een indiumrijke kwantumputstructuur werd gekozen om O-band werking mogelijk te maken. Dit ontwerp ondersteunde O-band lasing met een 25 µm caviteit, een laserdrempel van 11,83 kW/cm^2, een zijmodussuppressieverhouding van 17 dB. Onder gepulste optische pompwerking werd een drempel van slechts 5,03 kW/cm^2 bereikt voor een 103 µm lange caviteit.

3 Conclusie en Toekomstperspectief

Dit PhD-onderzoek heeft met succes de ontwikkeling van drie geavanceerde nano-ridge lasers aangetoond, monolithisch geïntegreerd op 300 mm siliciumsubstraten, waarbij lage laserdrempels en compacte afmetingen zijn gerealiseerd onder optische pompwerking. Door gebruik te maken van hoogwaardige nano-ridge materialen van imec, werden de belangrijkste uitdagingen in III-V laserintegratie aangepakt, wat heeft geleid tot efficiënte lichtopsluiting. Bovendien verbeterde de introductie van amorfe siliciumroosters de optische terugkoppeling en verkleinde het de caviteitsvoetafdruk, terwijl oppervlakterecombinatie werd geminimaliseerd en schade aan kwantumputten werd voorkomen. Recentelijk is ook lasing onder elektrische injectie gedemonstreerd voor nano-ridge gebaseerde apparaten. Echter, de zwakke terugkoppeling in deze apparaten resulteerde in caviteiten van 1–2 mm, wat onpraktisch is voor compacte integratie. De hoogcontrast-roosters die in ons werk worden geïntroduceerd, bieden een veelbelovende oplossing voor aanzienlijk compactere elektrisch geïnjecteerde apparaten. Daarnaast heeft de implementatie van apodized fotonicakristalcaviteiten sterke potentie getoond voor het realiseren van hoog-Q, ultracompacte apparaten, terwijl de kwantumputintegriteit behouden blijft. Deze vooruitgang markeert een belangrijke mijlpaal richting schaalbare en CMOS-compatibele laserintegratie voor siliciumfotonica-platforms.

Ondanks deze successen blijven er technische uitdagingen bestaan. Het realiseren van continue-golfwerking, efficiënte elektrische injectie en verbeterde prestaties in de O-band zijn cruciaal voor de praktische toepassing van deze lasers. Toekomstig onderzoek zou zich moeten richten op het optimaliseren van ladingsinjectieschema's, het verbeteren van thermisch beheer en het verfijnen van passiveringstechnieken om de kwantumputkwaliteit tijdens fabricage te waarborgen. Het aanpakken van deze obstakels is essentieel voor het ontwikkelen van volledig geïntegreerde, hoogwaardige lichtbronnen, geschikt voor next-generation optische communicatienetwerken en dichte fotonisch-elektronische co-packaged systemen. Dit onderzoek vormt de basis voor het volledig benutten van epitaxiale nano-ridge lasers binnen grootschalige siliciumfotonica-productie, en zal toekomstige innovaties in optische integratie en schaalbare fotonicatechnologieën stimuleren.

Summary

1 Introduction

Leveraging well-developed processes from the complementary metal-oxide semiconductors (CMOS) industry, silicon photonics circuits incorporating various optical components, including high-efficiency grating couplers, high-response-speed photodetectors and excellent modulators are now widely studied and used in a variety of applications. However, the absence of a high-performance on-chip laser remains a significant bottleneck in the further development of silicon photonics platforms. Direct-bandgap III-V semiconductors are promising candidates for realizing a practical and compact light source but not easy to integrate on silicon due to their large lattice mismatch. Several hybrid and heterogeneous integration techniques—such as flip-chip bonding, wafer bonding, and transfer printing—have been explored to address this challenge. Although these methods are applicable to a broad range of materials and devices, they introduce additional processing steps, complicating the integration and limiting the compatibility with large-scale production processes.

III-V heteroepitaxial growth on silicon presents an attractive alternative. Advanced techniques such as surface reconstruction, relaxed graded Ge/GeSi virtual substrates, defect filter layers, and growth in small regions have been used to minimize defects. Among these, imec's nano-ridge engineering technique combining with ART enables high-quality III-V material growth on silicon with a thin buffer layer, offering scalability, integration density, and cost advantages.

Previous work in our group already demonstrated distributed feedback (DFB) lasers with etched gratings and metal gratings, operating under optical pumping. However, these devices exhibited low coupling coefficients, requiring long cavities ($>$100 µm) and high lasing thresholds. This thesis explores innovative laser designs to address these limitations, focusing on reducing cavity size and lasing thresholds and thereby allowing for high-density integration and low energy consumption.

2 Results

Our work aimed to develop compact, low-threshold optically pumped nano-ridge lasers. Building on previous research into the optical properties of nano-ridge materials, a $\lambda/4$-shifted, index-coupled DFB laser with an amorphous silicon grating (aSi) was demonstrated. This design achieved a side-mode suppression ratio >35 dB and a lasing threshold of 7.84 kW/cm^2 for 130 µm cavities. This threshold is approximately five times lower than that of devices using an etched grating within the nano-ridge. The reduced threshold results from avoiding carrier loss paths caused by surface defects and plasma-induced damage inherent in the fabrication of etched gratings.

To further minimize the footprint, we developed a new approach for realizing a compact laser cavity by integrating an aSi grating at the sides of the nano-ridge rather than placing it on top. This innovative configuration allows for precise control over the interaction between the lasing mode and the grating. The fine-tuned adjustments in nano-ridge width and grating thickness facilitate the realization of high-Q factor resonances, even in cavities as small as 20 µm.

Unlike conventional etched gratings, which often degrade material quality, our deposited aSi grating preserves structural integrity, ensuring stable optical performance. Under pulsed optical pumping, a lasing threshold of $\sim$ 9.9 kW/cm^2 was measured for a DFB laser with a compact 16 µm cavity (100 periods). The emission spectrum confirmed single-mode operation, achieving a side-mode suppression ratio exceeding 24 dB.

Finally, an apodized photonic crystal cavity incorporating holes etched through the nano-ridge was proposed to further lower lasing thresholds and reduce footprint. Fabricating deep-etched photonic crystal cavities presents distinct challenges, particularly in achieving precise etching and effective passivation of the active region. Deep etching through the nano-ridge requires highly controlled gas flow dynamics, as the process is extremely sensitive to environmental variations in high-aspect-ratio holes (etched depth/hole diameter). Through optimized ICP etching power, RF power, chamber pressure, and gas flow, vertical sidewall holes were successfully fabricated using a complex etching recipe.

Despite achieving accurate etching, passivation experiments using $(NH_4)_2S$—conducted across various temperatures, concentrations, and exposure times—failed to fully reverse quantum well damage caused by the etching process, ultimately impacting optical efficiency. This finding led to further exploration of shallower photonic crystal designs, offering improved quantum well integrity while maintaining effective light confinement. Nevertheless, the deep etching process successfully defined photonic crystal mirrors with high reflectivity, demonstrating strong potential for photon collection in single-photon light sources.

Subsequent designs utilized shallow etching, terminating at the first quantum well layer without penetrating any quantum well layers, to preserve the active region. An indium-rich quantum well structure was chosen, to allow for O-band operation. This design enabled O-band lasing with a 25 µm cavity, a lasing threshold of 11.83 kW/cm^2, a side-mode suppression ratio of 17 dB. Under pulsed optical pumping, a threshold as low as 5.03 kW/cm^2 was achieved for a 103 µm long cavity.

3 Conclusion and perspective

This PhD. research successfully demonstrated the development of three advanced nano-ridge lasers, monolithically integrated on 300 mm silicon substrates, achieving low lasing thresholds and compact footprints under optical pumping. By utilizing high-quality nano-ridge material from imec, we effectively addressed key challenges in III-V laser integration, enabling efficient light confinement. Additionally, the introduction of amorphous silicon gratings significantly enhanced optical feedback and reduced cavity footprint, while minimizing surface recombination and avoid damage to quantum wells. Recently, also lasing under electrical injection was demonstrated for nano-ridge based devices. However, the weak feedback in these devices resulted in a cavity length of 1-2 mm, which are impractical for compact integration. The high-contrast gratings introduced in our work provide a promising solution for significantly more compact electrically injected devices. Furthermore, the implementation of apodized photonic crystal cavities demonstrated strong potential for achieving high-Q, ultra-compact devices, while preserving the quantum well. These advancements mark a major milestone toward scalable and CMOS-compatible laser integration for silicon photonic platforms.

Despite these achievements, several challenges remain. Continuous-wave operation, efficient electrical injection, and enhanced performance in the O-band are crucial for enabling practical deployment in real-world applications. Future research should focus on optimizing carrier injection schemes, improving thermal management strategies, and refining passivation techniques to maintain quantum well quality during fabrication. Addressing these challenges will be essential to realizing fully integrated, high-performance light sources, suitable for next-generation optical communication networks and dense photonic-electronic co-packaged systems. Ultimately, this research lays the foundation for unlocking the full potential of epitaxial nano-ridge lasers in high-volume silicon photonics manufacturing, driving future innovations in optical integration and scalable photonic technologies.

1

Introduction

Information technology is a critical driver of economic and social development. Ultra-large-scale, high-performance silicon-based microelectronic chips play a pivotal role in processing vast amounts of data. However, as the feature sizes of electronic components continue to shrink and the demand for highly functional chips grows, traditional electrical interconnections face significant limitations. These include increased electrical resistance and capacitance, which lead to time delays in high-speed operations, and crosstalk between neighboring wires [1,2]. To address these challenges, a transformative approach to interconnection technology is required. Optical interconnections have emerged as a promising alternative, leveraging photons to transmit and process information, thereby overcoming the constraints of electrical interconnections [3].

Silicon photonic integrated circuits (Si PICs), which employ optical components on silicon substrates, have been under investigation for decades. They benefit from the mature complementary metal-oxide-semiconductor (CMOS) manufacturing processes originally developed for the electronics industry. The potential applications of Si PICs extend beyond interconnections to fields such as telecommunications, imaging, sensing, and neural networks [4, 5].

This chapter introduces the key passive and active photonic components in Si PICs in Subsection 1.1.1. It then addresses the primary obstacle to their widespread commercialization—the lack of practical on-chip light sources. Subsection 1.1.2 explores various materials and methods for achieving on-chip light emission, along with their respective limitations. Subsection 1.1.3 reviews integration approaches for incorporating III-V materials onto silicon substrates, including flip-chip bonding, micro-transfer printing, and heteroepitaxy. The discussion also covers different III-V epitaxial growth techniques, with a focus on direct growth on silicon substrates using thin buffer layers as the main integration method in this thesis. Finally, Section 1.2 and Section 1.3 outline the objectives and structure of the thesis, while Section 1.4 lists my relevant publications.

1.1 Research background

1.1.1 Components in Si PICs

The monolithic integration of silicon photonic components onto chips with fast, very-large-scale integration (VLSI) silicon microelectronics inspired the development of opto-electronic integrated circuits (OEICs). Conceived in the mid-1980s, early research on Si photonics focused on waveguides and electro-optical switches [6, 7]. By the early 2000s, innovations accelerated, leading to breakthroughs such as ultra-low-loss waveguides, high-efficiency grating couplers, high-gain amplifiers, high-speed modulators, and high-performance photodetectors, showcasing the immense potential of silicon-based photonics.

1.1.1.1 Ultra-Low-Loss Waveguides

Similar to high-performance electrical wires in electronics, low-loss photon channels—waveguides—are fundamental in photonic integrated circuits (PICs). Decades of effort have prioritized reducing waveguide loss through two primary methods. The first method optimizes fabrication to smooth waveguide sidewalls and minimize roughness [8–12]. For instance, an etch-less process using selective thermal oxidation achieved a low loss of 0.3 dB/cm [9]. The second method reduces optical mode interaction with rough sidewalls, as seen in silicon-on-insulator (SOI) ridge waveguides with 50 nm etching depths, achieving 0.274 dB/cm loss [13] or in multimodal waveguides. A recent spiral waveguide on a 200-nm SOI platform demonstrated 0.28 dB/cm loss over 100 cm with a 10 µm bending radius [14].

1.1.1.2 Grating Couplers and Multiplexing

Advancements in silicon waveguides have enabled the development of critical PIC components, such as fiber-to-chip grating couplers. In 2015, an apodized design with optimized parameters like grating period, fill factor, and buried oxide thickness, incidence angle, achieved -0.7 dB coupling efficiency [15].

To address higher data transmission demands, multiplexing techniques such as wavelength-division multiplexing (WDM) [16], polarization-division multiplexing (PDM) [17] mode-division multiplexing (MDM) [18], as well as hybrid methods like MDM-WDM [19] and MDM-PDM [20] have been implemented. An example is the WDM receiver chip of [16], which yielded a 25-channel silicon nanowire arrayed waveguide grating (AWG) with 1.25 Tb/s total capacity at 50 Gb/s per channel.

1.1.1.3 Amplifiers and Modulators

As Si PICs scale, passive device insertion loss becomes a critical challenge. Optical amplifiers address this issue effectively. III-V/Si semiconductor optical amplifiers integrated via die-to-wafer bonding have achieved over 27 dB small-signal gain and 17.24 dBm saturation power [21]. Monolithic quantum dot (QD) amplifiers deliver similar gains with an expanded 120 nm amplification bandwidth [22].

High-performance optical modulators are essential for Si PICs, requiring high speed, efficiency, and low power consumption. Traditional electro-optic effects are weak in silicon [23, 24], prompting exploration of plasma dispersion and thermo-optic effects, as well as wafer-scale integration of alternative materials [25]. Recent advances include a $LiNbO_3$(Lithium Niobate)-on-insulator modulator with 100 GHz bandwidth and sub-0.5 dB loss [26–28], and PZT(Lead Zirconate Titanate)-integrated silicon nitride photonic circuits featuring 33 GHz bandwidth and 1 dB/cm loss [29].

1.1.1.4 Extended Wavelength Detection

Extending Si photonics to the 1.55 µm telecom band has been challenging due to the 1.1 µm cutoff of silicon photodetectors. Germanium photodiodes have addressed this, offering 265 GHz 3 dB bandwidth, 0.3 A/W responsivity, and low dark currents [30]. III-V photodetectors grown on silicon via lateral epitaxy demonstrate responsivities of 0.4 A/W at 1.3 µm and 0.2 A/W at 1.5 µm, covering the telecom band [31].

1.1.2 Noteworthy commercial products

The translation of research into industry has enabled Si photonics to impact diverse fields. In 2019, NVIDIA acquired Mellanox for $6.9 billion to expand its InfiniBand and Ethernet product lines [32]. NVIDIA Mellanox now offers QSFP transceivers with 400 Gb/s capacity, supporting data communication over single-mode fibers up to 2,000 meters and multimode fibers up to 50 meters [33].

Si photonics is also gaining traction in autonomous driving through its application in LiDAR systems. These systems are valued for their accurate long-distance measurement, high-resolution imaging and all-weather operation. In 2021, Mobileye, a subsidiary of Intel, showcased its new Si photonics LiDAR system-on-chip (SoC) at the All-Virtual Consumer Electronics Show (CES) [34]. The company demonstrated self-driving vehicles navigating Paris landmarks like the Eiffel Tower and Galeries Lafayette [35]. Mobileye's CEO, Amnon Shashua, announced that the LiDAR SoC is expected to be used in millions of autonomous vehicles, referring to the chip as an ”on-chip silicon photonic circuit” at the time.

Other notable products include Cisco's Dense Wavelength-Division Multiplexing (DWDM) Network Convergence System [36] and Sicoya's 400 G DR4 Engine, which integrates advanced modulators and photodiodes [37]. These innovations illustrate Si photonics' transformative potential across industries.

1.1.3 The 'Holy Grail': Lasers in Si PICs

Over the past decades, advancements in silicon photonic components have significantly matured silicon photonic platforms. However, silicon's indirect bandgap presents a major challenge for efficient stimulated emission, hindering large-scale commercialization. Consequently, developing a practical, efficient on-chip laser has been termed the ”holy grail” of silicon photonics research. Various materials and methods have been explored, including bulk silicon light sources [38,39], erbium

(Er)-doped laser [40, 41], germanium (Ge)-on-silicon lasers [42, 43], Titanium-sapphire lasers [44, 45], and III-V-on-silicon lasers [46, 47].

1.1.3.1 Bulk Silicon Light Sources

In bulk silicon, non-radiative recombination dominates over radiative recombination, causing most electron-hole pairs to recombine non-radiatively. Despite this limitation, strategies such as surface texturing and controlling recombination mechanisms (see in Figure 1.1) have enabled room-temperature electroluminescence (EL), achieving an external quantum efficiency of 1 % at silicon's band-edge emission wavelength [38]. Another approach involves inducing stress fields in bulk silicon through boron implantation, yielding EL in silicon diodes. However, these diodes exhibit low efficiency, and their emission wavelength remains restricted to approximately 1100 nm due to the band-edge constraint, making them unsuitable for standard telecommunication wavelengths [39].

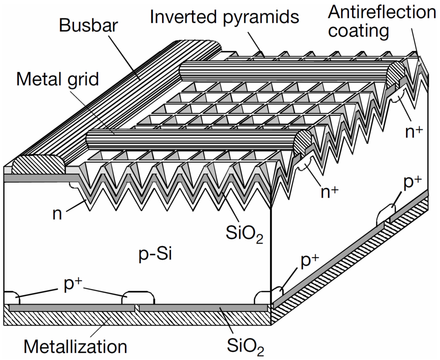

Figure 1.1: Schematic of high-efficiency silicon light-emitting diode. Reproduced from Ref. [38].

1.1.3.2 Erbium-doped laser

Erbium-doped fiber amplifiers, widely used in long-haul optical communications, have inspired on-chip light amplification and lasers. Incorporating Er^{3+} into the Si_3N_4 waveguide has realized a fully hybrid integrated single-mode lasing erbium-based laser, exhibiting $>$ 40 nm wavelength tunability in the C and L bands with a 70 dB side-mode suppression ratio (SMSR), a high output power (up to 17 mW) and a recordable intrinsic linewidth of 50 Hz [40], as shown in Figure 1.2. Another similar design from the same group gave much higher output power (more than 100 mW) [41]. However, a high pump threshold (tens of watt) and a meter-scale cavity length hinder their practical application in term of the high integration density and low power dissipation.

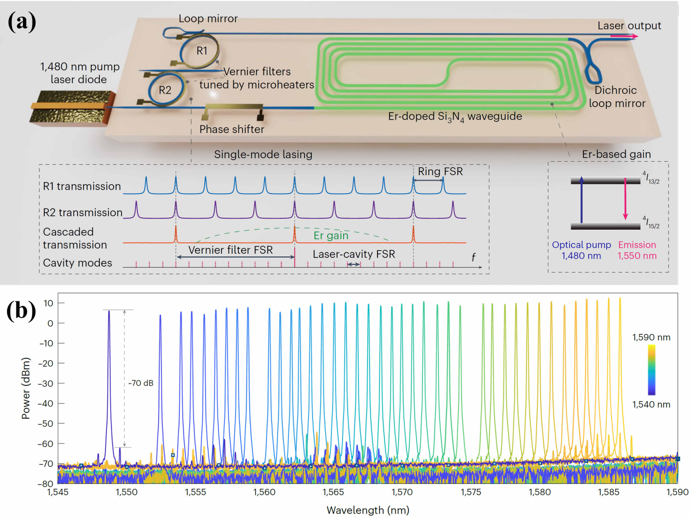

Figure 1.2: (a) Schematic of a hybrid integrated Vernier laser consisting of an Er:Si_3N_4 *photonic integrated circuit and an edgecoupled III–V-semiconductor pump laser diode. (b) Measured optical spectra of single-mode lasing tuned over the 40 nm wavelength range. All are reproduced from Ref. [40].*

1.1.3.3 Ge-on-Silicon Lasers

Epitaxial growth of Ge on silicon addresses silicon's indirect bandgap limitations. While Ge is also an indirect bandgap material, pseudo-direct bandgap behavior can be achieved through band structure engineering, including n-doping, tensile strain, and GeSn alloys. The first electrically injected Ge laser was demonstrated in 2012, but it suffered from a high threshold (280 kA/cm^2) and low efficiency [42]. In 2015, a GeSn layer grown on a virtual Ge-on-Si substrate exhibited a high density of dislocations at the interface (orange arrows in Figure 1.3 (a) [43]) but no threading dislocations (TDs) reaching the sample surface, allowing an upper limit estimate of the threading dislocation density (TDD) at 5×10^6 cm^{-2}. Leveraging this high-quality material, optically pumped GeSn lasers have been realized (Figure 1.3 (d)-(e)). However, they require low operating temperatures and high optical pump intensities ($\sim$ 325 kw/cm^2). Challenges such as free carrier absorption, wavelength redshifts, and achieving room-temperature operation remain unresolved.

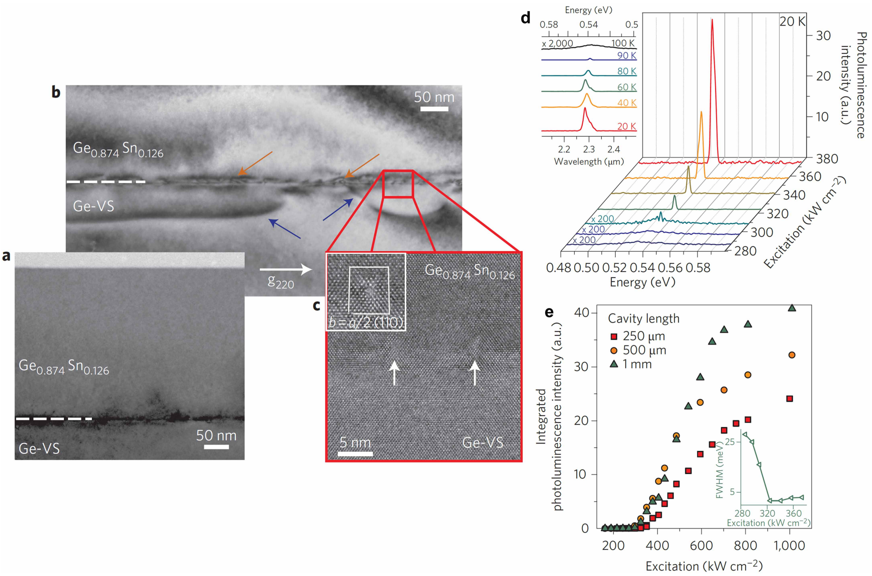

Figure 1.3: (a) Cross-sectional TEM image of $Ge_{0.874}Sn_{0.126}$. *(b) Dislocation loops (indicated by blue arrows) emitted below the* $Ge_{0.874}Sn_{0.126}$*/Ge interface (indicated by orange arrows) penetrate only into the Ge buffer. (c) High-resolution TEM image of the interface. (d) Power-dependent photoluminescence spectra of a 5-µm-wide and 1-mm-long Fabry–Perot waveguide cavity fabricated from sample* $Ge_{0.874}Sn_{0.126}$. *Inset: temperature-dependent (20–100 K) photoluminescence spectra at 1,000 kW/cm*^{2} *excitation density. (e) Integrated photoluminescence intensity as a function of optical excitation for waveguide lengths with 250 µm, 500 µm and 1 mm. Inset: FWHM around the lasing threshold for the 1-mm-long waveguide. All are reproduced from Ref. [43].*

1.1.3.4 Titanium-doped sapphire lasers

Titanium-doped sapphire (Ti:Sa) lasers are essential for optical sensing, metrology, communications, and spectroscopy but are traditionally bulky, power-intensive, and costly. Recently, the titanium:sapphire-on-insulator (Ti:SaOI) photonics platform addresses these limitations, achieving a record-low 290 µW lasing threshold and 1.0 kW peak power without pulse distortion (see Figure 1.4). Leveraging these advancements, an on-chip Ti:Sa laser was successfully employed as the sole light source in a cavity quantum electrodynamics experiment with artificial atoms in silicon carbide. This demonstrates its potential for scientific applications, offering low-cost, compact, and scalable solutions for next-generation photonic technologies [44, 45].

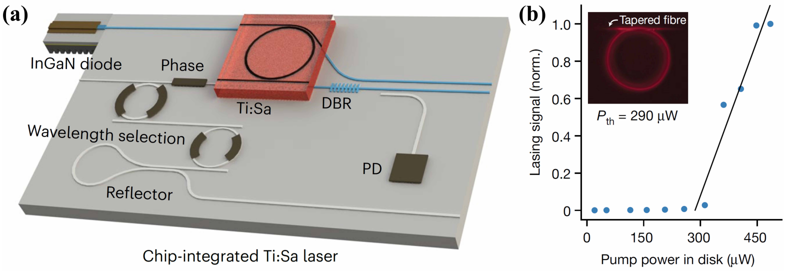

Figure 1.4: (a) Conceptional diagram of the integrated chip-based Ti:Sa laser system, consisting of an InGaN pump laser diode; a SiN waveguide loaded with Ti:Sa gain; and an external feedback circuit that includes distributed Bragg reflectors (DBRs), actively tuned microring resonators and integrated photodetectors (PDs). Ti:Sa laser cavities, external DBR cavities and diode-pumped lasing are demonstrated, and other parts are displayed in grey. (b) Lasing signal of the microdisk resonator (measured using spectrometer) with increasing pump power in the resonator, showing lasing threshold pump power of 290 μW. Inset, optical microscope image of the resonator under excitation (with 532 nm light filtered), showing spontaneous emission collected vertically. All are reproduced from Ref. [45].

1.1.3.5 III-V-on-Silicon Lasers

III-V semiconductors, with their direct bandgap and high material gain, are promising on-chip light sources. However, lattice mismatches, polarity differences, and thermal expansion disparities between III-V and silicon introduce defects like TDs, stacking faults and anti-phase boundaries, degrading optical performance. Integration techniques such as flip-chip bonding, wafer bonding, micro-transfer printing, and heteroepitaxy have been explored.

1.1.3.5.1 Hybrid integration Flip-chip bonding enables integration of III-V lasers onto silicon photonic platforms, achieving high-performance laser diodes and arrays [46,47]. However, challenges in alignment precision and the slow, costly die-to-die integration process persist.

Alternative hybrid methods like direct and adhesive bonding have shown promise, producing quantum well (QW) lasers emitting at 1.3 μm and 1.55 μm [48–50]. Despite these advances, challenges such as coupling efficiency, thermal management, and large-area high-quality contact surfaces remain. Notably, Intel has commercialized 50G silicon photonics links and expanded communication bandwidth in data centers and networks using bonding techniques [51,52].

Transfer printing offers benefits such as efficient material use and integration of diverse components. Recently, electrically pumped Fabry-Pérot (FP), distributed feedback (DFB), and vertical-cavity surface-emitting lasers (VCSELs) with high optical power, C-band emission, and high SMSR have been reported [53–55]. However, reliance on adhesives and alignment challenges remain.

1.1.3.5.2 Monolithic Growth The monolithic integration of III-V semiconductor devices on Si has attracted significant interest for Si PICs due to its cost-effectiveness and potential for large-area production, compared to other heterogeneous integration methods. However, differences in material properties between III-V compounds and Si substrates often lead to strain-induced defects during monolithic growth. These defects can compromise both device performance and reliability. Therefore, advanced techniques are needed to control defect formation in the monolithic hetero-epitaxy of III-V materials on Si. Two primary approaches for hetero-epitaxial growth on Si are growth on blanket Si wafers and growth on pre-patterned Si substrates.

III-V on blanket Si The direct approach to accommodate defects in III-V semiconductor integration on Si substrates involves inserting a thick buffer layer between the III-V active region and the silicon substrate. In the early 1980s, M. Akiyama et al. reported high mobility epitaxial GaAs by incorporating a ~ 5 µm GaAs/AlGaAs buffer layer [56]. However, this thick buffer layer poses a significant risk of thermal cracking during the cooling from growth temperature to room temperature due to the large difference in the thermal expansion coefficients between GaAs/AlGaAs and Si.

The presence of antiphase boundaries (APBs) complicates the fabrication and operation of III-V optoelectronic devices, as they propagate from the hetero-interface to the material surface. APBs are planar defects that occur in ordered crystal structures when two adjacent regions (domains) have the same composition but opposite atomic arrangements. This misalignment creates a boundary where atoms are incorrectly positioned relative to each other, leading to increased energy and potential degradation of material properties, such as electrical and mechanical performance. APBs are commonly observed in compound semiconductors, superlattices, and ordered alloys. A conventional strategy to suppress APBs involves using Si (001) substrates with offcut angles ranging from 4° to 7° toward the [110] or [111] directions and promotes the formation of stable double atomic steps on the Si surface after deoxidization and high-temperature annealing [57,58]. However, this method cannot guarantee consistent double atomic steps, and the deposition of a III-V pre-layer during continuous growth can disrupt these surface features. As a result, alternative strategies for (001) Si substrates without intentional offcut angles have been explored, including thermal annealing processes [59] and epitaxial Si buffer layers [60–62].

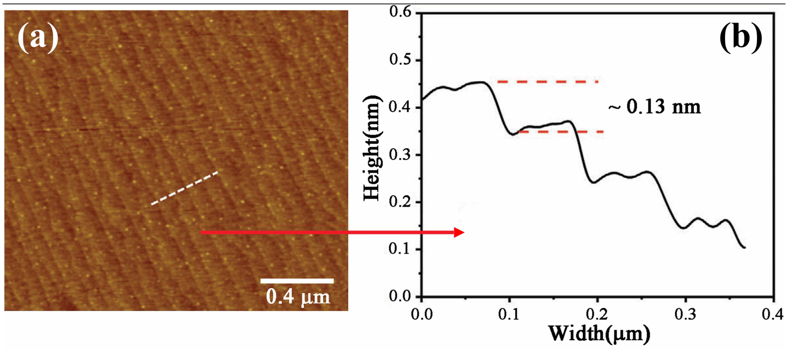

Figure 1.5: (a) 2 µm × 2 µm AFM image of Si buffer layer surface. (b) Height measurement of each step on the surface of 200 nm Si buffer. All are reproduced from Ref. [62].

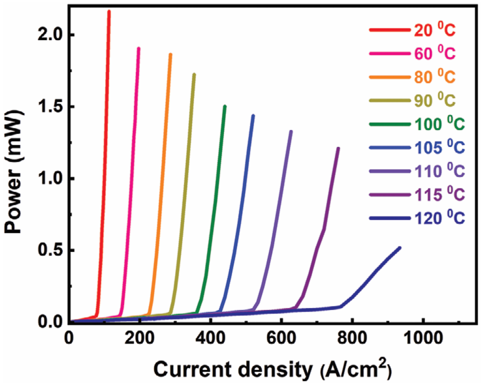

Figure 1.6: Temperature dependent L–I curve up to 120 °C of 1300 nm InAs QD laser on on-axis Si (001). Reproduced from Ref. [62].

In the 1990s, H. Mori et al. replaced the surface rearrangement of Si substrates through high-temperature annealing with a 5 µm epitaxial Si layer featuring double atomic steps, successfully demonstrating a laser diode emitting at 1.55 µm with a threshold current of 48 mA [60]. More recently, K. Li et al. investigated a 200 nm Si buffer with single atomic steps [62], as confirmed by atomic force microscopy (AFM) and step height measurements (Figure 1.5). Using a three-step growth method for GaAs and InAs QDs within GaAs following Si buffer deposition, they achieved an electrically pumped 1.3 µm InAs QD laser. This laser exhibited a low threshold current density of 83.3 A/cm^2 at 20 °C, and a maximum operating temperature of 120 °C, as shown in Figure 1.6. Room-temperature EL spectra (Figure 1.7) showed spontaneous emission at an injection current density of 80 A/cm^2 and lasing at 1303.9 nm under 90 A/cm^2.

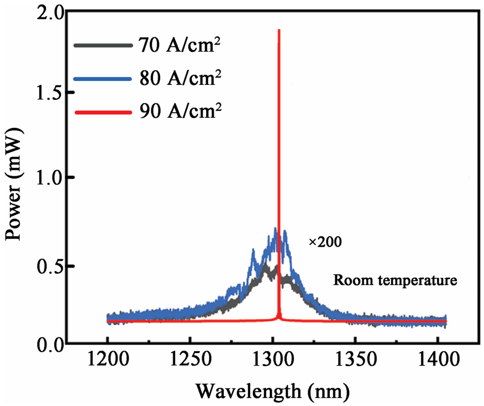

Figure 1.7: EL spectra of InAs QD laser on on-axis Si (001) substrate at different injection current densities. Reproduced from Ref. [62].

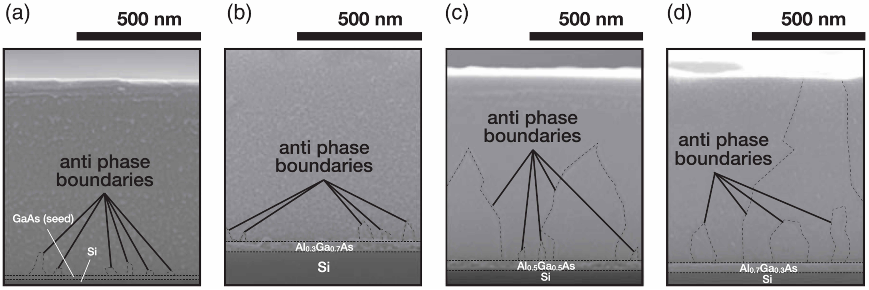

Figure 1.8: Cross-sectional SEM images of GaAs layer with (a) GaAs nucleation layer, (b) $Al_{0.3}Ga_{0.7}As$ nucleation layer, (c) $Al_{0.5}Ga_{0.5}As$ nucleation layer, and (d) $Al_{0.7}Ga_{0.3}As$ nucleation layer grown on (001) Si substrates. All are reproduced from Ref. [63].

An alternative strategy for suppressing APBs on Si (001) substrates with no off-axis angle is optimizing the initial III-V nucleation layer to promote self-annihilation of APBs [63]. J. Kwoen et al. explored the effect of AlGaAs nucleation layers on APB elimination, demonstrating an APB-free GaAs layer grown directly on on-axis (001) Si. Figure 1.8(a)-(d) presents cross-sectional scanning electron microscope (SEM) images of GaAs/Si with various $\mathrm{Al}_x\mathrm{Ga}_{1-x}\mathrm{As}$ (x = 0, 0.3, 0.5, 0.7) nucleation layers. Figure 1.8(d) shows that APBs extend through the GaAs buffer layer on an $\mathrm{Al}_{0.7}\mathrm{Ga}_{0.3}\mathrm{As}$ seed layer, while the $\mathrm{Al}_{0.3}\mathrm{Ga}_{0.7}\mathrm{As}$ seed layer effectively induces APB self-annihilation near the nucleation layer (Figure 1.8(b)). In Figure 1.9, the photoluminescence (PL) intensity of the InAs QD layer grown on GaAs/Si with an $\mathrm{Al}_{0.3}\mathrm{Ga}_{0.7}\mathrm{As}$ nucleation layer is twice that with a GaAs nucleation layer. The PL intensity increases as the Al content decreases. These findings indicate that an APB-free GaAs layer can be achieved with an $\mathrm{Al}_{0.3}\mathrm{Ga}_{0.7}\mathrm{As}$

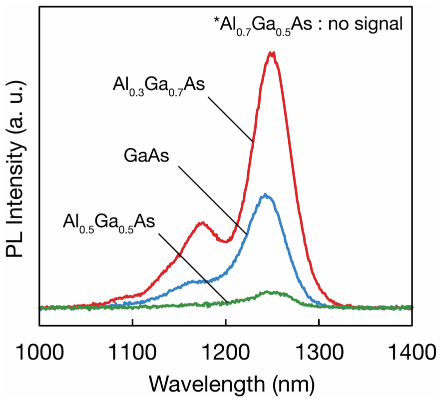

Figure 1.9: Room temperature PL intensity of an InAs QD layer grown on Si with different nucleation layers. Reproduced from Ref. [62].

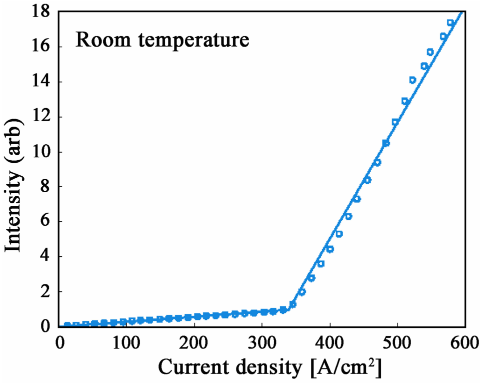

Figure 1.10: L-I curve of an InAs/GaAs QD laser grown on GaAs/Si (001) substrate under pulsed operation conditions at room temperature (25 °C). Reproduced from Ref. [64].

nucleation layer, with APB suppression attributed to self-annihilation. However, the detailed annihilation mechanism remains unclear, and critical parameters are yet to be determined. This group also fabricated a 2 mm-long electrically driven FP laser using the $Al_{0.3}Ga_{0.7}As$ nucleation layer [64]. The laser exhibited a threshold current density of 320 A/cm² at room temperature and a maximum operating temperature of 70 °C (Figures 1.10 and 1.11). Room-temperature EL spectra (Figure 1.12) show spontaneous emission below the threshold and lasing above it.

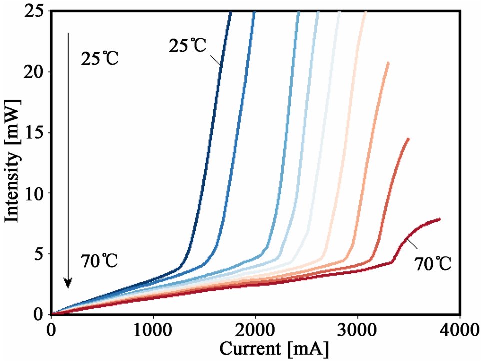

Figure 1.11: L-I curves of an InAs/GaAs QD laser grown on GaAs/Si (001) substrate under pulsed operation conditions at various temperatures. Reproduced from Ref. [64].

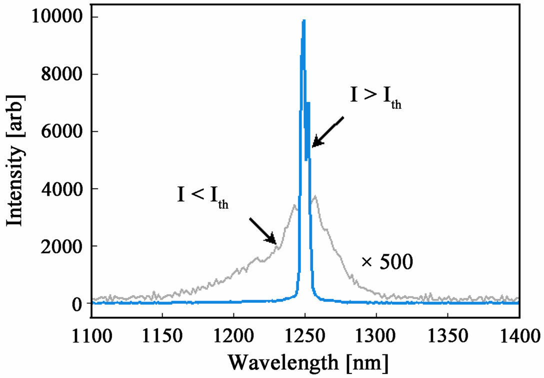

Figure 1.12: Emission spectra of the InAs/GaAs QD laser on GaAs/Si (001) substrate at room temperature (25 °C). Reproduced from Ref. [64].

TDs are line defects in a crystal where an atomic plane is disrupted, extending from the interface to the surface. They commonly occur in heteroepitaxy due to lattice mismatch. The difference between APBs and TDs are given in the table 1.1.

Feature	Threading dislocations (TDs)	anti-phase boundaries (APBs)
Type	Line defect	Planar defect
Cause	Lattice mismatch, strain	Ordered domains misalignment
Effect	Degrades electrical, mechanical properties	electrical properties degradation
Common in	Heteroepitaxy, strained layers	Ordered alloys, superlattices

Table 1.1: The difference between TDs and APBs.

Achieving a low TDD is crucial for high-quality III-V layers monolithically grown on Si. TDs that penetrate the active region of optoelectronic devices can significantly degrade performance. For example, QW lasers monolithically grown on Si substrates, with a TDD of approximately 5×10^7 cm^{-2} (common for GaAs/Si), exhibit no lasing behavior [65]. As a result, extensive efforts have focused on methods such as two-step growth [66–68], thermal cycle annealing [69, 70], graded buffer layers [71–74], and defect filter layers [75–85] to reduce TDD. These approaches have led to a TDD of about 10^6 cm^{-2} for GaAs-on-Si [80], as discussed below.

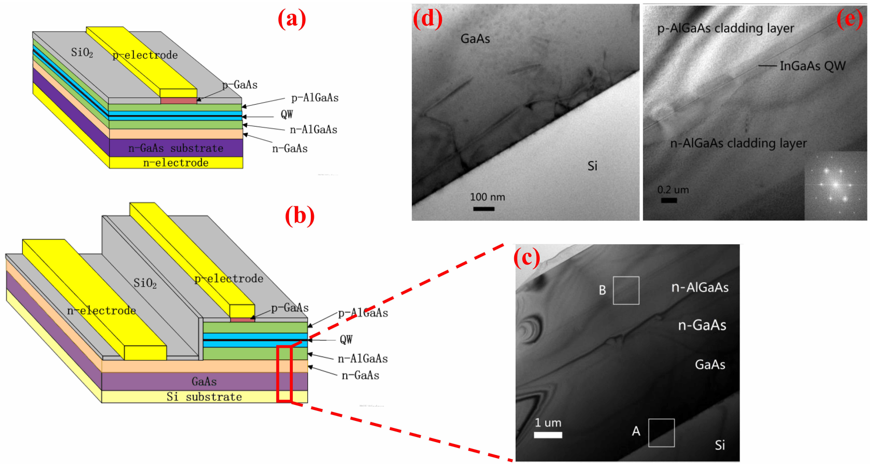

Figure 1.13: Schematics of the laser structures on GaAs (a) and Si (b) substrates. (c) Cross-sectional TEM images of the sample of the laser structure on Si. (d) and (e) are the amplified images of region A and B in (c). All are reproduced from Ref. [70].

Two-step growth begins with low-temperature epitaxial growth (around 400 °C for GaAs) to control defect generation near the III-V/Si interface, followed by high-temperature epitaxial growth for optimal crystal quality. In recent years, a three-step growth method, which adds an intermediate-temperature layer between the low- and high-temperature stages, has been commonly employed. In 2015, J. Wang et al. applied this three-step method to grow low-threshold-current-density InGaAs/AlGaAs QW lasers on Si [70], comparing them with devices grown on native GaAs substrates. The device schematics are shown and most of defects are confined at GaAs/Si interface (see Figure 1.13). They also introduced thermal cycle annealing during growth to further reduce dislocations, as it promotes thermally activated dislocation migration and annihilation. The laser on the Si substrate achieved lasing with a cavity length of 1 mm and a threshold current density of 313 A/cm^2 (Figure 1.14), while the GaAs-based device exhibited a threshold current density of 135 A/cm^2. The Si-based QW laser could be operated under continuous pumping at 240 K (Figure 1.15).

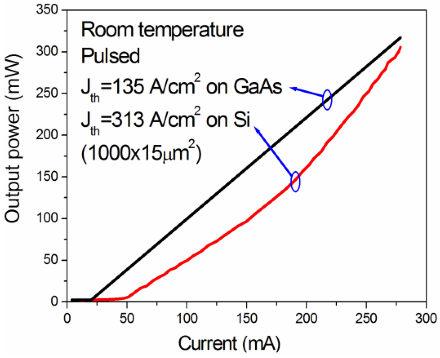

Figure 1.14: L-I characteristics of the lasers grown on Si and GaAs substrates, respectively. Reproduced from Ref. [70].

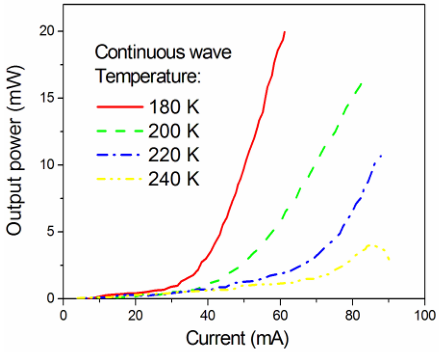

Figure 1.15: L-I characteristics of the laser on Si under continuous wave conditions at different temperatures. Reproduced from Ref. [70].

To address the material dissimilarity between Si and III-V, a common solution is to use materials that match the lattice constant and thermal expansion coefficient of Si. For GaAs/Si heteroepitaxy, a compositionally graded buffer has been extensively studied [71–74]. For instance, M. E. Groenert et al. demonstrated room-temperature continuous-wave (CW) GaAs/Al$_x$Ga$_{1-x}$As QW lasers monolithically grown on 10 µm relaxed graded Ge/Ge$_x$Si$_{1-x}$ virtual substrates (Figure 1.16 (a)-(b)) on Si [71]. This device exhibited lasing at 858 nm with a threshold current of 86 mA, corresponding to a calculated threshold current density of 577 A/cm^2 (Figure 1.16 (c)). The laser on the Si substrate showed similar turn-on behavior to that on the native GaAs substrate. However, the use of graded Ge$_x$Si$_{1-x}$ buffers generally requires a thicker layer. For monolithic integration on Si platforms, a thinner buffer layer is preferred to minimize thermal cracking and enable co-integration with other components.

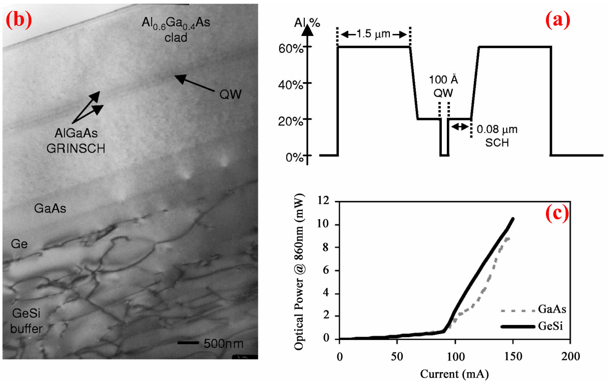

Figure 1.16: (a) Band gap schematic of AlGaAs/GaAs quantum well structure used for successful laser demonstration on Ge/Ge$_x$Si$_{1-x}$/Si substrates, and (b) TEM cross-section micrograph of this laser structure on Ge/Ge$_x$Si$_{1-x}$/Si. Processed lasers had cavity lengths of 1.0–0.7 mm and oxide stripe widths of 5–20 mm. (c) Light vs current for identical AlGaAs/GaAs quantum well lasers grown on Ge/Ge$_x$Si$_{1-x}$/Si and GaAs substrates. All are reproduced from Ref. [71].

Defect filter layers have been widely studied since the 1980s to reduce dislocation density [75–78]. QD [79] and strained super-lattice layers [80,81] have emerged as effective candidates for defect filtering. Leveraging this advanced technology, carrier lifetime for QDs from Huiyun's and Bowers' group extend to nano-second scale [82, 83] and high performance electrically-driven devices [80, 84, 85] were demonstrated. For example, B. Shi et al. [79] used multiple InAs/InP QDs as dislocation filters, reducing the defect density on the InP surface to 3×10^8 cm^{-2} and improving the optical properties of active photonic devices. S. Chen et al. [80] optimized InGaAs/GaAs super-lattice defect filter layers, achieving a TDD of around 10^5 cm^{-2} in the III-V epilayers (see Figure 1.17). Using this approach, they demonstrated a 3.2-mm electrically-driven CW InAs/GaAs QD laser with a low current density of 62.5 A/cm^2, room-temperature output power exceeding 105 mW (Figure 1.18(a)), and an operation temperature of up to 120 °C (pulse, Figure 1.18(b)).

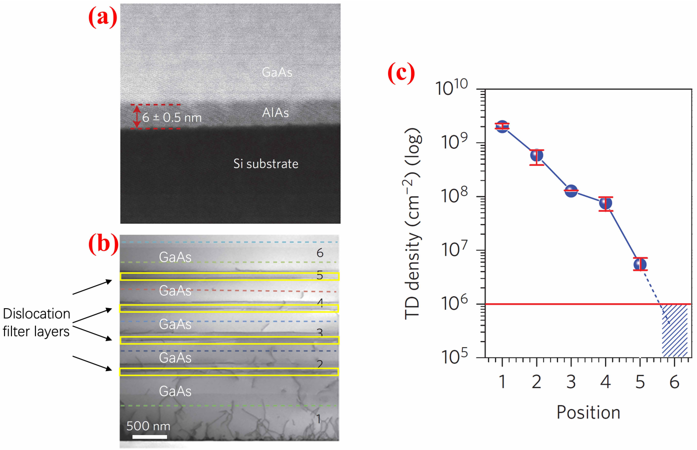

Figure 1.17: (a) High-angle annular dark-field scanning TEM image of the interface between the 6 nm AlAs nucleation layer and a silicon substrate. (b) Bright-field scanning TEM image of dislocation filter layers. (c) Dislocation density measured at different positions, as indicated in (b). All are reproduced from Ref. [80].

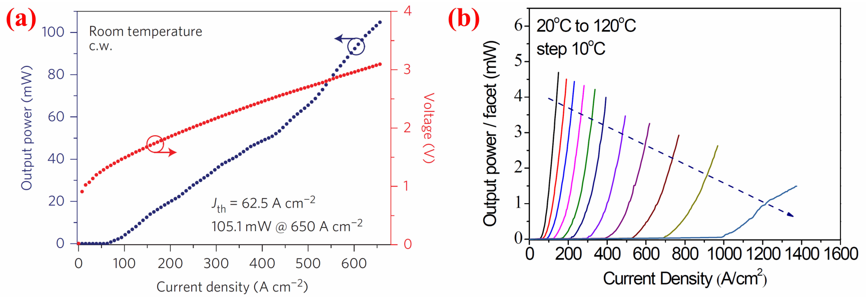

Figure 1.18: (a) LIV characteristics for a 50 µm × 3200 µm InAs/GaAs QD laser grown on a Si substrate under continuous-wave operation at 18 °C. (b) Light output power versus current density for a 50 µm × 3200 µm InAs/GaAs QD laser on Si at various heat sink temperatures under pulsed operation. All are reproduced from Ref. [80].

Growth in small regions The growth of III-V materials in small regions has been extensively studied in recent decades. This approach enables epitaxial III-V layers to be grown on pre-patterned silicon substrates, typically defined by SiO_x or SiN_x dielectric masks. Advanced techniques such as epitaxial lateral overgrowth (ELO), template-assisted selective epitaxy (TASE), and selective area growth (SAG) combined with aspect ratio trapping (ART) have been explored and are discussed below.

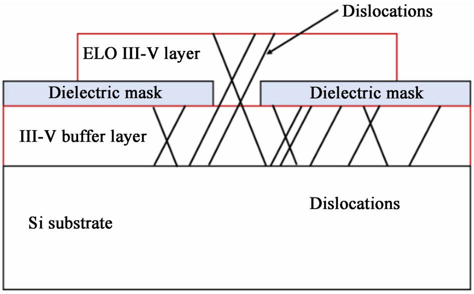

Figure 1.19: A schematic illustration of the epitaxial lateral overgrowth. Reproduced from Ref. [86].

To enable large-area growth of III-V materials on Si, ELO was developed. In this process, a III-V buffer layer is first grown on the Si substrate, followed by deposition of a dielectric mask (such as SiO_2 or Si_3N_4). The mask is then selectively etched to expose the III-V buffer layer for regrowth. The III-V epitaxial layer grows both vertically through the exposed mask regions and laterally over the mask. Most TDs in the buffer layer are blocked by the mask's bottom, with only a few propagating upwards around the openings (Figure 1.19). As a result, the laterally grown layer above the mask exhibits high crystalline quality. This technique has enabled the development of GaAs/AlGaAs lasers [87] and 100 µm-cavity GaN-based edge-emitting laser diodes [88] on Si, achieving thresholds of 0.81 kA/cm^2 at 854 nm and 83 kA/cm^2 at 416 nm, respectively. However, ELO-grown III-V materials suffer from limited defect-free regions and mechanical weakness in the laterally grown layers, which become more pronounced with increased layer thickness. Additionally, defects may arise during the lateral epitaxial island coalescence.

Despite these limitations, Plessey, a leader in the microLED industry, has commercialized single-chip high-power LEDs based on GaN-on-Silicon [89]. Recently, the company also proposed a record-breaking 2.5-micron pixel pitch ultra-high-resolution microLED display for next-generation Augmented Reality (AR) and Virtual Reality (VR) applications [90].

TASE, developed by the IBM research group in Zurich, is a promising method

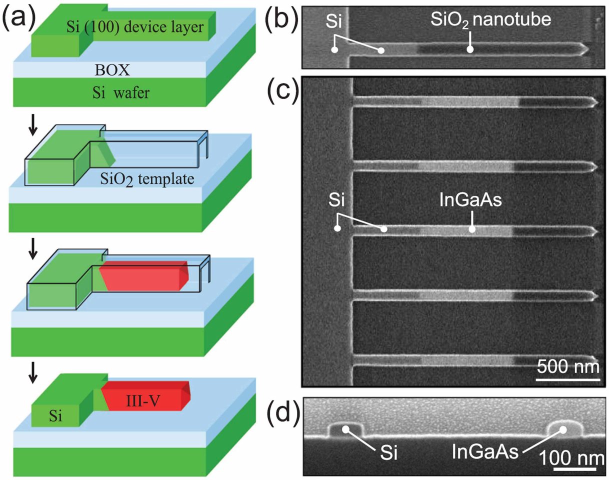

Figure 1.20: Schematic illustrating TASE process and experimental results. (a) From top to bottom: shape definition, nanostructure formation by oxide deposition and Si back-etching, selective epitaxy, and template oxide removal. (b) SEM images of a template structure containing a Si pad and a Si nanowires covered by a SiO_2 film. Part of the Si nanowires was back-etched to create a hollow tube, which was partially filled with InGaAs (c). (d) SEM cross-section image after removal of the template oxide, showing a co-planar integrated Si and InGaAs nanostructure. All are reproduced from Ref. [91].

for in-plane growth of III-V materials on Si wafers [91–94]. The process overview is illustrated in Figure 1.20 (a) [91]. A patterned Si device layer on an SOI substrate is covered with a SiO_2 layer using atomic layer deposition. Openings in the SiO_2 are created using buffered hydrofluoric acid (BHF) etching, followed by tetramethylammonium hydroxide (TMAH) etching to expose the underlying $\{111\}$ Si planes. The prepared substrate is then dipped in diluted (2.5 %) HF to remove the native oxide and immediately transferred to the MOCVD (Metal-Organic Chemical Vapor Deposition) reactor for III-V material growth. Figures 1.20 (b), (c) and (d) show SEM images of InGaAs nanowires grown on Si using TASE, giving a perfectly co-planar geometry and electrically isolated Si and InGaAs nanowires.

This technique also facilitates electrical contact fabrication for III-V lasers and light coupling from the cavity to silicon waveguides. Recent device demonstrations from this group include GaAs microdisk lasers [92], InGaAs microdisk lasers [93], and InGaAs/InP QW lasers [94], all integrated on III-V virtual substrates via TASE. The GaAs microdisk laser [92] exhibited lasing at 837 nm and 857 nm, with a threshold of 3 pJ/pulse at 300 K (Figure 1.21). This laser has a small footprint of 9π μm^2, showing promise for high-density integration. However, TASE depends heavily on the pre-definition of SiO_2 templates with Si seeds for III-V nucleation, posing mechanical stability challenges for large-area epitaxial growth.

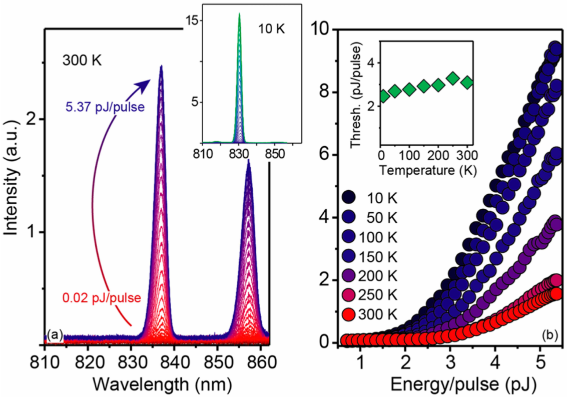

Figure 1.21: Optical characteristics of GaAs microdisk lasers at (a) room temperature and 10 K (inset). (b) Temperature dependent light-in light-out curves. The temperature-dependent lasing threshold is shown in the inset. All are reproduced from Ref. [92].

ART offers another solution for achieving high-quality III-V layers on Si by trapping defects within the patterned dielectric mask, typically SiO_2. This method requires optimized growth parameters, mask pattern designs, and specific Si surface cleaning techniques due to the confined structures and reduced dimensions [95]. When the dielectric mask pattern has an adequate aspect ratio (mask height/mask width), it effectively reduces defect density. As shown in Figure 1.22 [96], TDs tend to glide along the $\{111\}$ slip plane, reaching the oxide sidewall and becoming trapped, regardless of whether the $\{111\}$ plane is parallel or perpendicular to the trench orientation. The minimum aspect ratio for effective trapping is at least 1.43. APBs can also be trapped using trench structures, but only when the $\{111\}$ planes are parallel to the trench. Trapping APBs on planes perpendicular to the trench orientation is not possible. Using V-shaped Si surfaces and advanced surface cleaning techniques can control the APBs and stacking faults formation during III-V material nucleation on etched $\{111\}$ Si planes [97].

Using advanced ART techniques, Han et al. [98] successfully demonstrated the growth of InP/$In_{0.53}Ga_{0.47}As$ nanoridges within nanoscale Si trenches, as illustrated in the tilted-view SEM and TEM images (Figure 1.23(a), (b), and (d)). Figure 1.23(b) reveals that the significant lattice mismatch between InP and Si is mitigated by the formation of a thin layer of high-density planar defects at the III-V/Si interface, thereby improving the crystalline quality of the upper InP layer. At room temperature, the nanoridge array emits at approximately 1500 nm (Figure 1.23(c)), attributed to the five $In_{0.53}Ga_{0.47}As$ QW layers (Figure 1.23(d)).

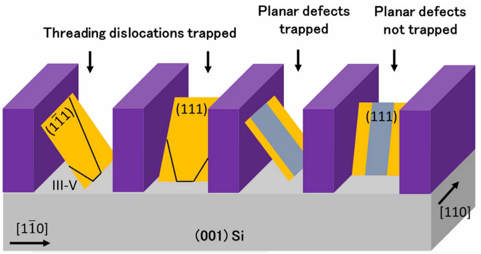

Figure 1.22: The trapping mechanism of the ART technique for TDs and planar defects. Reproduced from Ref. [96].

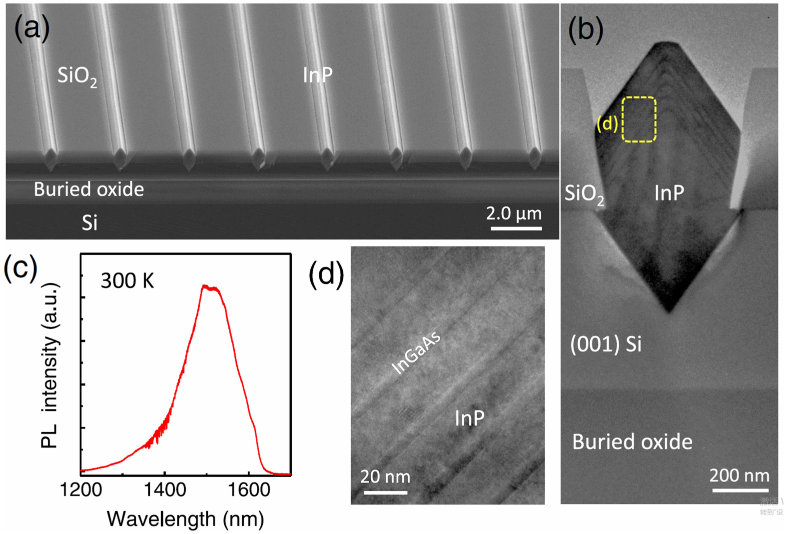

Figure 1.23: (a) SEM image of the InP/In$_{0.53}$Ga$_{0.47}$As nanoridge array on (001) SOI. (b) TEM image of one nanoridge, showing inserted In$_{0.53}$Ga$_{0.47}$As ridge QWs and buried oxide layer. (c) Room-temperature photoluminescence spectra of the as-grown nanoridges. (d) Close-up of one side of the InGaAs ridge QWs. All are reproduced from Ref. [98].

These high-quality nanoridges enabled a 40 µm-long FP cavity, achieving single-mode lasing with a remarkably low threshold of $\sim$ 40 µJ/cm^2 at room temperature (Figures 1.24 and 1.25).

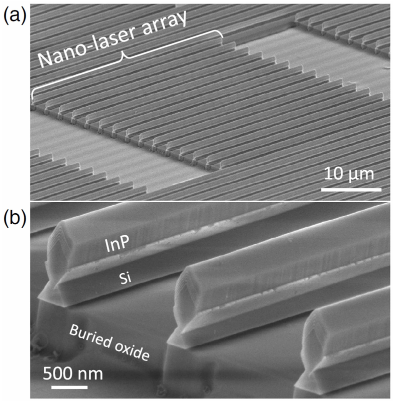

Figure 1.24: (a) Tilted-view SEM image of the InP/In$_{0.53}$Ga$_{0.47}$As nanolaser array on (001) SOI. (b) Zoomed-in SEM image of the end facets of the nanolaser array. All are reproduced from Ref. [98].

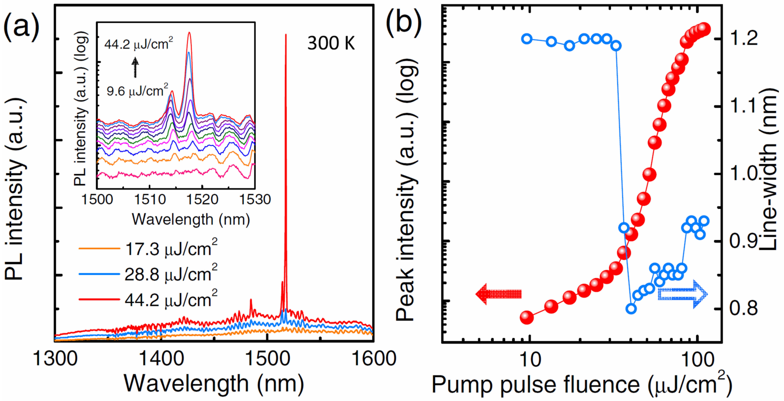

Figure 1.25: (a) Room-temperature emission spectra from InP/In$_{0.53}$Ga$_{0.47}$As nanolaser around threshold. Inset shows the emission spectra plotted in a logarithmic scale. (b) The evolution of the peak intensity and the linewidth as the excitation level increases. All are reproduced from Ref. [98].

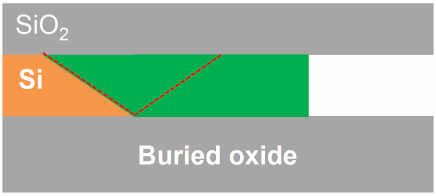

Figure 1.26: The scheme of LART. The red dotted lines denote the confinement of the majority of crystalline defects at the III-V/Si interface and the trapping of residual TDs by the top and bottom SiO$_2$ layers. Reproduced from Ref. [99].

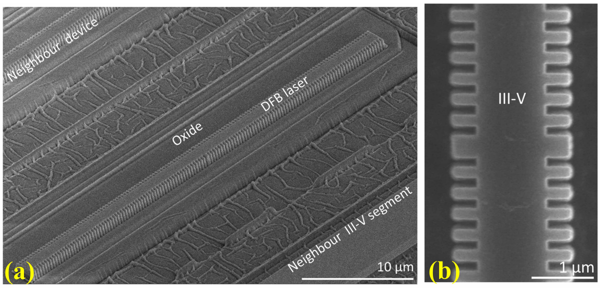

Figure 1.27: (a) Tilted view SEM image of the InGaAs/InP DFB lasers and adjacent III-V segment on SOI. (b) Top view SEM image presenting the uniformity of the lateral grating. All are reproduced from Ref. [100].

To meet the demands of Si PICs, III-V light emitters not only require large epitaxial material volumes but also enable direct light coupling to silicon waveguides. While conventional ART combined with overgrown III-V material shows potential for large-area in-plane growth, achieving effective light coupling remains a challenge. To address this, the lateral aspect ratio trapping (LART) technique was developed [99–101]. LART, as illustrated in Figure 1.26, enables the direct growth of in-plane, micrometer-scale III-V crystals above a buried oxide layer. Unlike ART, LART changes the groove direction to facilitate lateral growth, with $\{111\}$-oriented silicon pedestals inhibiting APB formation and wide SiO_2 trenches blocking TDs, thereby enhancing lateral aspect ratio characteristics. This approach allows for better control over III-V material volume by varying the Si layer dimensions on SOI substrates. The in-plane and close placement of the III-V layer with the Si device layer supports integration with Si photonic components. Using LART, Xue et al. [99] demonstrated a compact in-plane 1.5 µm DFB laser with InP gratings on both sides, as SEM images shown in Figures 1.27. The fabricated laser exhibited a threshold of 17.5 $\mu J/cm^2$ and a cavity length of $\sim$ 40 µm (Figures 1.28). This co-planar laser configuration with the silicon device layer presents a new approach for achieving large III-V material volumes and direct coupling. However, exposing the III-V active material to air increases the risk of non-radiative recombination, which can degrade optical performance and device lifetime.

To overcome the limitations of total III-V material volume in ART, the III-V epitaxy group at imec developed an innovative approach known as nano-ridge engineering (NRE). The idea is to increase the III-V volume with the growth out of the narrow trench. By optimizing metal-organic vapor phase epitaxy (MOVPE) growth conditions, distinct nano-ridge shapes, such as elongated rectangles, different diamond profiles or triangles, can be engineered [102], as shown in Figure 1.29. The straight and uniform ridges in Figure 1.29(a) with flat surfaces in all directions are promising for realizing waveguides with low light scattering losses. Compressively

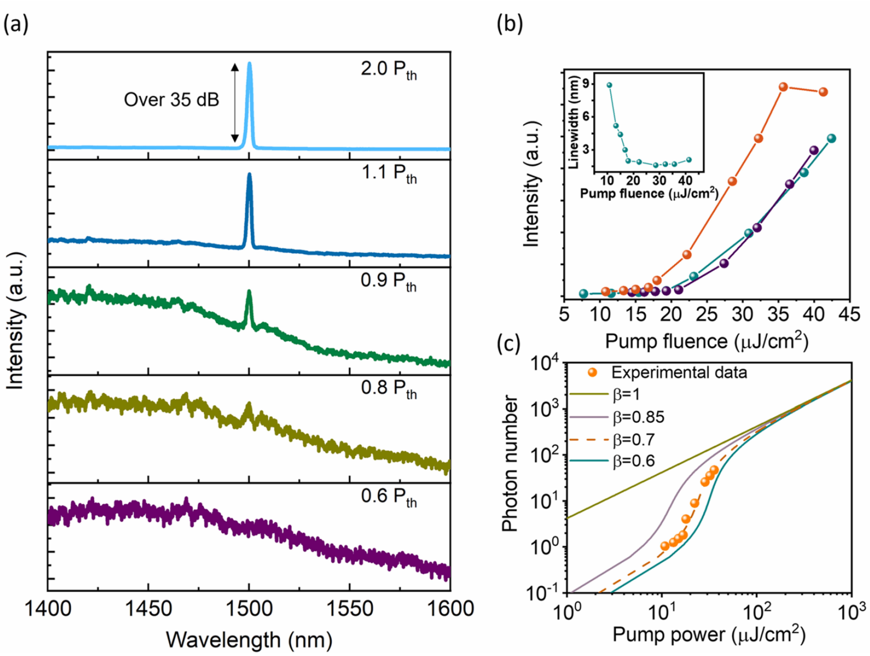

Figure 1.28: (a) Room temperature spectra of the InGaAs/InP DFB laser on SOI at various pump powers. (b) Measured light-in–light-out curves of the DFB lasers on SOI. Inset: linewidth evolution proving the lasing behavior. (c) Rate equation model solutions for various β values with β of 0.7 delivers the best fit to the experimental data. All are reproduced from Ref. [100].

strained InGaAs/GaAs multiple QWs incorporated within the box-shaped sections outside the trench, have been shown to exhibit significant QW photoluminescence at room temperature [103–105]. Key factors for achieving high-quality nano-ridges include: 1) controlling the plastic relaxation region as close to the III-V/Si interface as possible during the nucleation process [106, 107], 2) maintaining high enough aspect ratio to separate defects in the trench from the gain region in the box-part outside the trench, 3) leveraging the crystal plane dependent growth rate to obtain well-defined nano-ridges' profiles [108].

Exploiting these high-quality III-V nano-ridges, Shi et al. [103] demonstrated an optically pumped InGaAs/GaAs DFB laser directly grown on Si.The tilted SEM image (see Figure 1.30(a)) illustrates the overview of the fabricated DFB lasers, leaving enough space between two individual devices for the single laser characterization. The cross-sectional SEM images in Figure 1.30(b) and (c) give the zoomed-in $\lambda/4$ phase shift section, and the second-order grating coupler section. This device showed lasing at a wavelength of $\sim$ 1020 nm with a pump density

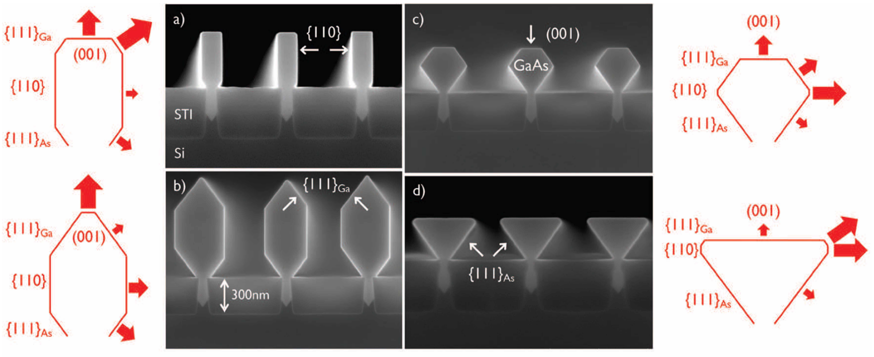

Figure 1.29: (a)-(d) Cross-section SEM images of GaAs nano-ridges deposited under very different MOVPE growth conditions. The simplified sketch next to each SEM image compares the growth rates on the different facets indicated by the size of the red arrow. All are reproduced from Ref. [102].

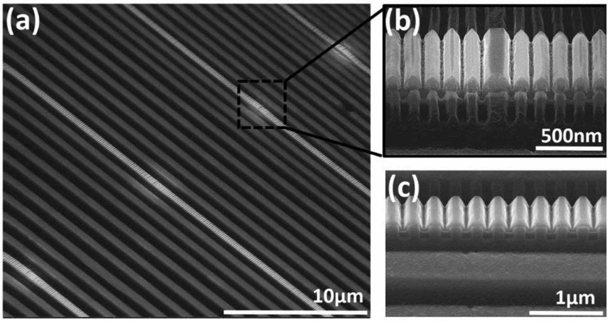

Figure 1.30: SEM of (a) the InGaAs/GaAs DFB laser array, (b) the zoomed-in $\lambda\backslash 4$ phase shift section and (c) the second-order grating coupler section. All are reproduced from Ref. [103].

threshold of 33.6 kW/cm^2 and a cavity length of $\sim$ 100 μm (Figure 1.31). The lasing wavelength can be tuned by adjusting the nano-ridge dimensions and grating period, which is useful for wavelength division multiplexing in integrated Si photonic circuits (Figure 1.32). Colucci et al. [105] later explored the growth of $In_{0.25}Ga_{0.75}As$ matrix containing three $In_{0.45}Ga_{0.55}As$ QWs. Using the higher Indium content in the active regions, they demonstrated a $\sim$ 1300 nm DFB laser with a metal grating atop the nano-ridges for telecommunications applications.

The mode profiles of these lasers are confined to the box-shaped region outside the trench, minimizing carrier loss. However, this configuration results in lower light coupling efficiency to Si waveguides compared to LART-grown III-V materials. Shi et al. [109] explored various couplers — directional, linear taper, and adiabatic

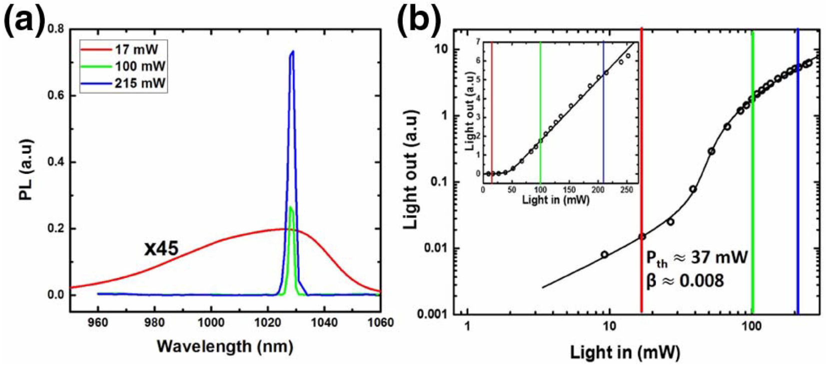

Figure 1.31: (a) Room-temperature spectra of the InGaAs/GaAs DFB laser under different pump powers (100 nm trench width, 170 nm grating period and 340 nm second-order grating coupler period). (b) Light-in-Light-out curve on logarithmic and linear (inset) scale of the measured DFB nano-ridge laser. Black circles and solid line represent the experimental data and the rate equations fit, respectively. All are reproduced from Ref. [103].

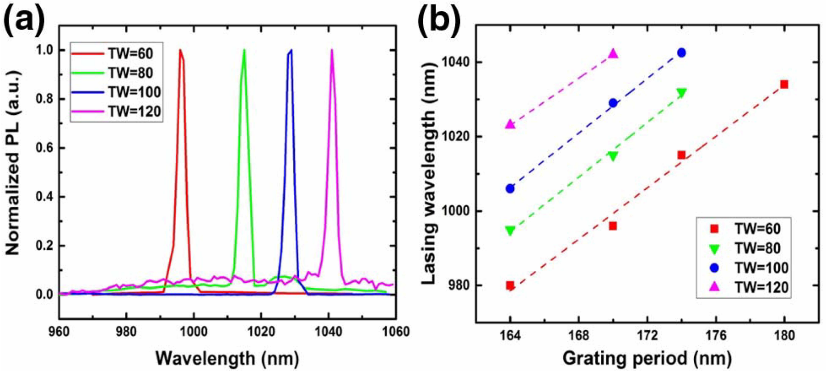

Figure 1.32: (a) Measured lasing spectra of the InGaAs/GaAs DFB laser array with grating period 170 nm. (b) Lasing wavelength versus grating period for trench size varying from 60, 80,100, 120 nm. All are reproduced from Ref. [103].

— to enhance coupling efficiency. This paves the way for integrating III-V lasers monolithically grown on SOI wafers with other photonic components and move closer to a fully functional silicon photonics platform.

1.2 Research objectives

The aim of this Ph.D. research was to investigate the feasibility of using $In_{0.25}Ga_{0.75}As/GaAs$ and $In_{0.45}Ga_{0.55}As/In_{0.25}Ga_{0.75}As$ nano-ridges as low-threshold, compact on-chip light sources. This objective can be divided into three key aspects:

- Characterizing the optical properties of nano-ridges
- Demonstrating nano-ridge lasers with low thresholds and small footprints
- Extending the lasing wavelength to the O-band

The initial goal was to lower the threshold in DFB lasers and photonic crystal (PC) laser through manipulating the electric field distribution, following the optical characterization of nano-ridge materials. To meet the requirement of high-intensity integration, strong gratings or photonic crystals with high refractive index contrast were employed to enhance light-matter interaction within a compact footprint. This work aims to achieve ultra-compact lasers as small as 10 µm, a significant reduction from previously demonstrated cavities exceeding 100 µm. Given the demands of telecommunication applications, extending the lasing wavelength to the O-band is a significant challenge.

This research was conducted within the Photonics Research Group (PRG) at Ghent University as part of the optical interconnect program at imec, which supplied the nano-ridge materials.

1.3 Outline of this thesis

The introduction chapter provides an overview of the background on Si PICs, III-V material hybrid integration methods and the state-of-the-art in III-V monolithic growth strategies. We discuss the requirements, opportunities, and challenges for III-V integration on silicon. Based on this, we introduced the objectives of this research work: the development of monolithically grown nano-ridge lasers with low thresholds and small footprints.

Chapter 2 describes the nano-ridge DFB lasers with an amorphous silicon (aSi) grating on top. We begin with device simulations using a well-defined model, followed by fabrication details. $\lambda/4$-shifted DFB lasers are then presented, demonstrating single-mode lasing with a low threshold. A rate equation analysis provides deeper insights into threshold behavior.

Chapter 3 focuses on nano-ridge DFB lasers designed with minimized cavity dimensions. We compare the optical properties of DFB lasers with aSi gratings placed on the top and on both sides of the nano-ridge.

Chapter 4 explores PC nano-ridge lasers targeting low thresholds, compact cavity footprints, and wavelength extension into the optical fiber communication band. Advanced design principles, etching processes, and passivation techniques are discussed, alongside an analysis of the optical performance of these devices.

Finally, Chapter 5 summarizes the overall research findings and suggests directions for future work in the field of monolithic III-V integration on silicon.

1.4 Publications

1.4.1 Publications in international journals

1. Z. Ouyang, D. Colucci, E. M. B. Fahmy, A. A. Yimam, J. Van Campenhout, B. Kunert and D. Van Thourhout,InGaAs/GaAs nano-ridge laser with an amorphous silicon grating monolithically grown on 300 mm Si wafer[J], Optics Letters, 40(18), 4741-4744, 2024.

2. Z. Ouyang, E. M. B. Fahmy, D. Colucci, A. A. Yimam, J. Van Campenhout, B. Kunert and D. Van Thourhout, Ultra-compact optical pump InGaAs/GaAs nano-ridge distributed feedback laser monolithically grown on 300 mm silicon substrate[J], Optics Letters, 50(7), 2358-2361, 2025.

1.4.2 Publications in international conferences

1. Z. Ouyang, D. Colucci, E. M. B. Fahmy, A. A. Yimam, J. Van Campenhout, B. Kunert and D. Van Thourhout, Compact 1.31 µm-emission $In_{0.45}Ga_{0.55}As/In_{0.25}Ga_{0.75}As$ photonic crystal nano-ridge laser monolithically grown on 300 mm silicon substrate. 2024, presentation. Society of Photographic Instrumentation Engineers Europe 2024 (SPIE Europe 2024), Strasbourg, France. Conference date: 07-04-2024 through 11-04-2024.

2. Z. Ouyang, E. M. B. Fahmy, D. Colucci, A. A. Yimam, B. Kunert and D. Van Thourhout, Side-amorphous-silicon-grating InGaAs/GaAs nano-ridge distributed feedback laser monolithically grown on 300 mm silicon substrate (Best paper). 2023, presentation. Asia Communications and Photonics Conference 2023 (ACP/IPOC 2023), Wuhan, Hubei, China. Conference date: 04-11-2023 through 07-11-2023.

3. Z. Ouyang, E. M. B. Fahmy, D. Colucci, A. A. Yimam, B. Kunert and D. Van Thourhout, Low-optical-pump-threshold InGaAs/GaAs nano-ridge laser monolithically grown on 300 mm silicon substrate. 2023, presentation. Conference on Lasers and Electro-Optics 2023 (CLEO 2022), San Jose, California, USA. Conference date: 07-05-2023 through 09-05-2023.

4. Z. Ouyang, E. M. B. Fahmy, D. Colucci, A. A. Yimam, B. Kunert and D. Van Thourhout, Top-amorphous-silicon-grating InGaAs/GaAs nano-ridge distributed feedback laser monolithically grown on 300 mm silicon substrate. 2022, presentation. IEEE Photonics Benelux 2022, Eindhoven. Conference date: 24-11-2022 through 25-11-2022.

2

DFB laser with aSi grating on top

In Chapter 1, we explored the potential of III-V material integration for on-chip lasers, emphasizing the challenges of heteroepitaxy and strategies to address them. Despite progress, many devices still exhibit high threshold values in the range of pJ/pulse (100 fs) [99] or kA/cm^2 [87, 88, 110], falling short of low-energy consumption requirements.

In our group, the previous work on DFB lasers with etched gratings in nano-ridges has shown promising results. However, the threshold of these devices was still relatively high. One of the suspected reasons is that the etched structure caused damage to the InGaP passivation layer, which introduces carrier loss paths at the GaAs-air interface and within the GaAs bulk. Hence, it is necessary to avoid such defect formation for improving the laser performance. Therefore, in this work, a high-refractive-index aSi grating was deposited on top of the nano-ridge rather than etching a grating inside the nano-ridge. The design of the aSi grating considered the trade-off between coupling strength of the grating and mode overlap with QWs, resulting in a nano-ridge cavity with low lasing threshold. The proposed device model is shown in Figure 2.1.

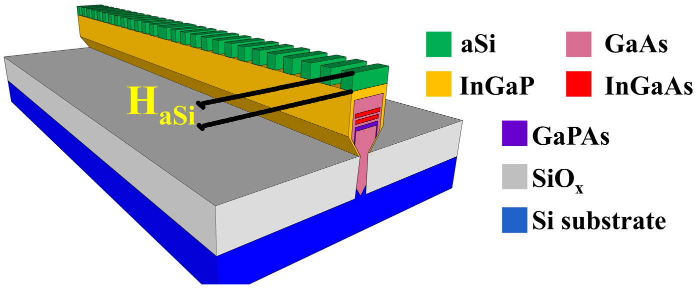

Figure 2.1: The proposed device model of DFB laser with an aSi grating on the top.

This chapter begins with an investigation of the morphological features and the optical characteristics of the epitaxial III-V materials grown using ART and NRE techniques via SEM imaging and PL (Sections 2.1 and 2.2). Next, we calculate the mode polarization and QW confinement through Finite Difference Eigenmode (FDE) simulations (Section 2.3). Grating designs are explored using 3D-FDTD simulations (Section 2.4). Fabrication challenges and optical characterization are discussed in Sections 2.5 and 2.6, with results and conclusions detailed in Sections 2.7 and 2.8.

2.1 Morphological characterization

The dimensions of the rectangular nano-ridges, typically several hundred nanometers in width and height, can be precisely measured via SEM. The QWs, although on the nanometer scale, are observable through SEM after specific post-processing. SEM imaging reveals the structure of as-grown nano-ridges, with Figure 2.2(a) showing a top view of nano-ridge arrays, and Figure 2.2(b)-(e) presenting cross-sectional views for trench widths of 60 nm, 80 nm, 100 nm, and 120 nm, respectively. Increased space between trenches enhances precursor supply, resulting in larger nano-ridge volumes. The most important nano-ridge dimensions are defined in

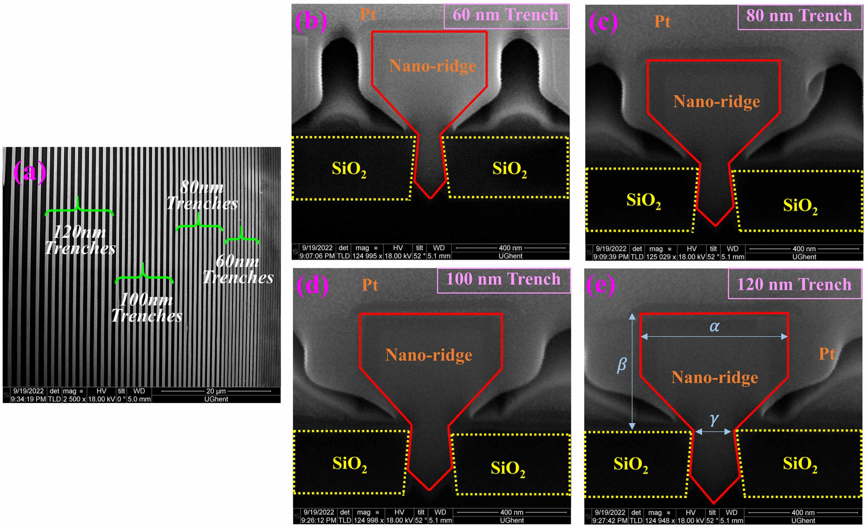

Figure 2.2: (a) Top view SEM image of nano-ridge array with 60 nm, 80 nm, 100 nm and 120 nm trench widths. Cross-sectional SEM image of nano-ridge with 60 nm (b), 80 nm (c), 100 nm (d) and 120 nm (e) trench width. The nano-ridge height, nano-ridge width and trench width are defined in (e).

Designed trench width (nm)	α (nm)	β (nm)	γ (nm)
60	411.3	485.4	87.5
80	471.7	533.0	98.3
100	541.7	520.8	112.5
120	582.5	539.3	132.5

Table 2.1: The nano-ridge height, nano-ridge width and trench width taken from the cross-sectional SEM images.

Figure 2.2(e). The extracted values are summarized in Table 2.1, and are used for subsequent laser design steps described in the remainder of this chapter.

Figures 2.3(a)-(c) give the cross-sectional SEM images of the overall structure after 1 minute wet etching using a solution consisting of 50 % citric acid mixed with 30 % hydrogen peroxide at a ratio of 10:1. Due to the differing etching rate of the different materials constituting the nano-ridge, the InGaP capping layer, the GaAs bulk layer, 2 InGaAs QWs, the GaPAs carrier blocking layer and the defect-rich GaAs trench are clearly visible in Figure 2.3(a). In the enlarged SEM image of Figure 2.3(b) the GaPAs carrier blocking layer and the QWs are clearly visible. The GaPAs carrier blocking layer confines the carriers above the trench and reduces carrier loss in the defect-rich trench region [111]. Figure 2.3(c) details the trench

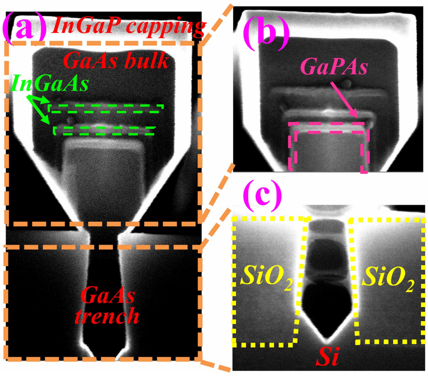

Figure 2.3: (a) Cross-sectional SEM image of nano-ridge structure. (b) Enlarged image of the InGaAs QWs and GaPAs carrier blocking layer. (c) Image of the defect-rich ART-trench region.

structure.

2.2 Photoluminescence characterization

PL, a non-destructive and efficient technique for material characterisation, involves the emission of light under optical excitation, providing insights into material properties such as energy band structure, composition, impurity levels, and temperature behavior [112]. PL measurements, influenced by parameters like excitation energy, and temperature, can be performed under CW or pulsed excitation. Key characteristics in the PL spectrum include spectral width, peak wavelength, and intensity.

We present PL measurements of nano-ridges under CW excitation at room temperature as an initial evaluation of their optical properties. To further investigate carrier lifetime, defects, and surface-related non-radiative recombination, measurements were conducted using pulsed excitation at both room and cryogenic temperatures.

Previous studies [95,107,108,111] investigated nano-ridges with varying ridge size, QW number, and passivation thickness. Here, we focus on one representative sample using the same micro-PL setup as in Ref. [113]. The nano-ridges were excited from the top by a 532 nm CW solid state diode laser. The emission scattered from the nano-ridges was collected from the top and detected with a monochromator and a thermo-electric-cooled InGaAs detector, as previous described [103–105].

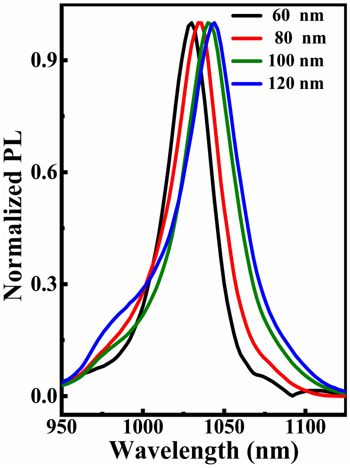

Figure 2.4: The normalized photoluminescence spectra from nano-ridges with the trench widths from 60 nm, 80 nm, 100 nm and 120 nm under 4.20 W/cm^2 CW 532 nm excitation.

Figure 2.4 presents normalized PL spectra from GaAs nano-ridges with two InGaAs QWs for trench widths ranging from 60 nm to 120 nm, at a pump power density of 4.20 W/cm^2. Nano-ridges with smaller or larger trench widths exhibit weaker emissions due to higher surface-to-volume ratios or increased TDs caused by lower aspect ratios and inefficient defect trapping [107]. The spectra display broad peaks (1000–1060 nm), attributed to active $In_{0.2}Ga_{0.8}As$ QWs and non-uniform band structures caused by the strain. The redshift with increasing trench width is believed to arise from changes in indium concentration and/or QW thickness, causing energy shifts in the quantized states. These variations reflect the sensitivity of the epitaxial process to the local growth environment.

2.3 Transversal optical mode

The rectangular configuration of the GaAs/InGaAs nano-ridges naturally allows them to function as optical waveguides, confining light transversely within the high-index GaAs volume. In this section, we calculate the optical modes of the nano-ridges, from which we derive the mode profile, polarization, effective refractive index (n_{eff}) and the QW confinement (Γ_{QW}).

The transverse optical fields are obtained by solving Maxwell's equations [114], with solutions corresponding to different eigenvalues referred to as eigenmodes. Each eigenmode propagates without change as long as the waveguide's transverse shape remains invariant. Based on the direction of their electric and

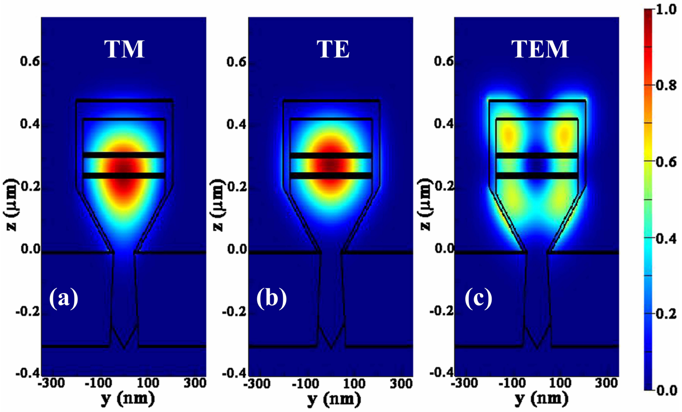

Figure 2.5: The first three optical modes of the nano-ridge with 60 nm trench width. The polarization of the modes is labelled at the top of the images. The simulation was carried out with a FDE solver.

magnetic fields relative to the propagation direction, the two common mode types in integrated waveguides are:

- Transverse electric (TE) modes: the electrical field is dominantly perpendicular to the direction of propagation.

-Transverse magnetic (TM) modes: the magnetic field dominantly perpendicular to the direction of propagation.

The transverse modes, their polarization, n$_{eff}$ and Γ_{QW} are calculated using the commercial FDE solver from Lumerical (now acquired by Ansys) [115]. All calculations were carried out at a wavelength of 1030 nm. The cross-section used in the simulations was based on the nano-ridge geometry (α, nano-ridge width; β, nano-ridge height; γ, trench width) extracted from cross-sectional SEM images (Figure 2.2(e)). The measured dimensions were summarized in Table 2.1.

A key parameter is the confinement factor Γ_{QW}. It defines the fraction of the optical field, which is confined in the QW region. It is calculated by the ratio of the integrated electric field intensity in the QW to the one in the total simulation region,

$$\Gamma_{QW} = \frac{|E_{QW}|^2}{|E_{tot}|^2}$$

Figure 2.5 displays the first three optical modes of a nano-ridge with a 60 nm trench width. Higher-order modes were excluded due to their weak confinement. The first mode, a TM-like mode, extends vertically. The second mode, a TE-like mode, exhibits an effective refractive index (n$_{eff}$) of 3.048 and strongest QW

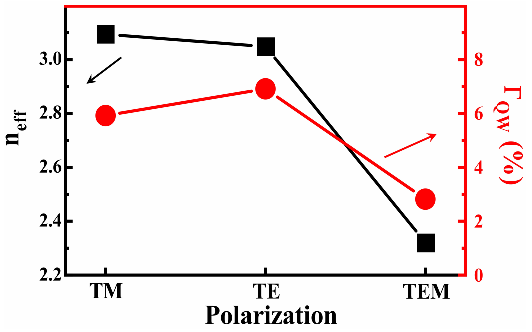

Figure 2.6: The simulated n_{eff} and Γ_{QW} of different optical modes in the nano-ridge with 60 nm trench width. The simulation was carried out with a FDE solver.

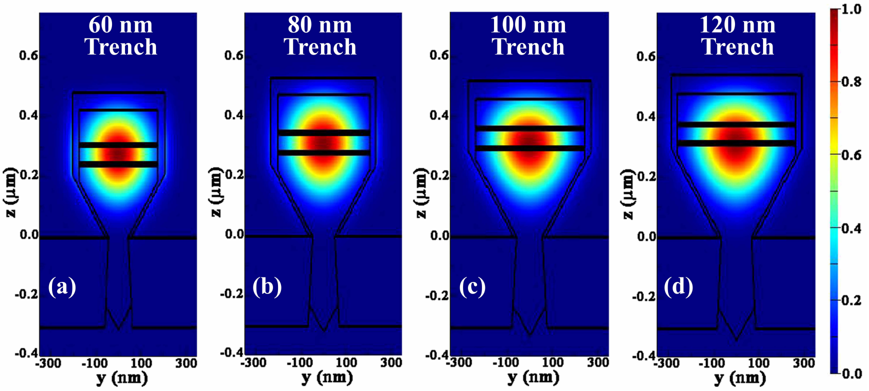

Figure 2.7: The TE-like ground modes of the nano-ridges with trench width 60 nm, 80 nm, 100 nm and 120 nm (left to right). The simulation was carried out with a FDE solver.

confinement (Γ_{QW} = 6.916 %) compared to other modes (Figure 2.6). The third mode, a higher-order TEM-like mode, demonstrates weaker QW confinement (Γ_{QW} = 2.822 %).

Among these modes, the TE-like ground mode emerges as the most favorable for lasing, offering the highest Γ_{QW}. Consequently, this mode was chosen for further analysis. Figure 2.7 and 2.8 depict the mode profiles, as well as the effective refractive index (n_{eff}) and confinement factor (Γ_{QW}) for nano-ridges with trench widths of 60 nm, 80 nm, 100 nm, and 120 nm. As the trench width increases, the nano-ridge size expands, resulting in higher n_{eff}. These modes exhibit strong QW confinement.

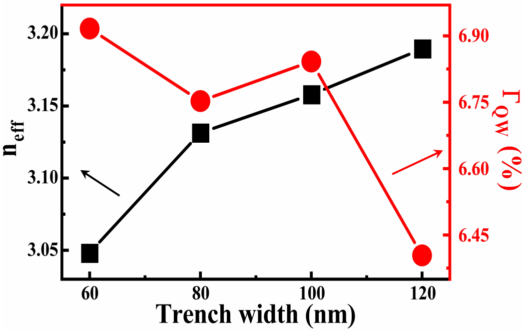

Figure 2.8: The simulated n_{eff} and Γ_{QW} of TE modes in the nano-ridge with 60 nm, 80 nm, 100 nm and 120 nm trench width. The simulation was carried out with a FDE solver.

2.4 λ/4 shifted DFB laser design

In the previous section, we have examined the nano-ridge morphology, PL spectrum and the optical modes confined transversally within the nano-ridges. A laser device requires light confinement in all three dimensions and feedback in the propagation direction, which is typically provided by a laser cavity.

Advanced DFB lasers have been the workhorse of telecom networks for decades due to their low thresholds, stable single-mode operation, and high quantum efficiency. In standard DFB lasers with continuous gratings, two symmetric resonant peaks appear at the edges of the Bragg stopband. Introducing a quarter-wave (λ/4) shift in the grating's center enables single-mode lasing. Therefore, in this section, we explore the design of a λ/4 shifted DFB laser to reduce the lasing threshold.

As discussed in chapter 1, in previous work within the group, lasing from nano-ridge devices using an etched grating to define the cavity was demonstrated [103]. However, the threshold of these devices was still relatively high. One of the suspected reasons is that the etched structure caused damage to the InGaP passivation layer, which introduces carrier loss paths at the GaAs-air interface and within the GaAs bulk. Hence, the assumption is that such defect formation needs to be avoided for improving the laser performance. In this section, a high-refractive-index aSi grating is deposited on top of the nano-ridge rather than etching a grating inside the nano-ridge. The details of the DFB laser design will be given below.

The lasers were designed using 3D-FDTD solver. The device model is shown in Figure 2.1. The grating duty cycle was fixed to 50 % and the period of the aSi grating (Λ) was chosen to match the cavity resonance with the PL peak. From here on, we focus on a 539 nm-high and 582 nm-wide nano-ridge (120 nm trench width). These dimensions are measured via SEM in Figure 2.2. To optimize the trade-off

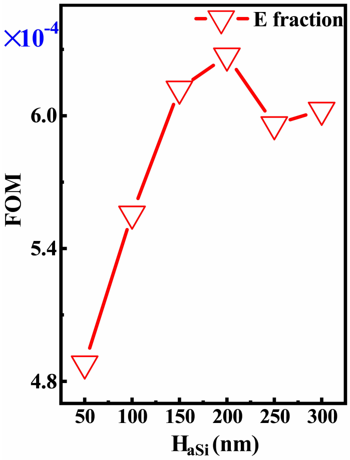

Figure 2.9: Dependence of FOM on H_{aSi}.

between the light interaction with the grating and the mode confinement in the QWs, the height of the aSi grating (H$_{aSi}$) was varied in the simulation. As the figure of merit (FOM) we choose the product $\Gamma_{QW}\Gamma_{aSi}$, with Γ_{aSi} the mode confinement in the grating, defined simalarly as Γ_{QW} earlier on. The simulation was performed with Bloch boundary conditions using a 3D-FDTD solver. Figure 2.9 shows the simulated FOM as function of H$_{aSi}$. The FOM first increases and then decreases with increasing H$_{aSi}$, which is ascribed to a shift of the lasing mode to the thicker high-index aSi grating. Although the FOM reaches a maximum when H$_{aSi}$ = 200 nm, experimentally we found that grating teeth higher than 100 nm tended to bend and touch each other after processing (will be shown in the fabrication section), due to the high aspect ratio. Thus, from here on we mostly focus on devices with H$_{aSi}$ = 100 nm, taking both the height optimization and process tolerances into account.

Figure 2.10 shows simulated spectra for nano-ridge devices with aSi gratings with Λ = 161 nm and different cavity lengths. For devices with 800 and more periods in total, the strength of the resonance peak strongly increases, indicating in this case the grating provides sufficient reflection to form a cavity.

Figure 2.11 plots the simulated Q-factor as function of the number of periods. The Q-factor increases with increasing number of periods due to the reduction of the light leaking at the beginning and end of the grating. Above 800 periods, the Q-factor starts to stabilize because other leakage mechanisms become more important. Therefore, in our final design we choose a grating with 800 periods and H$_{aSi}$ = 100 nm, to achieve a low threshold device. A second-order grating coupler with 200 periods was added at each side of the nano-ridge cavity to facilitate device characterization.

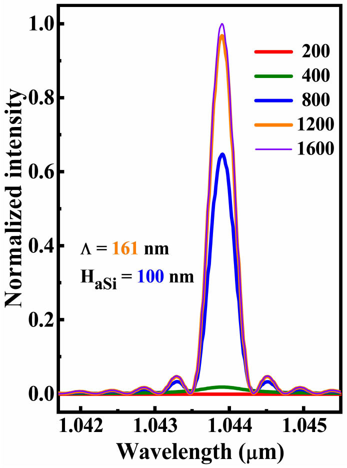

Figure 2.10: Simulated spectrum from the nano-ridge with H_{aSi} = 100 nm and increasing number of periods.

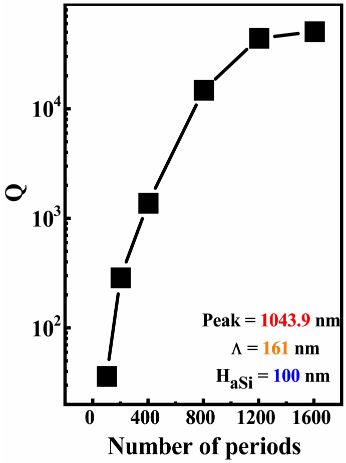

Figure 2.11: Quality factor vs. number of periods.

2.5 Fabrication process

2.5.1 Deposition of aSi with PECVD

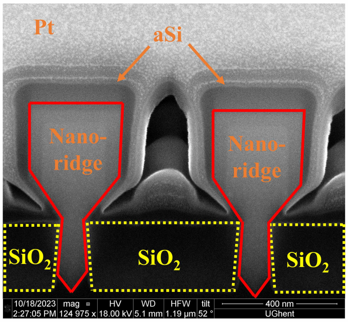

Figure 2.12: The nano-ridge sample with 100 nm aSi thin film full coverage.

A uniform coverage of the nano-ridge by the deposited aSi is critical for subsequent process steps, particularly considering their unique surface topography. A plasma-enhanced chemical vapor deposition (PECVD) process was used to deposit the aSi layer, as shown in Figure 2.12. Despite the irregular shape of the nano-ridges, the aSi layer successfully nucleated and grew uniformly across the entire surface, ensuring complete coverage.

2.5.2 EBL mask and spin coating

The DFB laser design incorporated an aSi grating with 800 periods (400 periods on each side) positioned on the top surface of the GaAs ridge waveguide. A $\lambda/4$ phase shift section was located at the center. The gratings were fabricated using electron-beam lithography (EBL). Figure 2.13 shows the EBL patterning mask, including zoomed-in views of the first- and second-order gratings. The purple rectangles represent the nano-ridge trenches. Each array consists of 10 identical nano-ridge trenches, separated by 11 times the trench width. This DFB cavity design was applied to 2 out of the 10 nano- ridges in each array, with trench widths of 60 nm, 80 nm, 100 nm, and 120 nm (arranged from right to left). This enables single-device characterization and minimize crosstalk.

The resist thickness on top of the nano-ridges was optimized for both EBL and reactive ion etching (RIE) using a $CF_4/H_2/SF_6$ gas recipe. This recipe was chosen for its 1:1 selectivity, ensuring comparable etch rates between HSQ (Hydrogen silsesquioxane, pure FOX-15) and aSi. The resist thickness was evaluated using

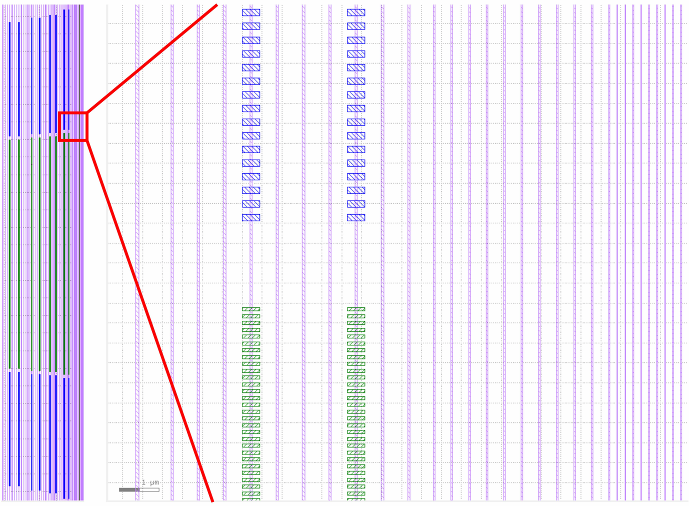

Figure 2.13: The EBL mask used for defining the gratings atop the nano-ridges with trenches varying from 60 nm (right) to 120 nm (left). The trenches of the nano-ridges are shown in purple lines, the DFB gratings and grating couplers are depicted in green and blue, and can be more clearly seen in the magniefied views.

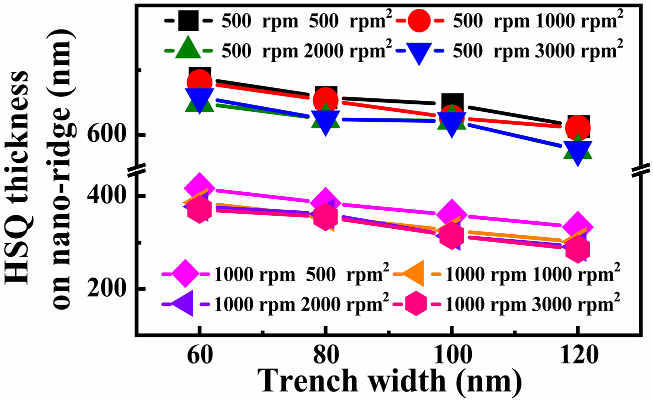

Figure 2.14: The spin coating curve of HSQ thickness atop nano-ridges with 60, 80, 100 and 120 nm trench widths. The spin coating acceleration is between 500 and 3000 rpm/s. The spin coating speed is between 500 and 1000 rpm.

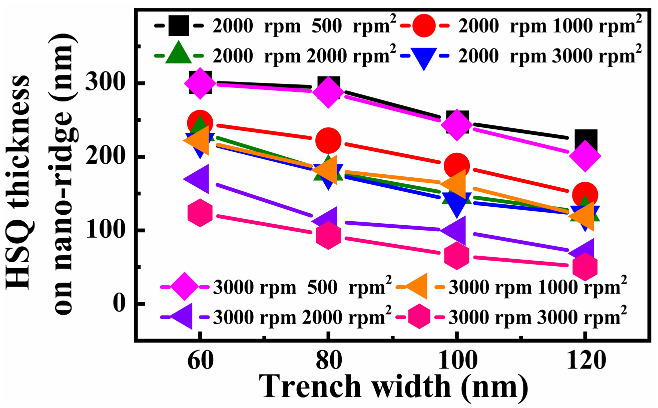

Figure 2.15: The spin coating curve of HSQ thickness atop nano-ridges with 60, 80, 100 and 120 nm trench widths. The spin coating acceleration is between 500 and 3000 rpm/s. The spin coating speed is between 2000 and 3000 rpm.

cross-sectional SEM images, with spin-coating curves displayed in Figure 2.14 and 2.15. Spin coating was performed at various speeds and accelerations to achieve optimal resist thickness on the nano-ridges. A spin speed of 2000 rpm and an acceleration of 1000 rpm/s (describing the rate of increase from 0 to the target speed) was selected. This ensured a minimum HSQ thickness of 150 nm while preserving adequate thinness and high EBL exposure resolution. After spin coating, the HSQ solvent was evaporated through two sequential baking steps at 120 °C and 220 °C, each lasting 2 minutes.

2.5.3 Cured BCB protection layer

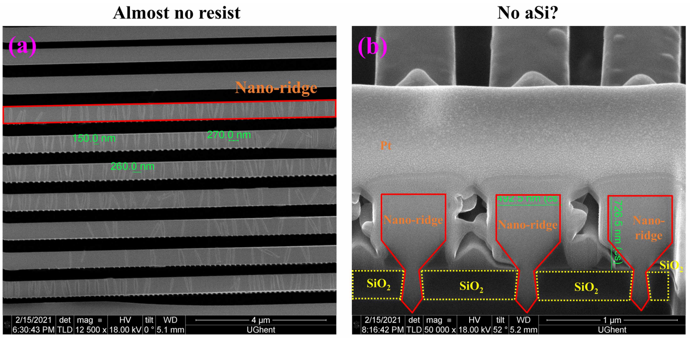

Figure 2.16: The top (a) and cross-sectional (b) SEM images of nano-ridge test sample with 60 nm trench width.

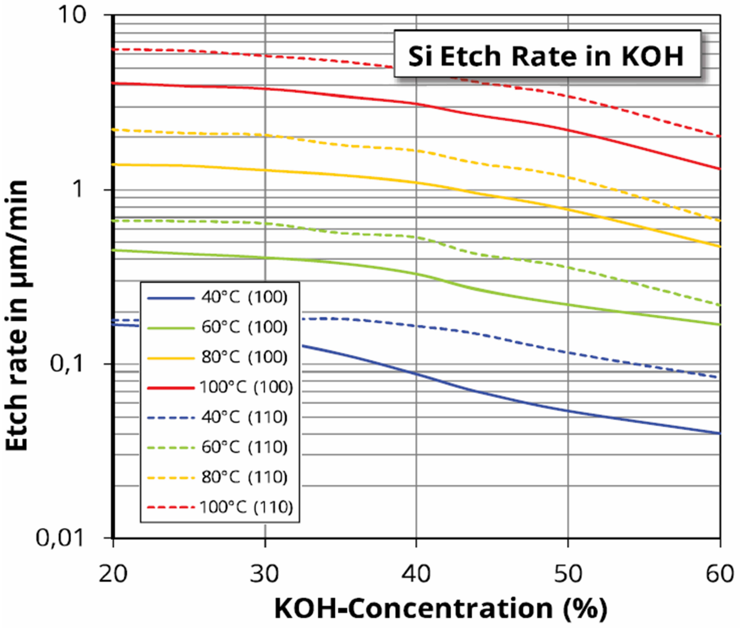

Figure 2.17: The etching rate of Si under different KOH concentrations, etching temperatures and plane facets from Ref. [116]

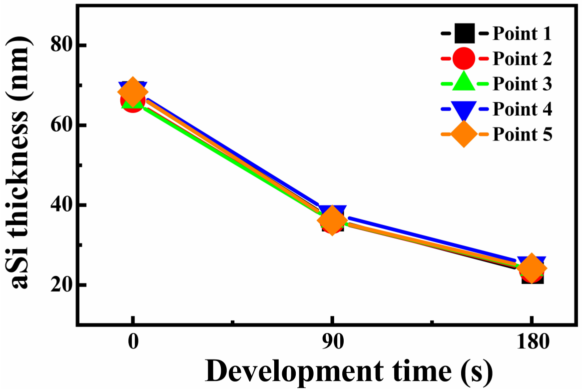

Figure 2.18: The change of aSi thicknesses after dipped into AZ400K for different development times.

Gratings with 800 periods were patterned into the HSQ resist using EBL. The development process involved HSQ developer (AZ400K:DI water = 1:3) and a stopper (DI water), each applied for 3 minutes and 40 seconds. However, numerous bubbles formed during development, leading to the complete removal of the aSi thin film, as shown in the SEM images in Figure 2.16. This issue was attributed to a chemical reaction between the KOH (Potassium Hydroxide) present in the AZ400K developer and the aSi thin film, represented by the following reaction:

$$Si + H_2O + KOH = K_2SiO_3 + H_2$$

Supporting evidence for this reaction is provided in Figure 2.17 [116], which compares the etching rates of (100) and (110) crystallographic planes in silicon crystals under varying temperatures. However, the current study utilizes an amorphous silicon (aSi) thin film, which exhibits different behavior. To further investigate this issue, the change in aSi thickness was measured using a test sample (70 nm aSi - 300 nm SiO_x - Si substrate) immersed in AZ400K for varying development times. Figure 2.18 shows the dramatic decrease in thickness measured at five points on the sample, highlighting the removal of the aSi layer.

To mitigate this issue, a $\sim$ 50 nm BCB (benzocyclobutene) layer was spin-coated and cured, serving as a protective coating before applying a $\sim$ 150 nm HSQ resist layer. The curing recipe is provided in Table 2.2. Cured BCB was chosen for its resistance to the developer.

Step	Duration(hh:mm:ss)	Temperature (°C)	Temperature increasing rate (°C/min)
1	0:02:00	20	10
2	0:20:00	20	0
3	0:19:03	100	4.2
4	0:15:00	100	0
5	0:13:53	150	3.6
6	0:20:02	150	0
7	0:18:00	180	1.67
8	0:15:00	180	0
9	0:59:10	280	1.69
10	0:59:10	280	0
11	0:44:57	75	-4.56
12	0:05:00	25	-10

Table 2.2: BCB curing recipe.

2.5.4 Critical HSQ thickness and etching process

2.5.4.1 Critical HSQ thickness

In section 2.5.2, the spin coating curve of HSQ was discussed and the optimal thickness was determined as $\sim$ 150 nm, considering both HSQ/BCB and HSQ/aSi etching selectivity into account. Thicker resist is theoretically more favorable for the etching process. However, higher HSQ grating teeth tend to bend and touch each other (Figure 2.19) after the development due to the high aspect ratio and weak adhesion between HSQ and cured BCB. This limited HSQ thickness restricts the aSi height used for the gratings. For this reason, a grating height of 100 nm was employed for simulations in the previous section, despite a larger FOM associated with higher aSi gratings.

2.5.4.2 Etching process

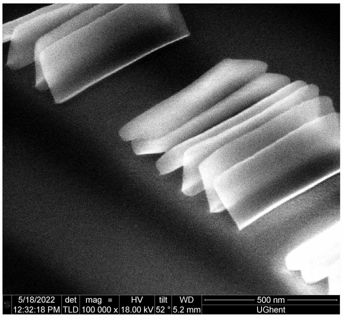

Figure 2.19: 52-degree tilted SEM image of developed HSQ on nano-ridge.

Next, the etching process was optimized using test samples (150 nm HSQ - 55 nm BCB - 100 nm aSi - 300 nm buffer oxide - Si substrate). The structures patterned in the HSQ resist were transferred to the aSi layer by reactive ion etching of the BCB layer and the aSi layer with SF_6/O_2 and $CF_4/H_2/SF_6$, respectively. Etching quality was assessed based on surface roughness and verticality. Tilted and cross sectional SEM imaging (Figure 2.20 and 2.21) was used to evaluate the impact of varying the O_2 flow on the quality of the BCB etching. Sidewalls etched with an O_2 flow rate of 30 sccm exhibited notably reduced striped and dot-like surface features (Figure 2.20) and more vertical profiles (Figure 2.21) compared to other conditions. This optimized O_2 flow was thus selected for subsequent structure definition. A similar assessment was conducted for the effect of varying the H_2 flow on the aSi etching, as shown in Figure 2.22 and 2.23. Etching with H_2 = 9 sccm

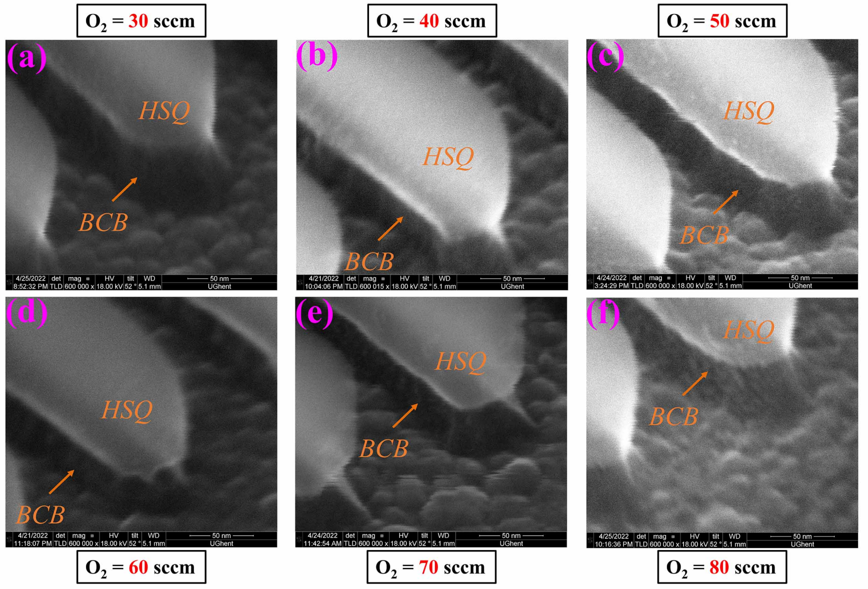

Figure 2.20: (a) 52-degree tilted SEM image of etched BCB layer on the test samples, for various O_2 flows.

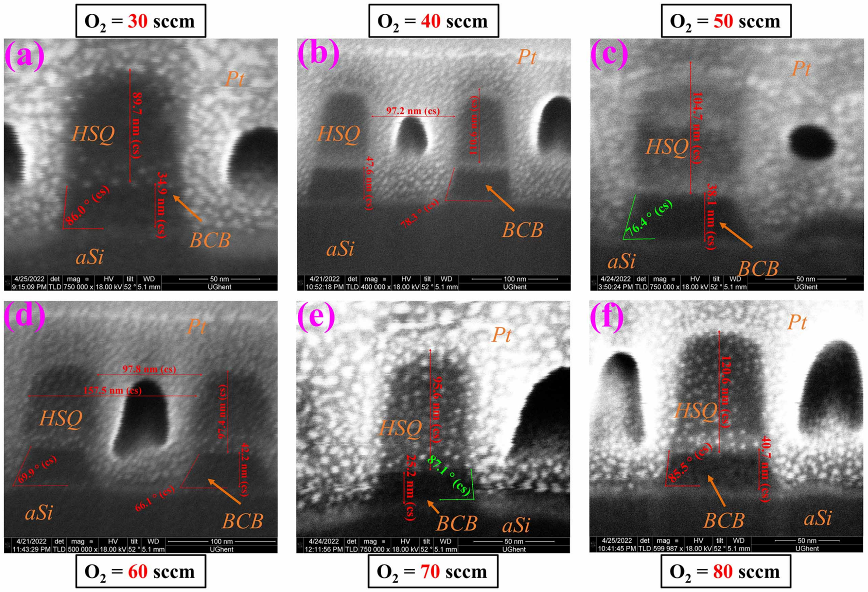

Figure 2.21: (a) Cross-sectional SEM image of etched BCB layer on the test samples, for various O_2 flows.

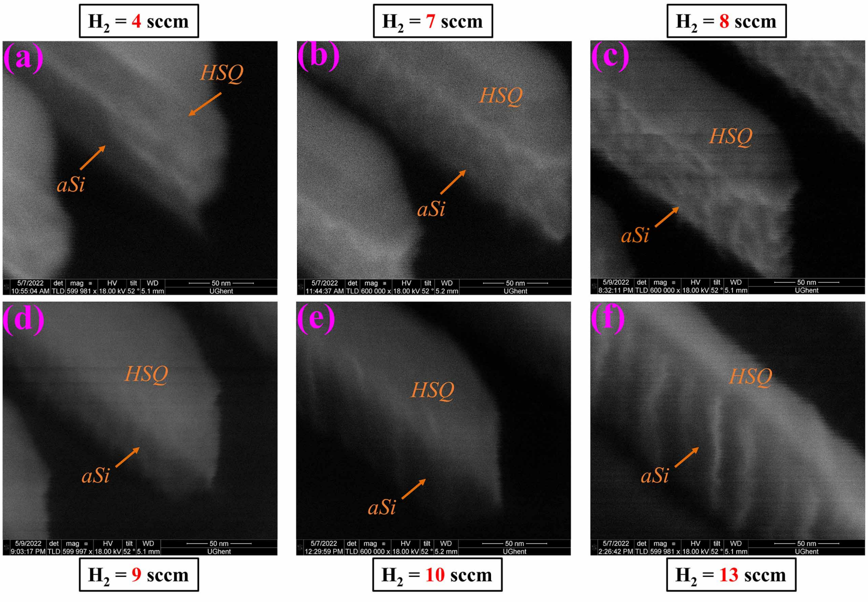

Figure 2.22: (a) 52-degree tilted SEM image of etched aSi layer on the test samples, for various H_2 flows.

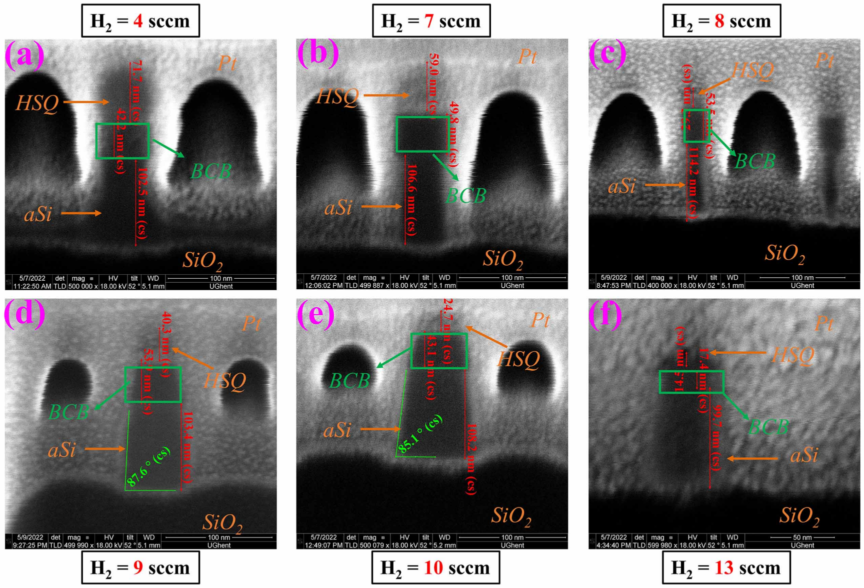

Figure 2.23: Cross-sectional SEM image of etched aSi layer on the test samples, for various H_2 flows.

resulted in improved sidewall roughness and verticality, making it the preferred condition for defining aSi grating structures in the later fabrication.

To ensure consistency, etching was performed under stable conditions rather than during the plasma build-up process. This is particularly important for small structures, as they are highly sensitive to gas flow fluctuations and etching environment variations. The finally selected etching recipes for DFB laser fabrication are summarized in Table 2.3.

	BCB etching recipe	aSi etching recipe
Gases	O_2/SF_6	$CF_4/H_2/SF_6$
Flow	30/5	100/9/3
Chamber pressure (mTorr)	10	20
RF power (W/V)	150 W	420V
Temperature	18	18

Table 2.3: The etching recipes selected for the DFB lasers fabrication.

In the end, two optimized etching recipes were used for the DFB laser fabrication. Figure 2.24(a) shows a 52-degree tilted SEM view of the fabricated devices with the 200 period second-order gratings clearly visible at the bottom-right corner. Figure 2.24(b) is a zoomed-in image of the region with the first-order grating and Figure 2.24(c) shows that the sidewalls of the aSi grating are vertical.

In summary, the aSi film was deposited on the nano-ridge chips by PECVD after aceton, isopropyl alcohol (IPA) and DI water cleaning. A $\sim$ 50 nm cured BCB layer was added as a protection layer before spin coating $\sim$ 150 nm HSQ electron beam resist. This protection layer is critical given the reaction between the aSi layer and the HSQ developer (AZ400K:DI water = 1:3). Then, gratings with 800 periods were patterned using EBL into the HSQ resist. The patterned structures were transferred from the HSQ resist to the aSi layer by reactive ion etching of the BCB layer and the aSi layer with SF_6/O_2 and $CF_4/H_2/SF_6$, respectively. Figure 2.25(a) and 2.25(b) illustrate the process flow and provide a top-view schematic of the device.

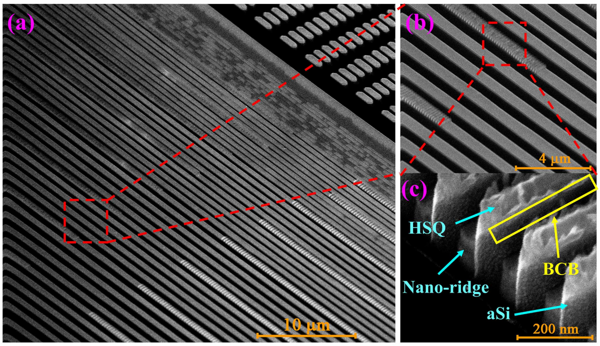

Figure 2.24: (a) 52-degree tilted SEM image of DFB lasers with 60, 80, 100, 120 nm trench widths. (b) Zoomed-in image of the region with the first order grating on nano-ridge with 120 nm trench width. (c) Zoomed-in image of the grating.

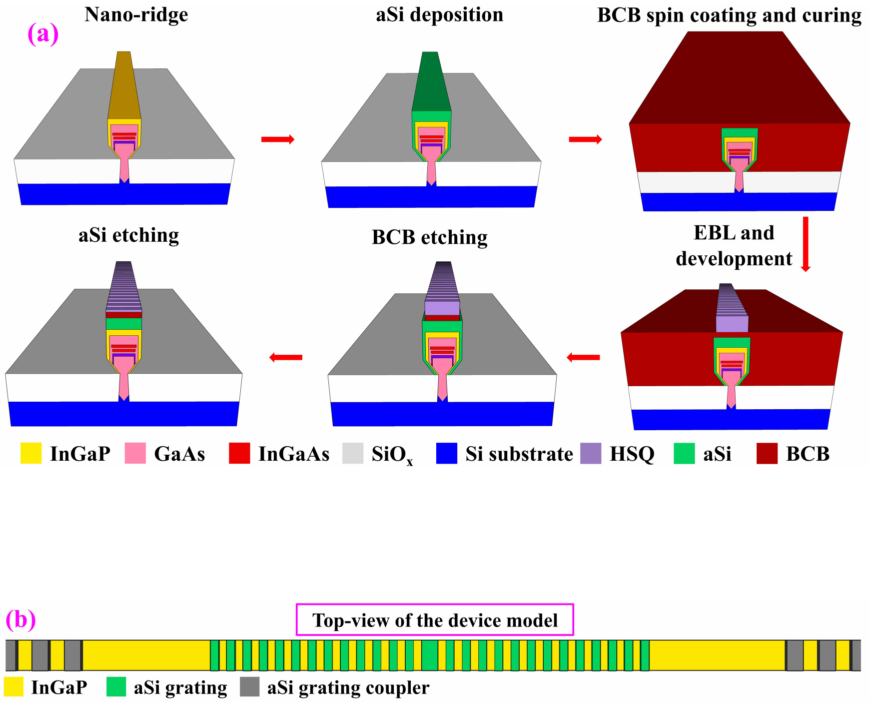

Figure 2.25: (a) Process flow for fabrication of the DFB laser with an aSi grating atop the nano-ridge. (b) Top-view schematic of the device.

2.6 Optical characterization

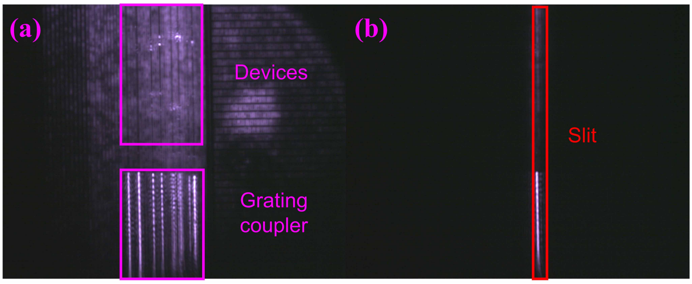

Figure 2.26: (a) Microscope image of a full array of devices excited simultaneously by a 532 nm pulsed pump. (b) Microscope image sample excited with rectangular aperture to select a single DFB laser.

The devices were excited by a Nd:YAG 532-nm nanosecond pulsed laser (7 ns pulse width, 938 HZ repetition rate) at room temperature. The emission from the devices was collected and detected with the same monochromator and InGaAs detector, as mentioned in the section 2.2. Figure 2.26(a) shows a microscope picture of a full array of devices excited simultaneously by a pump spot with a Guassian profile and a full width at half maximum of 400 µm. To characterize the individual devices, a rectangular aperture was utilized to control the pump beam shape, as shown in Figure 2.26(b). Figure 2.27(a) shows the PL spectrum from the DFB laser having an aSi grating with H_{aSi} = 100 nm and Λ = 161 nm, under different pulsed pump power densities. The 1044 nm lasing peak becomes apparent when the pump density reaches 2.5 kW/cm^2, and the peak intensity increases strongly with the further increase of the pump density. At a pump density of 35 kW/cm^2, the lasing peak reaches a SMSR of more than 35 dB. The linewidth of the laser, obtained from a Gaussian function fitting as shown in Figure 2.27(b), is 1.5 nm and likely limited by the pulsed operating regime. In this regime, thermal fluctuations, non-equilibrium carrier dynamics, and mode competition contribute to spectral broadening. Additionally, averaging over pulses during measurement can further increase the observed linewidth.

The reported power density in kW/cm^2 refers to the peak output power density of the nanosecond (ns) laser during a pulse cycle. It is calculated theoretically using the measured average power from the power meter, following the equation:

$$P_{den} = \frac{P_{avg}}{PPR \cdot FWHM \cdot \pi \cdot r^2} \cdot 0.804 \times 10^8$$

where P_{den}, P_{avg}, PPR, $FWHM$ and r are the peak power density, average

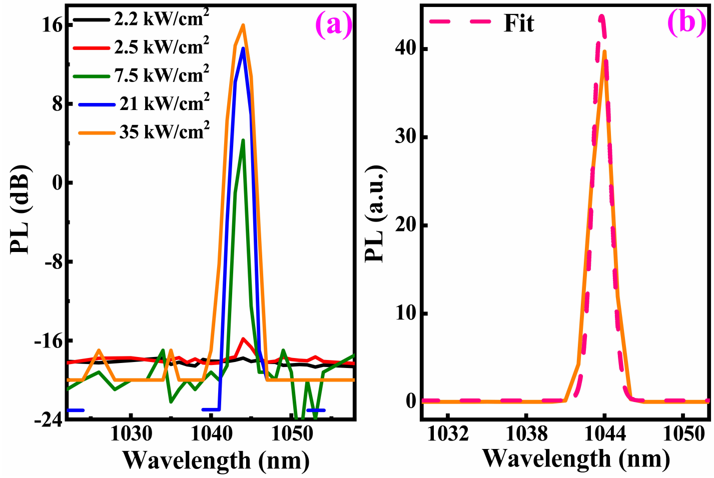

Figure 2.27: (a) PL spectrum from the DFB laser under different pulsed pump power densities. (b) PL spectrum on linear scale with Gaussian function fitting from the same DFB laser under 35 kW/cm^2.

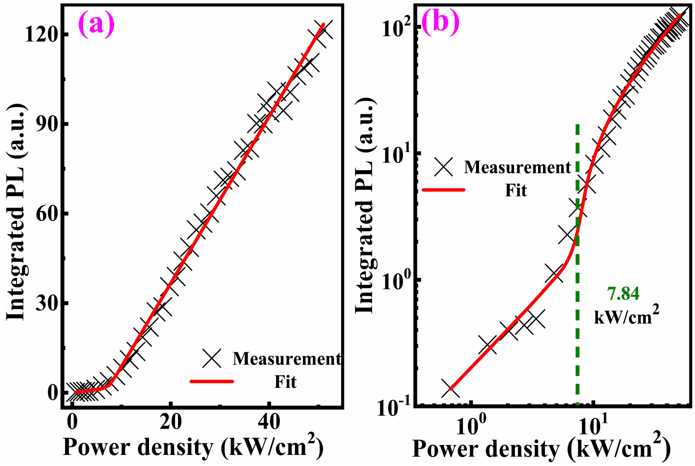

Figure 2.28: Light in - Light out curve on linear (a) and logarithmic (b) scale of the same DFB laser in Figure 2.27.

power, pulse repetition rate, full width at half maximum of the pulse, and pump spot radius. The conversion factor 0.804×10^8 ensures unit consistency.

Figure 2.28 shows the light in (pump power density) - light out (integrated PL) curve on a linear (a) and a logarithmic (b) scale for the same measured laser. The integrated wavelength range is from the peak wavelength ± 1 nm. A clear change of slope is a signature of the lasing turn-on. The threshold density is 7.84 kW/cm^2 (48 µJ/cm^2). This value is obtained from the second order derivative of the light in - light out curve on linear scale [117]. This threshold is $\sim$ 5 times smaller than the value for the nano-ridge with an etched grating (33.4 kW/cm^2) [103]. The light in - light out curve on both linear and log scale are fitted to the rate equations [118, 119] giving a value $\beta \sim 0.9$ % for the coupling efficiency from the spontaneous emission to the cavity mode. In theory, a higher β value is beneficial to obtain a lower lasing threshold value. However, the β value is almost the same as for the nano-ridge laser with an etched grating. Thus, the coupling efficiency β is not the main reason for the lower lasing turn-on threshold value.

Note that in principle the coupling efficiency β could be improved by optimizing the nano-ridge dimensions. Simulations show that this leads to a strongly reduced overall cross-section, which is not necessarily favorable in terms of overall laser design and might e.g. lead to considerably lower output powers.

To better understand the origin of the lowered threshold, time-resolved photoluminescence (TRPL) measurements were carried out, as these can provide insight in extra carrier losses introduced by the etched grating at the GaAs-air surfaces and in the QWs. The nano-ridges were excited by a Ti:Sapphire ultrafast laser (35 fs pulse width, 8 MHZ repetition rate) at both room temperature (R.T.) and cryogenic temperature(Cryo., 5K), using the similar setup as in Ref. [113]. The emission from the nano-ridges was collected and detected with a monochromator and a superconducting nanowire single photon detector.

Figure 2.29 presents the decay curve for the room temperature emission at 1044 nm from a nano-ridge with and without etching. A single exponential decay function is utilized for fitting. The fitted lifetime value of the etched nano-ridge is 5 times smaller than the one without, 76 ps compared to 379 ps. This is consistent with the reduction in threshold for the lasers with an aSi grating vs. those with an etched grating (5x) [103].

To further investigate the origin of the decreased lifetime, the measurements were repeated at cryogenic temperature (5K), see Figure 2.30. At this temperature, the carriers are expected to have insufficient thermal energy to escape the InGaAs QWs and hence the measured lifetime only should depend on the material quality of the QWs, and not on the surface defects. The lifetime for the nano-ridge with etched

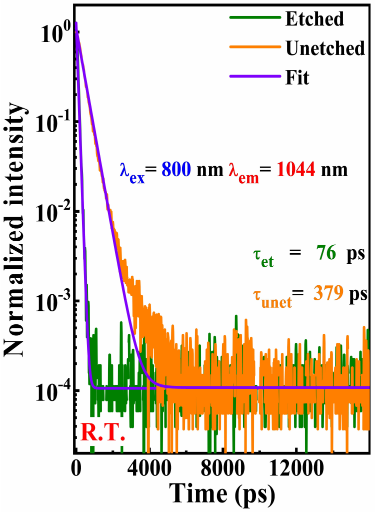

Figure 2.29: Decay traces of the 1044 nm and 1000 nm emission from nano-ridges with and without etching under 800 nm pulsed pump at room temperature.

grating is now 153 ps, double that of the one at room temperature, but still smaller than the one without etching (379 ps and 475 ps at room temperature and cryogenic temperature, respectively). This demonstrates the etching introduces extra carrier loss paths. In summary, we believe the decreased lifetime for the devices with etched grating originates both from surface non-radiative recombination centers at the GaAs-air interface, which is exposed by etching the InGaP passivation layer [111], and by defects introduced in the QWs by the high-impact ions used in the plasma etching process.

Previously, we reported InP [120] and InGaAs/InP [121] DFB-lasers with etched gratings exhibiting laser thresholds of 2143 kW/cm^2 and 760 kW/cm^2. The DFB laser reported here, with an aSi grating on top, demonstrates a threshold of 7.48 kW/cm^2, more than two orders of magnitude lower. This superior performance can be attributed to the following reasons: 1) the high quality of the epitaxial material and the incorporation of an extra InGaP passivation layer suppressing non-radiative recombination via surface states. 2) the absence of damage to the nano-ridge material during aSi grating fabrication. 3) enhanced carrier confinement inside the QW layers. Leveraging LART techniques, Han and Xue, et al. reported InP FP lasers, distributed Bragg reflector (DBR) laser and DFB lasers with an etched grating on the two sides [98, 99, 122, 123]. These devices had a lasing threshold ranging from 16 μJ/cm^2 to 40 μJ/cm^2. In this case ultrashort pulses (100 fs) were used, making a direct comparison not straightforward. In contrast, given that the 7 ns pump pulse width used here is much larger than the measured lifetime,

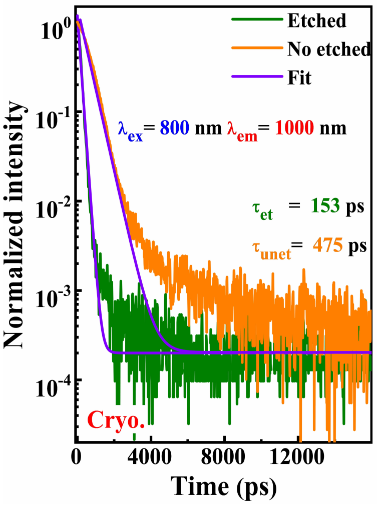

Figure 2.30: Decay traces of the 1044 nm and 1000 nm emission from nano-ridges with and without etching under 800 nm pulsed pump at cryogenic temperature.

the DFB laser with aSi grating can be considered to lase under quasi-continuous pump conditions.

2.7 Threshold discussion

To further explore how this improved lifetime influences the device's threshold, we study the threshold condition and compare with our earlier results.

In general, the threshold condition is given by:

$$n\Gamma_{QW} g_{th} = \alpha_m + \alpha_i \tag{2.1}$$

With n the number of QWs, Γ_{QW} the confinement factor per QW, g_{th} the threshold material gain, α_m the mirror losses and α_i average internal losses. We explicitly take into account the number of QWs here, as we compare our current device containing 2 QWs with the previous device [103] having 3 QWs.

The mirror losses are determined by the laser's κL, where κ and L are the coupling coefficient and the length of the DFB cavity. κL is a measure for the grating reflection and was estimated to be 7.19 for the aSi grating device using [124]

$$\kappa L = \sqrt{(\frac{\Delta\lambda\pi n_{eff}L}{\lambda_{Bragg}^2})^2 - \pi^2} \tag{2.2}$$

In this equation, $\Delta\lambda$, n_{eff} and λ_{Bragg} are the stopband width, the effective refractive index of the lasing mode and the Bragg wavelength. All of them can be obtained from a numerical simulation. The large κL indicates the aSi grating provides a strong mirror reflection, resulting in limited light loss at both cavity ends. For the etched grating device κL is 3.3. In both cases these values are very high and as such we can assume that the mirror losses are negligible compared to the internal losses, such that equation (2.1) simplifies to:

$$n\Gamma_{QW}g_{th} \approx \alpha_i \tag{2.3}$$

From the threshold material gain g_{th}, we can derive the required threshold carrier density N_{th}. To relate the carrier density with the carrier generation rate and ultimately the pump density, we start from the rate equation for the carriers:

$$\frac{dN}{dt} = G - (AN + BN^2 + CN^3) \tag{2.4}$$

where N, G, A, B and C are the carrier density, the net optical generation rate, the linear non-radiative recombination rate, the bimolecular recombination coefficient and the Auger recombination coefficient. It is common to combine the effect of all carrier recombination mechanisms in a single lifetime τ, simplifying the equation to:

$$\frac{dN}{dt} = G - \frac{N}{\tau} \tag{2.5}$$

However, one must consider that the carrier lifetime τ is then dependent on the carrier density in principle. The generation rate is given by:

$$G = \frac{\eta_{ex}P}{nt_{QW}h\nu} \tag{2.6}$$

With η_{ex} the external quantum efficiency, P the pump density, t_{QW} the thickness of the QW, h Planck's constant and ν the emission frequency. Given that 7 ns pump pulse width is much larger than all other time constants in the system, we can assume to operate under quasi-continuous pump conditions, which simplifies equation (2.5) as

$$G = \frac{N}{\tau} \tag{2.7}$$

Combining equation (2.6) and (2.7), we can calculate the threshold as:

$$P_{th} = \frac{N n t_{QW} h\nu}{\eta_{ex}\tau} \tag{2.8}$$

In a first order approximation, we can connect the material gain and the carrier density as:

$$g = a(N - N_0) \tag{2.9}$$

From which we finally find:

$$P_{th} = \frac{\alpha_i}{\tau}\left[\frac{t_{QW} h\upsilon N_{th}}{a\Gamma_{QW}\eta_{ex}(N_{th} - N_0)}\right] \tag{2.10}$$

While this relation is simplified a lot – in reality a more complex relation should be considered to connect gain and carrier density – it shows that in first order, the threshold density is independent of the number of QWs but is dominated by the carrier lifetime and the internal losses of the laser cavity. This equation clearly shows that the dramatic decrease of lifetime τ after etching, as shown in Figure 2.29, can indeed explain the strong difference in threshold for the aSi grating and etched grating based devices.

2.8 Conclusion

A 100 nm high, 161 nm period aSi grating with 800 periods was integrated on top of a GaAs nano-ridge directly grown on a standard 300 mm Si wafer. This approach allowed to demonstrate lasing with strongly lowered threshold compared to the device with an etched grating, which suffers from additional non-radiative recombination [103, 120, 121], and compared to the devices with a metal grating on top [104, 105], which suffer from increased propagation losses. The room temperature photoluminescence spectrum shows single mode laser operation with more than 35 dB side-mode suppression ratio and 7.84 kW/cm^2 lasing threshold. This lasing threshold is $\sim$ 5 times smaller than for a DFB laser with a grating etched into the nano-ridge. This is ascribed to the fact that the aSi grating fabrication process allows to avoid extra carrier loss paths from surface state defects at the

GaAs-air interface and from damage in the quantum wells active region due to the high-energy ions involved in the plasma process used for the etched gratings. This demonstration of a nano-ridge laser with low threshold proves the high quality of the III-V-on-silicon epitaxial material again and opens up the road towards achieving electrically driven devices.

3

Ultra-compact InGaAs/GaAs nano-ridge laser

The exponential growth of data traffic requires efficient chip-to-chip and on-chip optical interconnection methods with low energy consumption and high-density integration. Ultra-compact and low-threshold III-V semiconductor lasers are promising as light source for the silicon photonic platform due to their small footprint and low energy consumption.

In Chapter 2, we employed an aSi grating atop the nano-ridge to avoid introducing extra carrier loss mechanisms, which were present in our previous DFB lasers designs featuring etched gratings [103] or metal gratings on top [104, 105]. These lasers demonstrate excellent threshold performance, supporting their potential for low energy operation. However, these lasers suffer from small interaction with the optical mode and hence long cavities (over 100 µm). This limits integration density, emphasizing the need for footprint reduction and miniaturization.

To address this, Chapter 3 introduces high-refractive-index aSi gratings deposited on the sidewalls of nano-ridges, enhancing interaction with the guided mode and enabling cavity dimension reduction. The proposed device model is shown in Figure 3.1. This modification is a step toward practical on-chip laser applications. From Sections 3.1 to 3.7, we explore the following:

- Sections 3.1-3.2: Characterization of morphological features and optical properties using SEM imaging and PL spectroscopy to determine ridge dimensions and QW emission wavelengths.
- Section 3.3: Optical mode analysis using FDE simulations.
- Section 3.4: Design and comparison of compact nano-ridge lasers with sidewall gratings (SG) and top gratings (TG).
- Sections 3.5-3.7: Fabrication challenges, optical characterization, results, and conclusions.

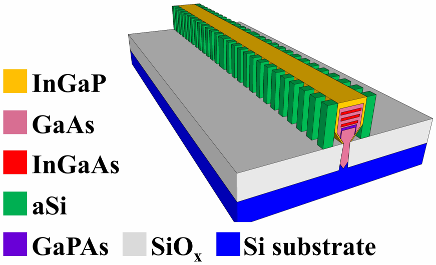

Figure 3.1: The proposed device model of DFB laser with an aSi grating on the sides.

3.1 Morphological characterization

To obtain the nano-ridge dimensions needed for the laser design, we performed top and cross-sectional SEM imaging (Figure 3.2). The sizes of the nano-ridges with 60 nm, 80 nm, 100 nm and 120 nm trench width are summarized in table 3.1. The nano-ridge dimensions are defined similarly to those in Figure 2.1.

Figure 3.3(a)-(b) give the cross-sectional SEM images of the overall structure after preparing the sample using the same solution described in Section 2.1. The InGaP capping layer, the GaAs bulk layer, the InGaAs QWs, the GaPAs carrier blocking layer and the defect-rich GaAs trench are clearly visible in Figure 3.3. Unlike the nano-ridge samples in Chapter 2, these include three QW layers, as shown in Figure 3.3(b).

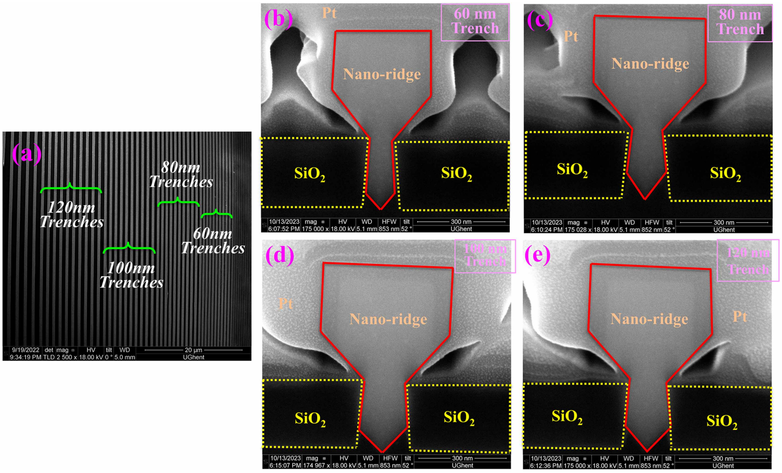

Figure 3.2: (a) Top view SEM image of nano-ridge array with 60 nm, 80 nm, 100 nm and 120 nm trench widths. Cross-sectional SEM image of nano-ridge with 60 nm (b), 80 nm (c), 100 nm (d) and 120 nm (e) trench width. The nano-ridge height, nano-ridge width and trench width are defined similarly to those in Figure 2.1.

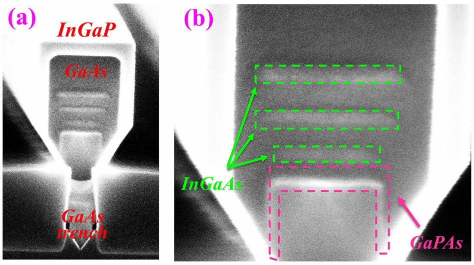

Figure 3.3: (a) Cross-sectional SEM image of nano-ridge structure. (b) Enlarged image of the InGaAs QWs and GaPAs carrier blocking layer.

Designed trench width (nm)	α (nm)	β (nm)	γ (nm)
60	333.8	452.1	75
80	378.3	459	91.7
100	395.8	510.2	110.4
120	447.9	502.3	133.3

Table 3.1: The nano-ridge height, nano-ridge width and trench width taken from the cross-sectional SEM images.

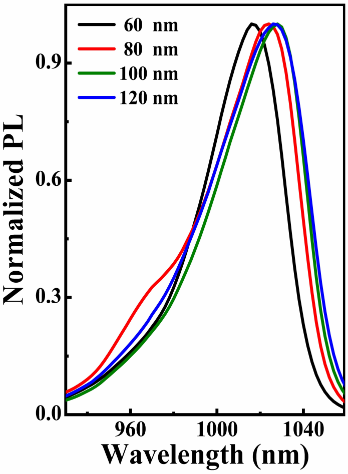

Figure 3.4: The normalized PL spectra from nano-ridges with trench widths 60 nm, 80 nm, 100 nm and 120 nm under 4.20 W/cm^2 CW 532 nm excitation.

3.2 Photoluminescence characterization

The nano-ridge arrays were optically pumped using a 532 nm CW laser at 4.20 W/cm^2, consistent with conditions in Section 2.2. Normalized PL spectra (Figure 3.4) reveal a broad emission peak between 1000 nm and 1060 nm, attributed to the active $In_{0.2}Ga_{0.8}As$ QWs. The redshift observed in the PL peak is explained by mechanisms similar to those in Section 2.2. This wavelength region serves as the focus for cavity design in the next section.

3.3 Transversal optical modes

Simulations of the optical modes supported in the nano-ridges were performed using an FDE solver, as described in Section 2.3. Figure 3.5 shows the first three

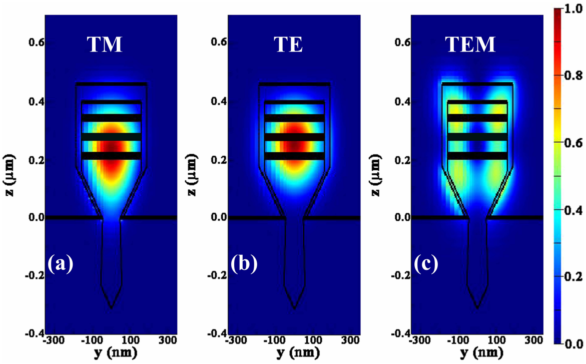

Figure 3.5: The first three optical modes of the nano-ridge with 80 nm trench width. The polarization of the modes is indicated on top of the images. The simulations were carried out with an FDE solver.

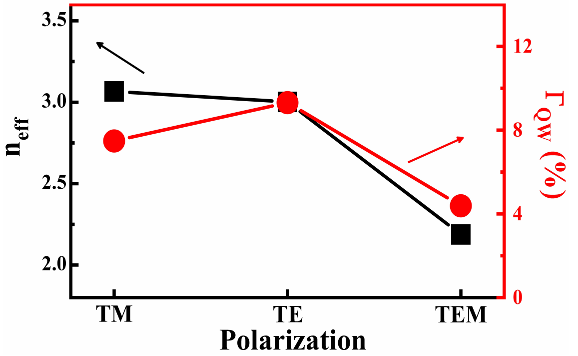

Figure 3.6: The simulated n_{eff} and Γ_{QW} of different optical modes in the nano-ridge with 80 nm trench width. The simulation was carried out with an FDE solver.

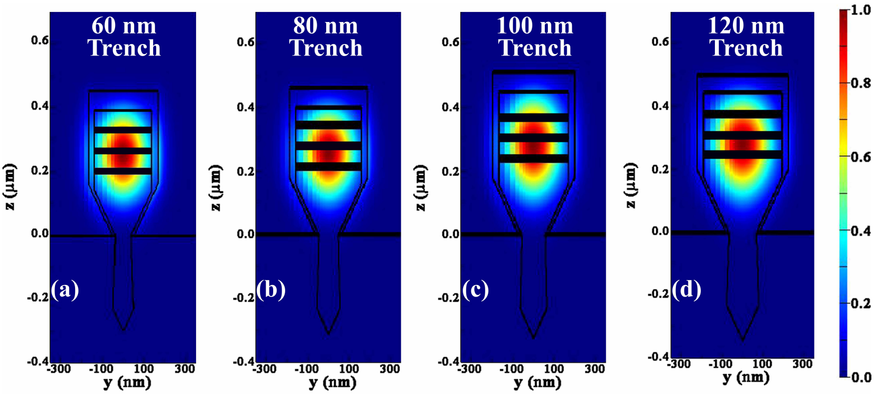

Figure 3.7: The TE-like ground modes of the nano-ridges with trench width 60 nm (a), 80 nm (b), 100 nm (c) and 120 nm (d). The simulation was carried out with an FDE solver.

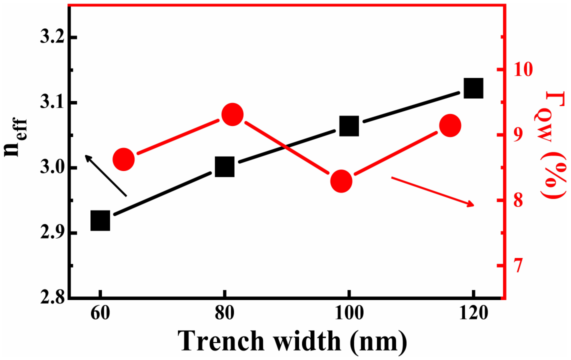

Figure 3.8: The simulated n_{eff} and Γ_{QW} of TE modes in the nano-ridge with 60 nm, 80 nm, 100 nm and 120 nm trench width. The simulation was carried out with a FDE solver.

optical modes for nano-ridges with a 60 nm trench width, including a TM-like, a TE-like, and a higher-order TEM mode. The TE-like ground mode remains the most promising candidate for lasing due to its high QW confinement factor (Γ_{QW} = 9.312 %), as can be seen in Figure 3.6. Figure 3.7 and 3.8 show the TE-like modes and their n_{eff}, Γ_{QW}.

3.4 Ultra-compact DFB laser design

In Chapter 2, we demonstrated lasing from nano-ridge devices with a grating on top (TG). However, insufficient grating modulation limited the coupling efficiency and prevented compact device footprints. To address this, in this chapter we place a grating on the side of the nano-ridges (SG), aiming to enhance light-matter interaction and achieve further miniaturization. The detailed design of the DFB laser is discussed below.

3.4.1 Comparison of top and side grating

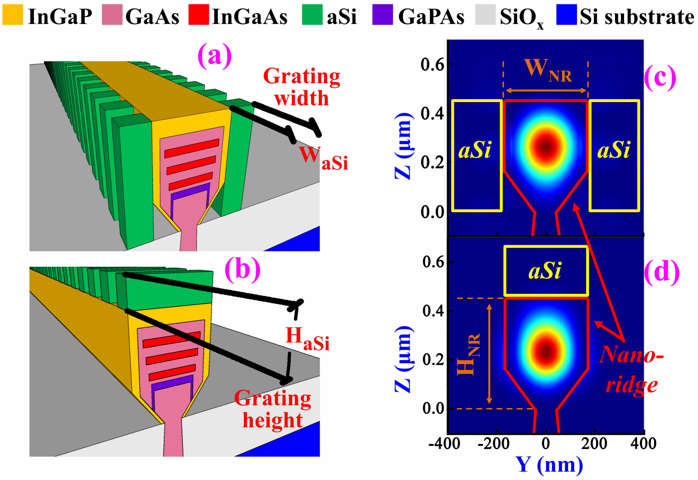

Figure 3.9: Device models with the definition of W_{aSi}, H_{aSi} for the (a) SG and (b) TG. The lowest order transverse electric (TE)-like mode from the models with (c) W_{aSi} = 200 nm SG and with (d) H_{aSi} = 200 nm TG.

For the design of the sidewall grating laser cavities (SGL) and top grating laser cavities (TGL), we used a 3D-FDTD solver with Bloch boundary conditions. The simulation models for both types of devices and the definition of the most relevant parameters, the grating width W_{aSi} (for SGL) and grating height H_{aSi} (for TGL), are depicted in Figure 3.9(a) and 3.9(b). Figure 3.9(c) and 3.9(d) show the lowest order transverse electric (TE)-like modes for both device models with W_{aSi} = 200 nm for the SGL and H_{aSi} = 200 nm for the TGL. The nano-ridge itself has a height H_{NR} = 452 nm and width W_{NR} = 334 nm. The trench width is 60 nm. The field distribution was calculated, assuming a 50 % duty cycle for the gratings, with the cross-section taken in the high-index region. Figure 3.9(c) and 3.9(d) show that the mode is strongly confined inside the nano-ridge.

3.4.2 Cavity simulation

	Grating type	W_{NR} (nm)	H_{NR} (nm)	W_{aSi}/H_{aSi} (nm)
S1	SG	200	452	200
S2	SG	267	452	200
S3	SG	334	452	200
S4	TG	334	452	200

Table 3.2: The dimension of simulated devices.

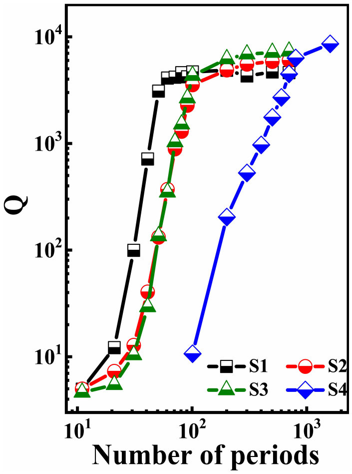

Figure 3.10: Simulated Q-factor for devices S1-S4 as defined in the text, for varying number of periods.

The interaction between the guided mode and the gratings was investigated by simulating the Q-factor and the confinement of the optical mode in the grating and the QWs, using a 3D-FDTD solver with PML and Bloch boundary conditions. All simulations were carried out for a wavelength of 1016 nm, the peak of the PL spectrum for the 60 nm nano-ridge. Figure 3.10 presents the calculated Q-factor for different structures, as function of the number of periods. S1, S2 and S3 are

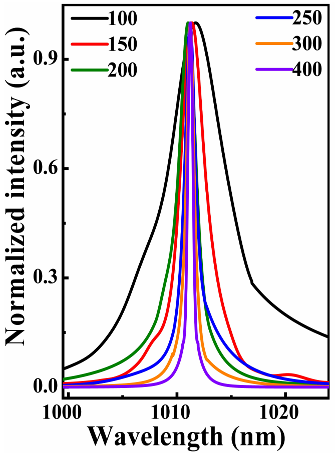

Figure 3.11: Simulated spectrum from nano-ridge with W_{aSi} = 200 nm, W_{NR} = 334 nm, H_{NR} = 452 nm, varying number of periods.

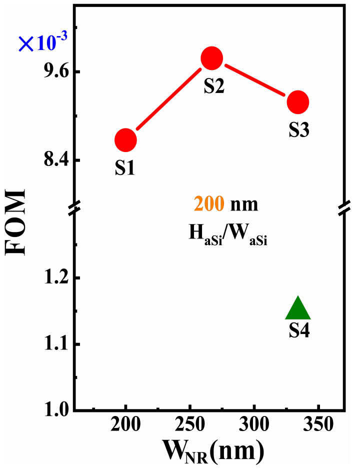

Figure 3.12: Relationship between FOM and W_{aSi} for the same devices S1-S4.

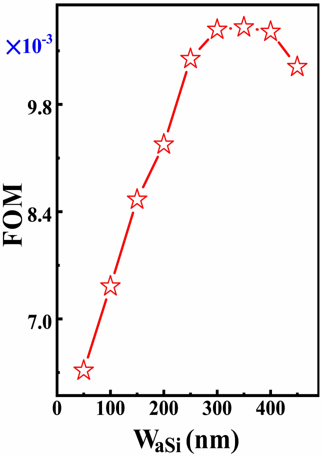

Figure 3.13: FOM as function of W_{aSi} for SGL with W_{NR} = 334 nm.

SGL devices for which the width of the nano-ridge was varied (W_{NR} is 200 nm, 267 nm and 334 nm for S1, S2 and S3 respectively). The height of the nano-ridge and the thickness of the grating are kept constant at H_{NR} = 452 nm and W_{aSi} = 200 nm. S4 is a TGL device with H_{NR} = 452 nm, W_{NR} = 334 nm and H_{aSi} = 200 nm. The latter is chosen to allow for a direct comparison with the SGL device. All dimensions of simulated devices are given in table 3.2.

It is obvious that for all devices the Q-factor increases with increasing number of periods. Further, for the SGL devices, the Q-factor increases faster for the narrower nano-ridges. This is a result of the increasing overlap of the optical mode with the grating. On the other hand, the Q-factor saturates at a slightly higher value for the wider devices and for the top grating. Finally, for the shorter gratings, the SGL devices always exhibit a higher Q-factor than the TGL devices.

Figure 3.11 shows the simulated spectrum for nano-ridge with W_{NR} = 334 nm, H_{NR} = 452 nm, W_{aSi} = 200 nm, Λ = 165 nm and different cavity lengths. As the number of periods increases, the linewidth narrows due to reduced light leakage, consistent with the Q-factor trend.

These simulations show that, in particular for the SGL devices, a narrower nano-ridge results in a stronger interaction of the mode with the grating and hence potentially shorter devices. However, reducing the nano-ridge width also results in a reduced confinement in the QWs, and hence a reduced modal gain. To further explore this trade-off, we used FOM = $\Gamma_{aSi}\Gamma_{QW}$, similar as in Section 2.4. Figure 3.12 shows this FOM for the 4 devices previously introduced. For all SGL devices the FOM is significantly larger than that for the TGL. In addition, the FOM for the SGL devices shows an optimum for $W_{NR} \sim 260$ nm. The dependence of the FOM on the nano-ridge width is limited however, and all experimental results were obtained for devices with W_{NR} = 334 nm as these were readily available. Figure 3.13 shows how the FOM varies for a SGL device, as a function of W_{aSi} (with W_{NR} = 334 nm). Increasing W_{aSi} increases the confinement in the grating and leads to an increased FOM. After reaching a maximum, the FOM decreases again as the mode shifts to the grating region and the overlap with the QWs decreases. Experimentally we found aSi grating teeth wider than 200 nm bended and touched each other after processing due to the high aspect ratio and the weak adhesion between the III-V material and the aSi grating, similarly as Section 2.5. Thus, in the remainder of this work, we mostly focus on devices with W_{aSi} = 200 nm.

3.5 Fabrication process

3.5.1 aSi deposition

The fabrication of the grating began with depositing a thick aSi layer on both sides of the nano-ridges. PECVD was used to evaluate the aSi coverage on the test sample (Figure 3.14). However, the deposition resulted in faster growth on the tops than the sides, causing the aSi on neighboring nano-ridges to merge before fully filling the gaps.

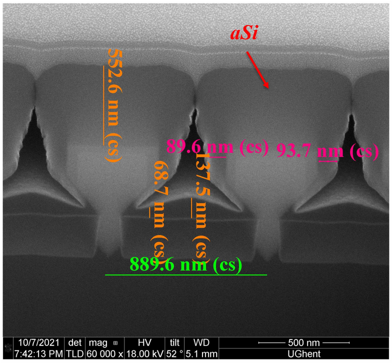

Figure 3.14: The test nano-ridge sample with the deposited aSi thin film by PECVD.

Due to these limitations, electron beam evaporation was explored (Figure 3.15). While this increased the aSi volume between nano-ridges, achieving complete coverage remained a challenge.

To improve coverage, we returned to PECVD and partially removed nano-

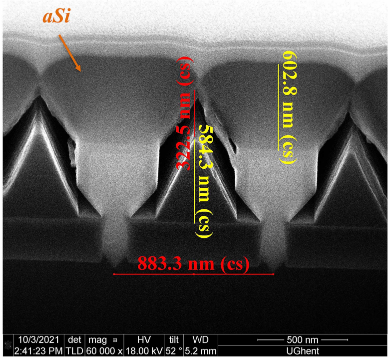

Figure 3.15: The test nano-ridge sample with the deposited aSi thin film by electron beam evaporation.

ridges in the array to create more open spaces. Using HSQ as a mask, we tested various etching recipes (table 3.3). Figure 3.16 and 3.17 show the etching rates of GaAs and HSQ, along with the GaAs/HSQ selectivity for each recipe. Transitioning from recipe 1 to recipe 2 increased both etching rate and selectivity due to higher ICP (Inductively Coupled Plasma) power, which enhances plasma concentration. Recipe 3 further improved selectivity by reducing RF power, minimizing physical bombardment. A similar trend was observed in recipe 4 with increased ICP power. Ultimately, recipe 3 was selected for its balance of high selectivity and moderate etching rates.

Figure 3.18 presents cross-sectional SEM images of the test sample at various stages: (a) EBL patterning and development, (b) nano-ridge etching, (c) HSQ removal, (d) aSi deposition, and (e) top aSi film etching. These results confirm that the filling and coverage challenges were resolved.

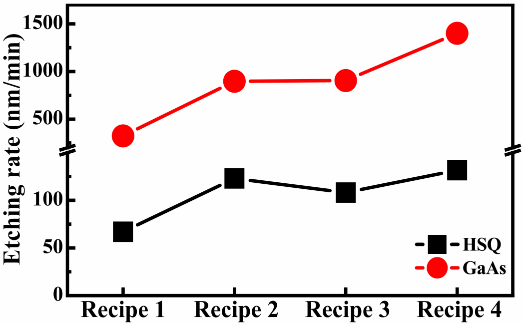

Figure 3.16: The etching rates of GaAs and HSQ from different etching recipes in table 3.3.

	Nano-ridge etching recipe 1	Nano-ridge etching recipe 2	Nano-ridge etching recipe 3	Nano-ridge etching recipe 4
Gases	BCl_3/N_2	BCl_3/N_2	BCl_3/N_2	BCl_3/N_2
Chamber pressure (mTorr)	3	3	3	5
Flow	20/8	20/8	20/8	20/8
ICP power (W/V)	200 W	400 W	400 W	600 W
RF power (W/V)	120 W	120 W	100 W	100 W
Temperature(°C)	18	18	18	18
Etching time	1 min	2 min	1 min	1 min

Table 3.3: Etching recipes for removing the nano-ridges.

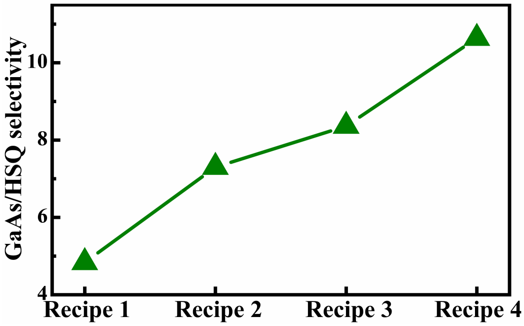

Figure 3.17: The selectivities of GaAs/HSQ from different etching recipes in table 3.3.

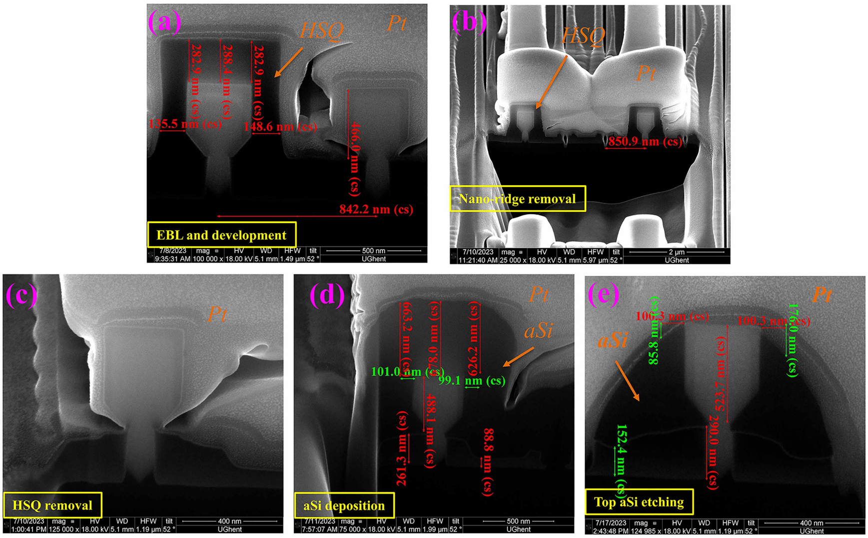

Figure 3.18: The cross sectional SEM images of the test sample with (a) EBL patterning and development, (b) nano-ridge etching, (c) HSQ removal, (d) aSi deposition and (e) top aSi film etching

3.5.2 SiO_x etching

In Chapter 2, a $\sim$ 50 nm cured BCB layer was used as a protective layer but proved unstable for etching. Here, it was replaced with a more robust SiO_x hard mask deposited via PECVD. The etching process was optimized to minimize effects on subsequent SG structure definition, using a test sample (400 nm HSQ - 200 nm SiO_x on Si substrate) patterned with HSQ resist. Etching was performed in RIE mode on an ICP-RIE (Inductively Coupled - Plasma Reactive Ion Etching) system, with recipes detailed in table 3.4. Cross-sectional SEM images (Figure 3.19) were used for evaluation. Although distinguishing HSQ from SiO_x in SEM images is challenging due to similar contrast, the layer adjacent to the Si substrate was confirmed as SiO_x.

Figure 3.19 illustrates that the volume of SiO_x near the silicon substrate increases with higher CHF_3 flow rates. When CHF_3 = 200 sccm is used as the etching gas, the etched profile near the substrate approaches a rectangular shape—indicating enhanced anisotropic etching. This improvement is attributed to surface passivation caused by etching by-products, which suppress lateral etching. While the SiO_x sidewalls were not entirely vertical, over-etching produced sufficiently vertical, thin layers for protection (Figure 3.20). Top, cross-sectional, and tilted SEM images (Figure 3.20) of a sample (40 nm SiO_x - 600 nm aSi - 300 nm SiO_x - Si substrate) confirm the results.

	SiO_x etching recipe 1	SiO_x etching recipe 2	SiO_x etching recipe 3
Gases	CHF_3/O_2	CHF_3/O_2	CHF_3/O_2
Flow	50/21	100/21	200/21
Chamber pressure (mTorr)	5	5	5
RF power (W/V)	150 W	150 W	150 W
Temperature(°C)	18	18	18
Etching time	25 mins	25 mins	25 mins

Table 3.4: Etching recipes for SiO_x.

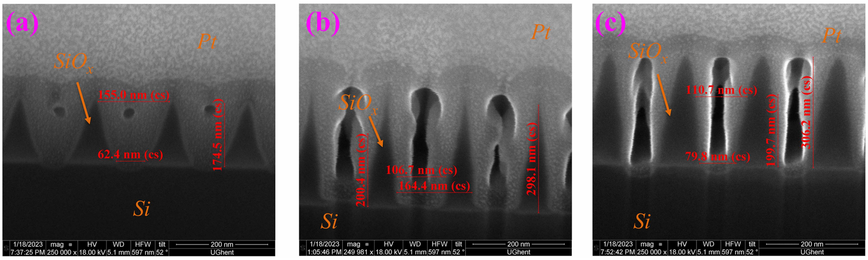

Figure 3.19: The cross sectional SEM images of the test sample (400 nm SiO_x - Si substrate) etched with SiO_x etching recipe 1 (a), recipe 2 (b) and recipe 3 (c).

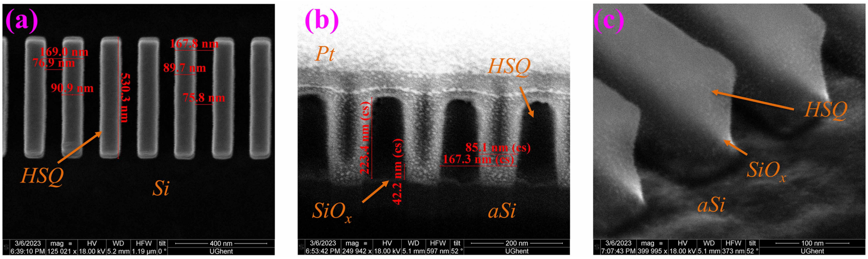

Figure 3.20: The top, cross sectional and tilted SEM images of another test sample (40 nm SiO_x - 600 nm aSi - 300 SiO_x - Si substrate) over-etched with SiO_x etching recipe 3.

	aSi etching recipe 1	aSi etching recipe 2	aSi etching recipe 3	aSi etching recipe 4
Gases	$CHF_3/SF_6/H_2$	$CHF_3/SF_6/H_2$	$CHF_3/SF_6/H_2$	$CHF_3/SF_6/H_2$
Flow	98/10/4	98/10/5	98/10/6	98/10/8
Chamber pressure (mTorr)	3	3	3	3
RF power (W/V)	150 W	150 W	150 W	150 W
Temperature(°C)	18	18	18	18
Etching time	1 min 45s	1 min 45s	1 min 45s	1 min 45s

Table 3.5: aSi etching recipes

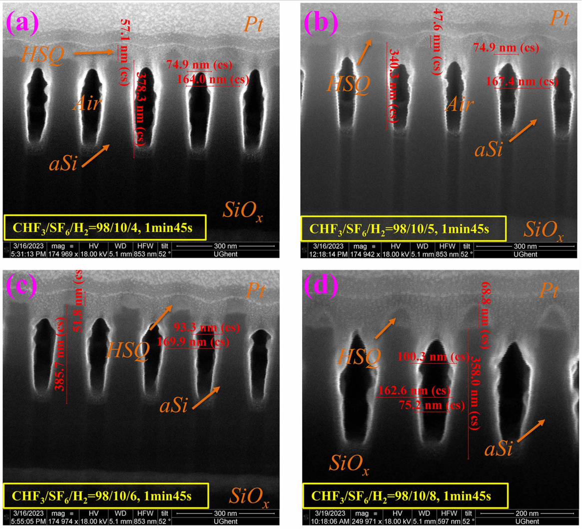

Figure 3.21: Cross sectional SEM images of the test samples (40 nm SiO_x - 600 nm aSi - 300 nm SiO_x - Si substrate) etched with different aSi etching recipe 1 (a), recipe 2 (b), recipe 3 (c) and recipe 4 (d).

3.5.3 aSi deep etching

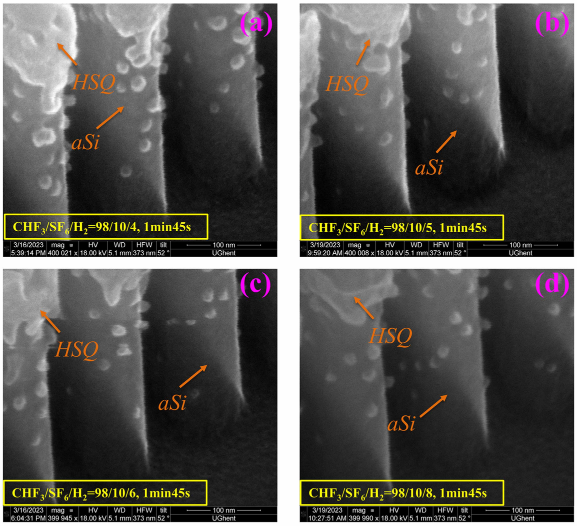

Figure 3.22: The tilted SEM images of the same test samples in Figure 3.21.

Section 2.5.4.1 highlighted the low selectivity of the aSi etching process with respect to HSQ, which was inadequate for defining the high aSi grating on both sides. To optimize the etching process, we used a test sample (40 nm SiO$_x$ - 650 nm aSi - 300 nm SiO$_x$ - Si substrate) patterned with HSQ resist. The etching recipes (table 3.5) were assessed using cross-sectional and tilted SEM images (Figure 3.21 and 3.22). Although all conditions resulted in sidewalls with good verticality, the top portion of the sidewalls consistently exhibited surface roughness, indicating potential limitations in resist integrity or etching uniformity near the surface.

Etching depths of 300–400 nm (Figure 3.21) were insufficient for grating

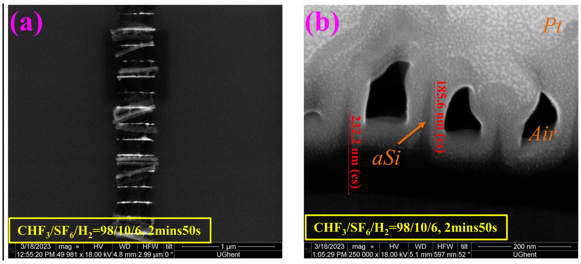

Figure 3.23: (a) Top and (b) cross sectional SEM images of the etched test samples with the increased etching time.

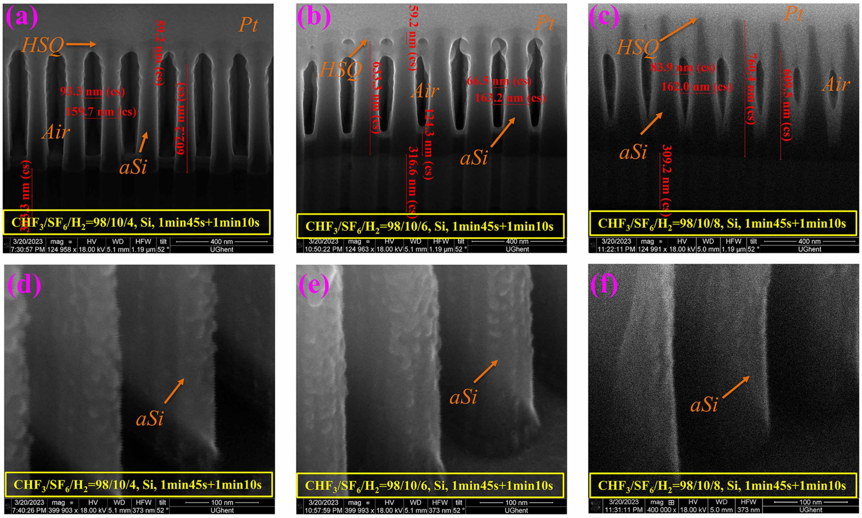

Figure 3.24: (a)-(c) Cross sectional and (d)-(f) tilted SEM images of the etched test samples with 2 etching steps and time interval of 10 mins.

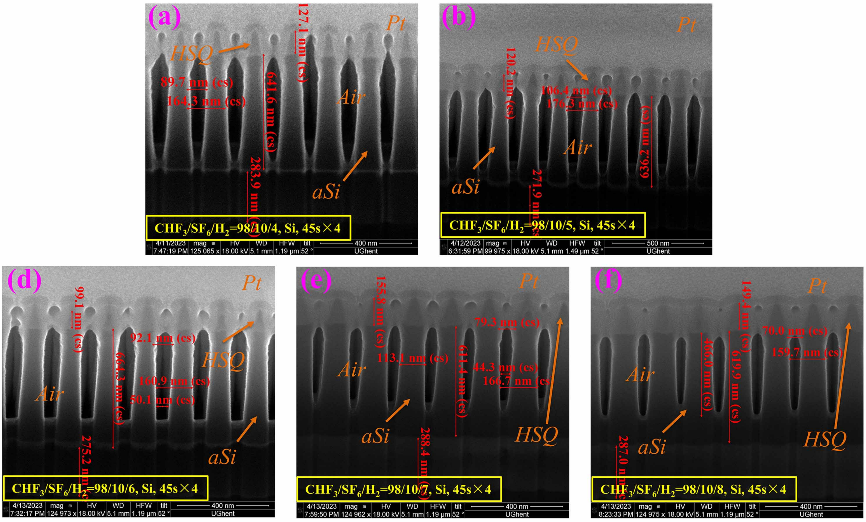

Figure 3.25: Cross sectional SEM images of the etched test samples with 4 etching steps and time interval of 10 mins.

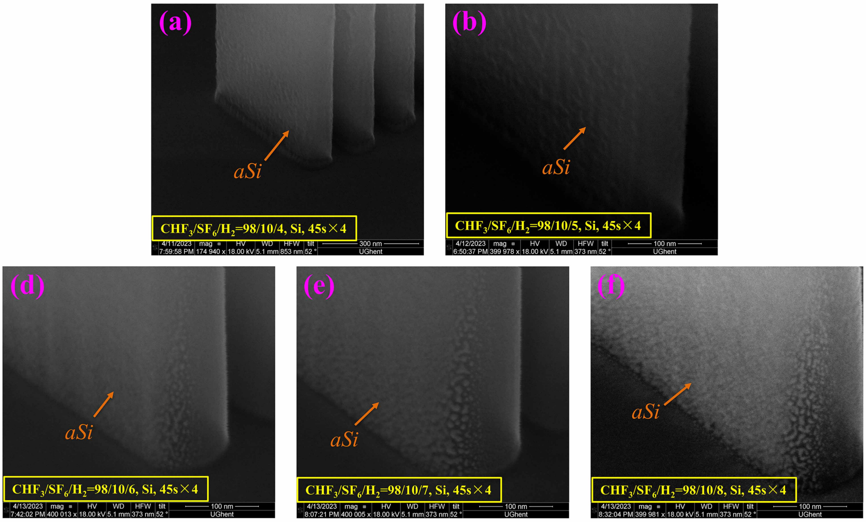

Figure 3.26: Tilted SEM images of the etched test samples with 4 etching steps and time interval of 10 mins.

definition. While extending the etching duration was considered, a total etching time of 2 minutes and 50 seconds led to significant distortion of the grating profiles however (Figure 3.23). The resulting structures in Figure 3.23(b) exhibited sharp triangular shapes, which likely caused by inadequate heat dissipation during continuous etching.

To mitigate thermal effects and improve etching quality, the process was divided into two steps with a 10-minute cooling interval. This adjustment produced clearer grating profiles, albeit with rough sidewalls, as observed in Figure 3.24. Further refinement was achieved by splitting the etching into four steps, each separated by a 10-minute cooling period. This multi-step approach yielded improved structural integrity and more uniform sidewall quality.

Figure 3.25 and 3.26 show the improved etching results. The sidewall roughness was caused by the SEM imaging but not the etching process. Initially, the sidewall appeared smooth under the electron beam imaging, but white spots emerged with increasing imaging time. Key optimizations included: 1) using a pure Si substrate carrier for enhanced heat dissipation, 2) allowing sufficient cooling intervals to prevent heat accumulation, and 3) cleaning the chamber with O_2 plasma after every four-step cycle to prevent by-product buildup, which could increase chamber pressure and weaken anisotropic etching.

The optimized SiO_x and aSi recipes were utilized for defining the SG. The

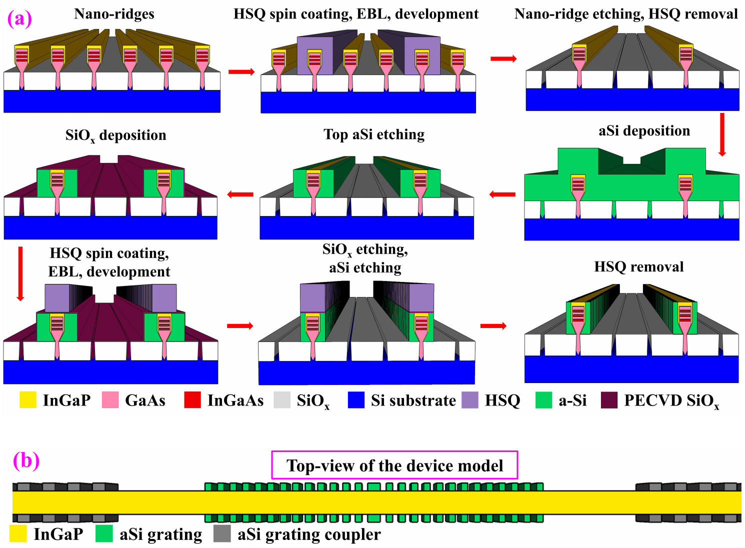

Figure 3.27: (a) Process flow diagram illustrating the fabrication steps of nano-ridge DFB laser with the SG. (b) Top-view schematic of the device.

full fabrication process and the top-view schematic of the device are illustrated in Figure 3.27(a) and 3.27(b) . First, part of the nano-ridges in the dense array were removed to reduce the overall filling ratio of the nano-ridge pattern and allow for complete aSi filling, using a combination of EBL and plasma etching. We used HSQ resist, developed in a 1:3 mixture of AZ400K and DI water. The non-protected nano-ridges were removed using ICP-RIE with BCl_3/N_2 and the remaining HSQ resist was removed by a buffered oxide etching solution (BOE). Then, a $\sim$ 600 nm aSi thin film was deposited using a PECVD process. Next, the aSi thin film was uniformly etched using a $CHF_3/SF_6/H_2$ gas mixture through ICP-RIE, leaving only the aSi on the sidewalls. To protect the aSi layer from the HSQ-developer used in the subsequent lithography step, $\sim$ 40 nm SiO_x was deposited using PECVD. Then a second EBL step was used to define the grating in HSQ. Finally, the aSi grating structures on both sides of the nano-ridge and a second-order grating coupler were transferred from the HSQ resist to the aSi layer by ICP-RIE etching of the SiO_x layer and the aSi layer with CHF_3/O_2 and $CHF_3/SF_6/H_2$, respectively. A second-order grating is added to allow vertical coupling of the light emission. Figure 3.28(a) and Figure 3.28(b) depict a top-view SEM image and a tilted SEM image of DFB lasers with H_{NR} = 452 nm and W_{NR} = 334 nm. Figure 3.28(c) shows an enlarged view of the aSi grating. The crack visible in the lower part of the grating is aligned with the transition from the angled section at the bottom to the vertical section at the side of the nano-ridge. The current deposition process for the aSi

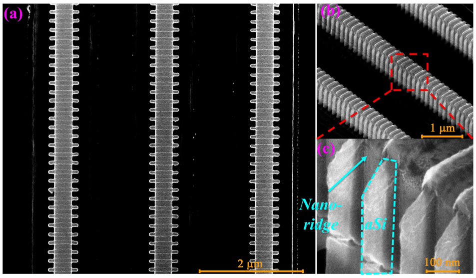

Figure 3.28: (a)Top-view SEM image of DFB lasers. (b) Tilted SEM image of the same DFB lasers. (c) Enlarged tilted SEM image of the aSi grating on the one side.

layer does not result in a perfectly conformal layer here. This could be improved in the future but at this moment does not seem to influence the operation of the device.

3.6 Optical characterization

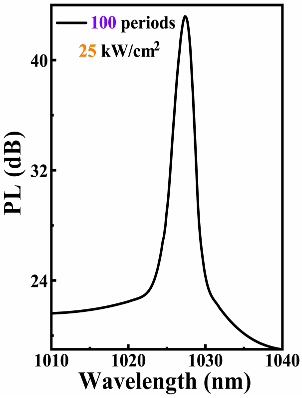

Figure 3.29: PL spectrum on logarithmic scale from the DFB laser with a 100-period SG under 25 kW/cm^2 532 nm-pulsed pump power density.

The devices were characterized using pulsed optical pumping, using the setup and settings discussed in Section 2.6. Figure 3.29 shows the PL spectrum for a SGL device with a grating having 100 periods, W_{aSi} = 200 nm and period Λ = 165 nm. The total length of the cavity was 16 µm. The pump power density was 25 kW/cm^2. The peak from the DFB laser is located at 1027 nm, achieving a SMSR of over 24 dB. The linewidth of this laser, obtained from a Gaussian function fitting as shown in Figure 3.30, is 1.25 nm and likely limited by the pulsed operating regime. Figure 3.31 shows the light in (pump power density) - light out (integrated PL) curve

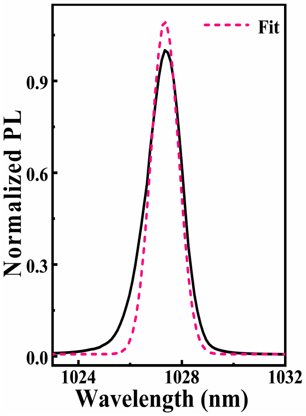

Figure 3.30: Normalized PL spectrum of the same DFB laser in Figure 3.29, fitted with a Gaussian function.

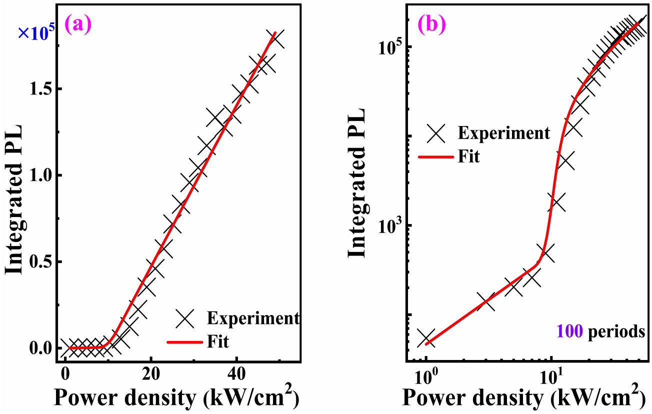

Figure 3.31: Light in - Light out curve on the linear (a) and logarithmic (b) scale of this DFB laser.

for the same device on a linear (a) and a logarithmic (b) scale. The characteristic S-shaped curve and a clear change of slope are the signature of lasing turn-on. The curve is fitted to a rate equations based model [118, 119] giving a value $\beta \sim 0.8$ % for the coupling efficiency from the spontaneous emission to the cavity mode.

To explore the effect of the grating length on the laser operation, the PL spectra and the light in – light out curves of a series of SGL devices with increasing number of periods was measured. Figure 3.32 shows the PL spectra taken at a pump power density of 25 kW/cm^2. All show a sharp peak, indicating laser operation. This is further confirmed by the light in – light out curves shown in Figure 3.33, which all

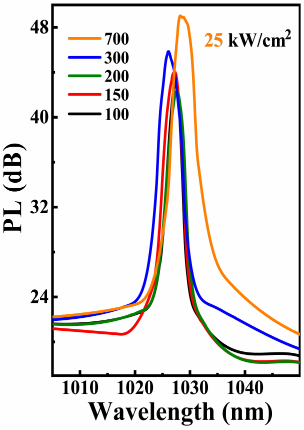

Figure 3.32: PL spectrum on dB scale from the DFB lasers with the SG comprising various numbers of periods at 25 kW/cm^2.

show a clear threshold behavior. The extracted threshold values are shown with black markers (design 1) in Figure 3.34. As expected, the threshold decreases with increasing grating length.

To investigate the effect of the grating strength, we measured the length dependent light in – light out curves for first 4 different device designs, as shown in table 3.6. The extracted laser thresholds for all 20 devices are shown in Figure 3.34. Comparing design 1 (black) and design 2 (red), we see that decreasing the thickness of the SG results in a higher threshold for shorter devices, associated with the lower confinement in the grating. For longer devices, the situation reverses, probably due to lower scattering losses in the shallow grating devices. This behavior is also expected from the simulations for the Q-factor shown in Figure 3.10, where we see a higher maximum Q-factor for devices with a weaker grating interaction. Design 3 and 4, with a TG, require a further increased cavity length to ensure low threshold lasing. Figure 3.35 shows the light in – light out curves for the 4 devices within the magenta ellipsis in Figure 3.34, which all exhibit a similar lasing threshold pump density. Here the effect of increasing the grating strength is even more obvious, with design 4 requiring 4 times the number of periods for reaching the same threshold density as design 1. Note that this effect would be even more pronounced if we referred to the absolute pump power. (i.e. the pump power density multiplied by the device surface).

To investigate the effect of the duty cycle, we measured the PL spectrum and length-dependent L-L curves for designs 1 and 5, as summarized in table 3.6. Figure 3.36 presents the PL spectrum for SGL devices with gratings of 200 periods and a 50 % duty cycle, and 400 periods and an 80 % duty cycle. The duty cycle is

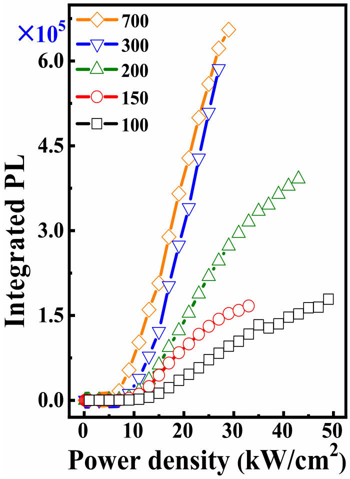

Figure 3.33: Light in - Light out curves on linear scale of the same DFB lasers in Figure 3.32

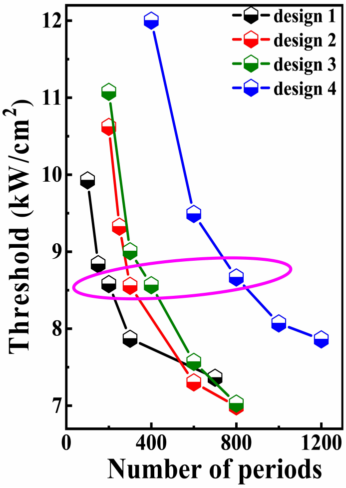

Figure 3.34: Extracted threshold values for devices with designs 1–4 as defined in table 3.6, for varying number of periods.

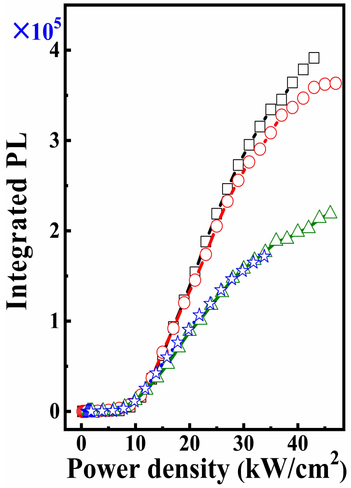

Figure 3.35: Light in–light out curves for the 4 devices within the magenta ellipsis in Figure 3.34.

	Grating type	W_{aSi}/H_{aSi} (nm)	Duty cycle (%)
design 1	SG	200	50
design 2	SG	50	50
design 3	TG	100	50
design 4	TG	50	50
design 5	SG	200	80

Table 3.6: The dimension of fabricated devices.

defined as the grating teeth width relative to the grating period. The SGL device with an 80 % duty cycle exhibited a shorter emission wavelength, likely due to the mask design error in the grating period. Theoretically, increasing the duty cycle contributes to a larger n_{eff} , leading to a longer lasing wavelength. However, the default 5 nm interval setting in IPKISS imposed a limitation, restricting the grating periods in this mask to 165, 170, 175 nm and so on. This issue was resolved for the series with a 50 % duty cycle.

Figure 3.37(a) displays the extracted laser thresholds for all 10 devices. Comparing design 1 (black) and design 5 (orange), we observe that increasing the SG duty cycle raises the threshold for shorter devices, likely due to higher loss from the high-order mode. Figure 3.37(b) illustrates the L-L curves for the two devices within the magenta ellipsis in Figure 3.37(a), showing similar lasing threshold pump densities. However, design 5 required twice the number of grating periods as design 1 to achieve the same threshold density, highlighting the significant impact

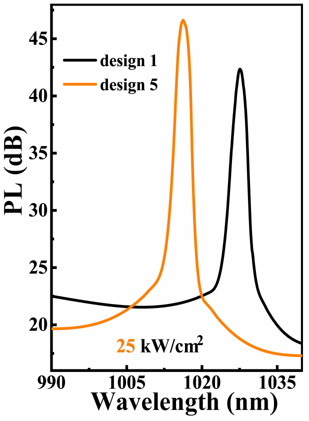

Figure 3.36: PL spectrum for for devices with design 1 and 5 as defined in table 3.6, with 200 periods, 50 % duty cycle and 400 periods, 80 % duty cycle, respectively.

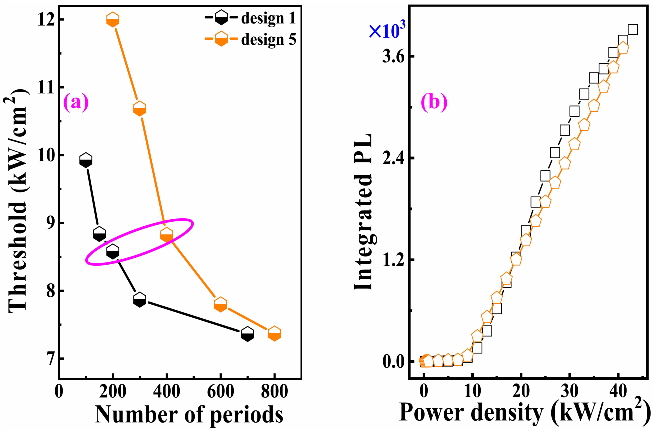

Figure 3.37: (a) Extracted threshold values for devices with design 1 and 5 as defined in table 3.6, for varying number of periods. (b) Light in – light out curves for the 2 devices within the magenta ellipsis in (a).

of increasing the duty cycle.

3.7 Conclusion

We proposed a novel approach for realizing compact laser cavities, monolithically integrated on a silicon substrate, using an amorphous silicon grating deposited at the sides of a nano-ridge. By modifying the nano-ridge width or the grating thickness, the interaction of the lasing mode with the grating can be controlled and a high Q-factor can be obtained, even for cavities shorter than 20 µm. Compared to approaches based on etched gratings or photonic crystals, the deposited grating does not deteriorate the material quality. Under pulsed optical pumping, a $\sim$ 9.9 kW/cm^2 lasing threshold was observed for a DFB laser with a cavity length of only $\sim$ 16 µm (100 periods). The spectrum reveals single mode operation with more than 24 dB side-mode suppression ratio. This result also again demonstrates the high-quality of the epitaxial material obtained using the nano-ridge approach. Recently, also lasing under electrical injection was demonstrated for nano-ridge based devices [125]. However, the weak feedback in these devices resulted in a cavity length of 1-2 mm. The high contrast gratings demonstrated in the current work, open up the road towards realizing much more compact electrically injected devices that can be used in high density optical interconnects and other high volume applications based on silicon photonics.

4

Photonic crystal nano-ridge laser

Chapters 2 and 3 examined GaAs nano-ridge devices, with Chapter 2 focusing on achieving low thresholds and Chapter 3 on achieving small footprints. Lasers meeting these targets simultaneously have been pursued due to their low energy consumption and high-density integration. Achieving high integration density and low power consumption necessitates device miniaturization and low-threshold lasing. This work employs a PC cavity to minimize footprint and power consumption, benefiting from its strong light-matter interaction at the wavelength scale and its apodized cavity design. The proposed device model is shown in Figure

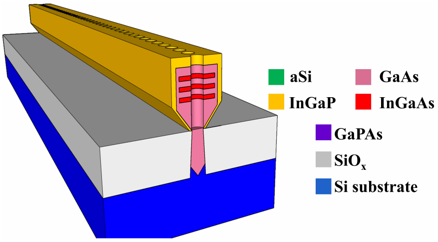

Figure 4.1: 3D model of PC cavity.

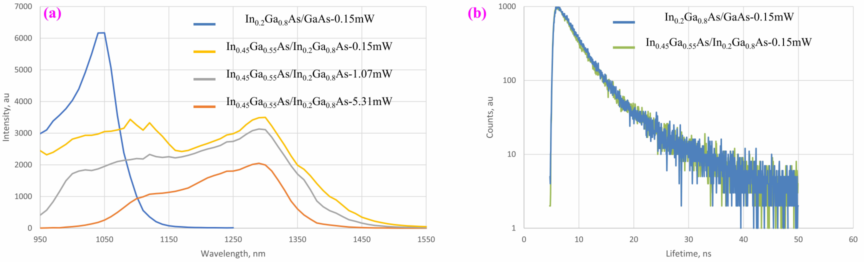

Figure 4.2: (a) PL spectra from GaAs-based and InGaAs-based nano-ridges under different pulsed pump power. (b) TRPL from the same nano-ridges at 0.15 mW.

4.1. Additionally, previous emissions were limited to around 1100 nm, whereas optical interconnect applications typically require emissions at 1.31 µm or 1.55 µm. As discussed earlier, we will use InGaAs nano-ridge devices with higher indium content to shift emissions to longer wavelengths [105].

In our previous work, InGaAs-based nano-ridges demonstrated emission at 1.31 µm. However, GaAs-based nano-ridges showed superior material quality, while InGaAs-based structures still require further optimization (see Figure 4.2). Details on the growth process can be found in [126]. From Figure 4.2, although the carrier lifetimes of GaAs- and InGaAs-based nano-ridges are comparable, the PL intensity is significantly higher for GaAs-based nano-ridges, indicating a greater proportion of radiative recombination. Thus, we began device design with GaAs-based nano-ridges emitting at ∼1.1 µm. Section 4.1 evaluates the optical performance using PL spectra and lists the nano-ridge dimensions. These measurements informed subsequent cavity designs using a 3D-FDTD solver. Section 4.2 analyzes cavity modes through FDE simulations, while Section 4.3 presents the cavity design principles, including band structure simulations and Q-factor calculations. Section 4.4 addresses fabrication challenges while section 4.5 discussed the extension of the wavelenght to 1.31 µm and the optical characterization. Conclusions are provided in Section 4.6.

4.1 Photoluminescence characterization

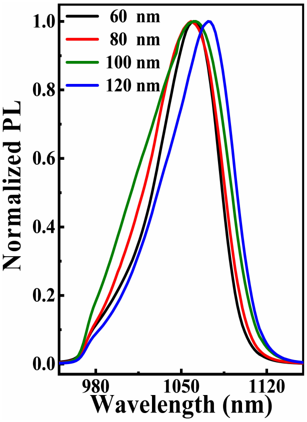

Figure 4.3: Normalized PL spectra from nano-ridges with trench widths 60 nm, 80 nm, 100 nm and 120 nm under 4.20 W/cm^2 CW 532 nm excitation.

Designed trench width (nm)	α (nm)	β (nm)	γ (nm)
60	376.3	501.3	87.5
80	435.4	515.5	95.8
100	505	545.7	116.7
120	510.4	557.8	135.4

Table 4.1: Nominal trench width, nano-ridge height, nano-ridge width and actual trench width.

The nano-ridge arrays are pumped at 4.20 W/cm^2 using a 532 nm CW diode laser, as described in Section 2.2. These arrays have different dimensions and emission wavelengths compared to those in previous chapters. Figure 4.3 shows normalized PL spectra for GaAs nano-ridges with three InGaAs QWs for different trench widths. The PL spectra exhibit a broad peak from 1000 nm to 1060 nm, with peak emissions attributed to active $In_{0.2}Ga_{0.8}As$ QWs. The cavity design, discussed in the following section, targets this wavelength range. Redshifts in PL peaks with increasing trench width are consistent with findings in Section 2.2. The nano-ridge dimensions measured with SEM are provided in Table 4.1, with parameters α, β, and γ defined in Section 2.1. These serve as inputs for the cavity design.

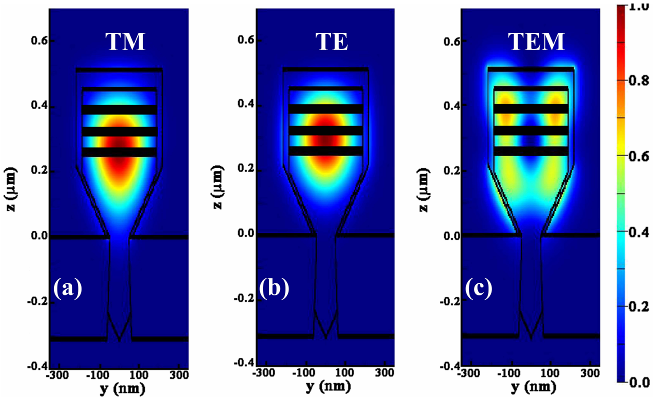

Figure 4.4: The first three optical modes of the nano-ridge with 80 nm trench width. The polarization of the modes is shown at the top of the images. The simulation was carried out with an FDE solver.

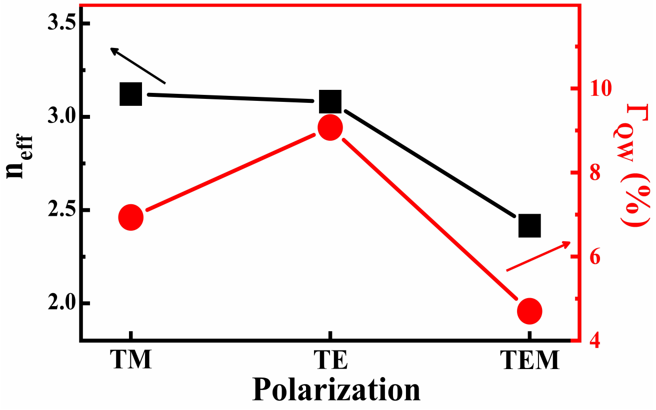

Figure 4.5: The simulated n_{eff} and Γ_{QW} of different optical modes in the nano-ridge with 80 nm trench width. The simulation was carried out with an FDE solver.

4.2 Transversal optical mode

The optical modes supported by the nano-ridges were simulated using the FDE solver described in Section 2.3. Figure 4.4 illustrates the first three optical modes — TM-like, TE-like, and high-order TEM modes — for a 60 nm trench width. The TE-like ground mode was identified as the most promising for lasing due to its highest Γ_{QW} (9.072 %) in Figure 4.5. Figure 4.6 visualizes the TE-like mode profile, while Figure 4.7 shows how Γ_{QW} and n_{eff} change with trench width.

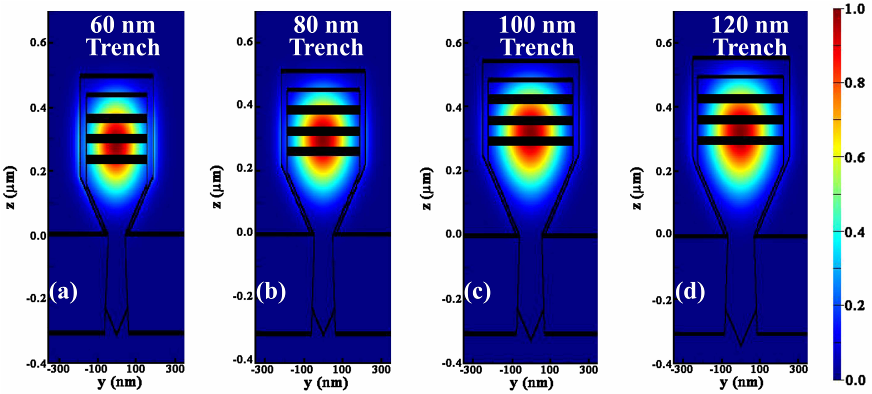

Figure 4.6: The TE-like ground modes of the nano-ridges with trench width 60 nm (a), 80 nm (b), 100 nm (c) and 120 nm (d). The simulation was carried out with an FDE solver.

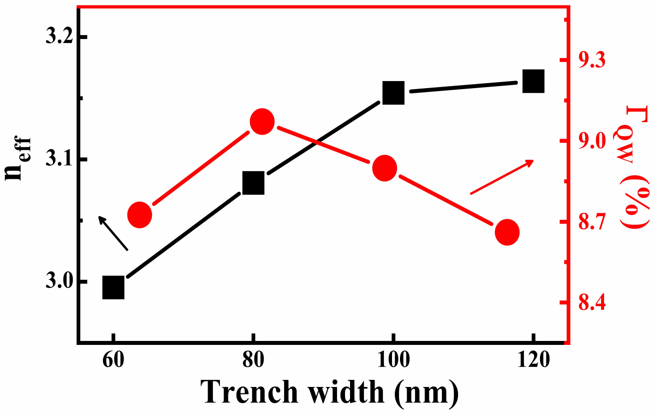

Figure 4.7: The simulated n_{eff} and Γ_{QW} of the TE modes in the nano-ridge with 60 nm, 80 nm, 100 nm and 120 nm trench width. The simulation was carried out with an FDE solver.

4.3 Apodized PC laser design

An apodized PC cavity design begins with band structure simulations for varying periods. The optical properties of PC cavities are analyzed to achieve a Gaussian electric field distribution through geometry optimization, aiming to maximize Q-factors while minimize the footprint. In this design, the cavity is divided into blocks with equal periodicity, progressively increasing from the center outward (see Figure 4.16). This shifts the bandgap position downward, as illustrated in the cavity band diagrams (see Figure 4.23(a)). The irregular shape of the nano-ridge complicates both band structure simulations and cavity design. Further details on addressing these challenges are provided in the sections below.

4.3.1 Band structure

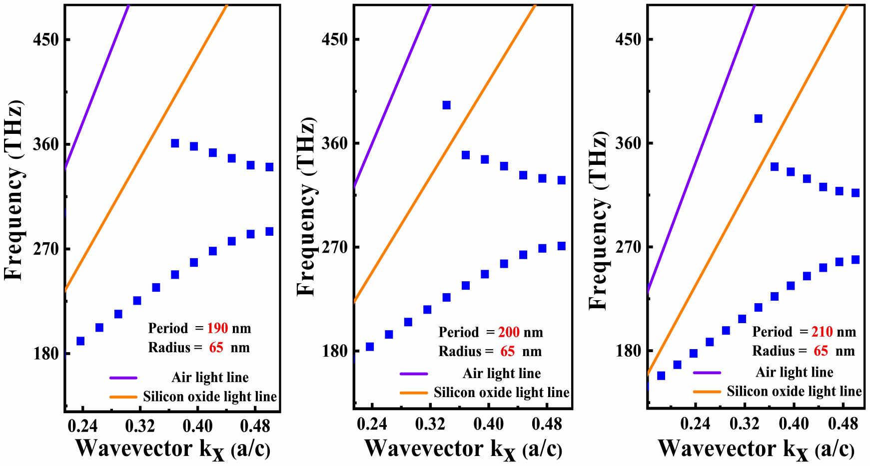

Figure 4.8: Photonic band structures for the PC inside the nano-ridge, with different periods and r = 65 nm.

Band structure analysis is essential for designing PC cavities. Band diagrams for structures with varying periods and a hole radius (r) of 65 nm were computed using a 3D FDTD solver with Bloch boundary conditions. The PC structure used in these simulations resembles Figure 4.16, but with an identical period (a_i). Figure 4.8 illustrates the formation of a photonic band gap at the Brillouin zone edge. Specifically, in Figure 4.8(c), the connections formed by the small blue squares in the upper region define the conduction band (or air band edge), while those in the lower region define the valence band (or dielectric band edge). The frequency range separating these bands is known as the band gap. The band gap increases with the period from 190 nm (Figure 4.8(a)) to 210 nm (Figure 4.8(c)), while the band-edge frequencies shift downward. In the simulation, the band frequencies were determined from the spectral peak positions across various wavevectors. Three key approaches were employed: (1) anti-symmetric boundary conditions along the light propagation direction and a TE-mode light source to select only TE-like cavity modes (2) exclusion of frequency points corresponding to peaks significantly smaller than the maximum peak (3) the use of a 3D-FDTD solver instead of conventional 2D or 2.5D solvers, to account for the nano-ridge's irregular shape.

4.3.2 Design principle

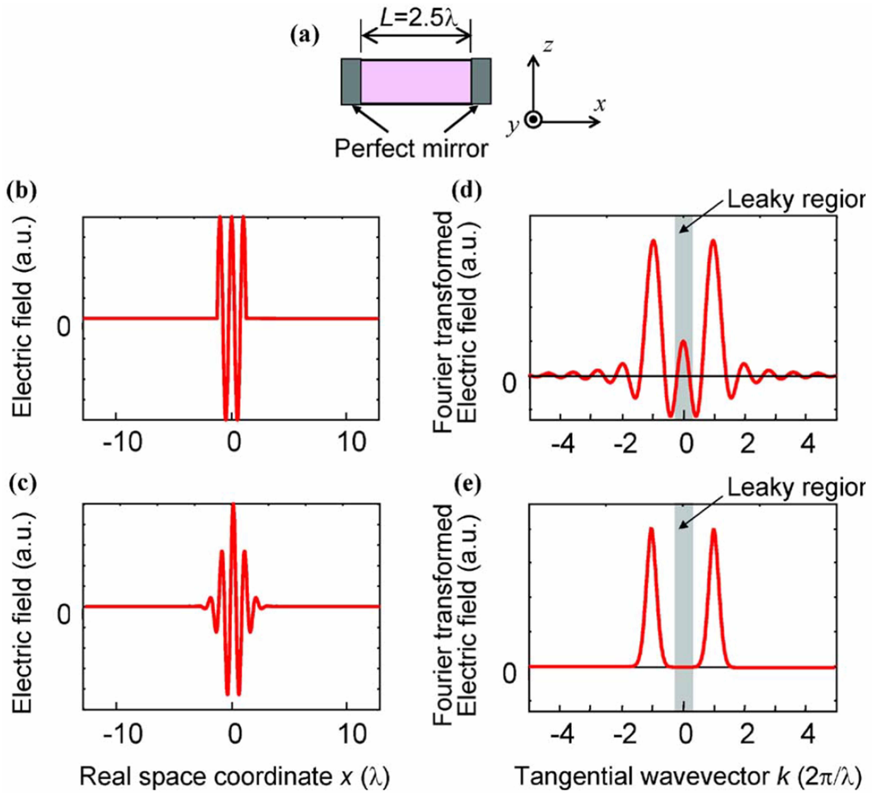

Figure 4.9: Analysis of cavities with different in-plane confinement characteristics. (a) Simplified model of a cavity. Electric field profiles of cavities with (b) a rectangular envelope function, and (c) a Gaussian envelope function. (d) and (e): respective Fourier transform spectra of (b) and (c). All are reproduced from Ref. [127].

The simplest PC cavity consists of two periodic hole arrays separated by a specific distance, functioning as mirrors for frequencies within the photonic band gap, similar to a FP resonator. Optical losses in these cavities stem from weak confinement in both the horizontal (x-direction) and vertical (z-direction) dimensions. While horizontal losses can be reduced by increasing the mirror length, vertical losses depend on the cavity's k-space distribution [128].

Vertical confinement strength, determined by total internal reflection, can be analyzed by decomposing the electric field within the cavity into plane wave components with varying wave vectors (k-vectors) via spatial Fourier transformation. When the tangential component $k_{//}$ (x-z plane) falls within the range $0 \leq k_{//} \leq 2\pi/\lambda_0$ (where λ_0 is the light wavelength in air), waves can escape into the air cladding, as the conservation law for $k_{//}$ (generalized Snell's law) is satisfied at the cavity-air interface. This results in weak vertical confinement. Since, when $k_{//}{>}2\pi/\lambda_0$, the conservation law is no longer held at the interface, enabling strong vertical confinement. Figure 4.9(d) depicts the spatial Fourier spectrum of the electric field—modeled as the product of a sinusoidal wave (λ) and an envelope function $F(x) = 1$ — as shown in Figure 4.9(b). Components within the leaky region $k_{//} \leq 2\pi/\lambda_0$ correspond to significant radiation loss.

Akahane et al. [129] proposed the "gentle confinement" design principle, employing gradual spatial variations in the envelope function at the cavity edges rather than abrupt changes to prevent components from entering the leaky region. Using a Gaussian envelope function $F(x)$ (see Figure 4.9(c)) significantly reduces components in the leaky region, as shown in the corresponding Fourier spectrum (see Figure 4.9(e)). This approach demonstrates that high-Q cavities can be achieved by carefully tailoring the envelope function and suppressing k-space components in the leaky region [127].

High Q-factors (up to 10^6 - 10^{10}) have been demonstrated in 1D PC cavities by varying the geometry (hole radius, periodicity, and width) [130–133]. These optimized structures produce a Gaussian field envelope by causing the field decay to vary quadratically with the distance from the cavity center. In this work, we optimized the lattice constants to produce a Gaussian field envelope. Using EBL to vary the lattice constants and define the relative positions of holes simplifies the fabrication process, as it avoids the high etching precision required for varying hole radii or widths. Following Ref. [127], we constructed a high-Q PC cavity with variable lattice constants. Figure 4.1 and 4.16 illustrate the simulation model.

For frequencies in the photonic band gap, no propagating modes exist. Wavevectors exhibit non-zero imaginary components q, causing fields to decay as e^{-qx}. To achieve a Gaussian field profile, q was varied linearly with distance x from the cavity center, producing an envelope decay of e^{-Bx^2} where $q = Bx$. Thus, our design approach leverages dependence of q on the lattice constant a. The value of q directly correlates with the frequency's position relative to the band edges, allowing tuning along the cavity by modifying the lattice constant. The design process involved:

(a). Calculating q as a function of frequency for various lattice constants.

(b). Analyzing the impact of lattice constant changes on the band structure.

(c). Determining the lattice constant variation required to achieve a Gaussian field profile.

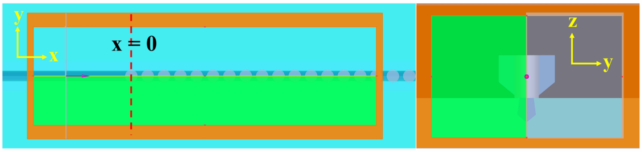

Figure 4.10: The top and cross-section view of the simulated model in a 3D-FDTD simulation.

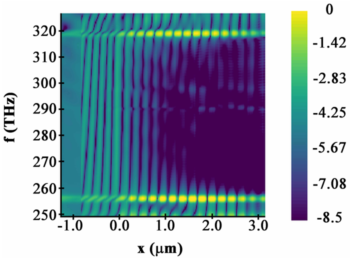

Figure 4.11: Electric field intensity distribution in a logarithmic scale along the linear monitor and in a frequency range across the photonic band gap, with a = 210 nm and r = 65 nm.

4.3.2.1 Decay factor $q(f)$ inside the photonic band gap

We calculated $q(f)$ for the nano-ridge photonic band gap using 3D-FDTD simulations, followed by data processing. Figure 4.10 gives the top view of the simulation model, where a broadband pulse enters the nano-ridge waveguide and encounters a PC mirror with a fixed period a. Inside the photonic band gap, the field penetrates the PC mirror evanescently, with a decay length inversely proportional to $\frac{1}{q(f)}$. A linear time monitor at the nano-ridge center captures the time-domain signal and a discrete Fourier transform is applied. Figure 4.11 shows the spatial electric field intensity distribution, highlighting the photonic band gap as a low-intensity region (dark blue zone).

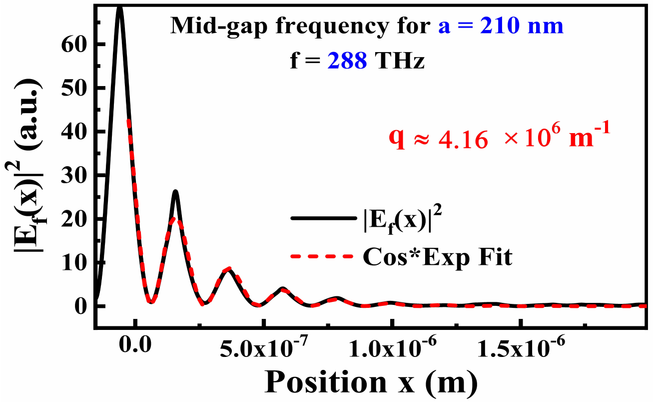

Figure 4.12: Calculated electric field intensity energy distribution for the mid-photonic band gap frequency along the simulated structure, with a = 210 nm and r = 65 nm.

The decay factor $q(f)$ was determined by fitting the electric field decay curve at each frequency within the photonic band gap. This fitting, shown as a red curve in Figure 4.12, used a product of a cosine function and an exponentially decaying function. Repeating this process for different periods a yielded the relationship between $q(f)$ and frequency, as plotted in Figure 4.13. Each $q(f)$ curve was fitted using Equation (4.2) to extract A_a, which was subsequently used for linear fitting in Figure 4.15.

Near the dielectric band-edge mode frequency, the dispersion relation $f(q_a)$ inside the gap is approximated by:

$$f = f_a^{cut} + A_a q_a^2 \tag{4.1}$$

Alternatively, q_a can be expressed as:

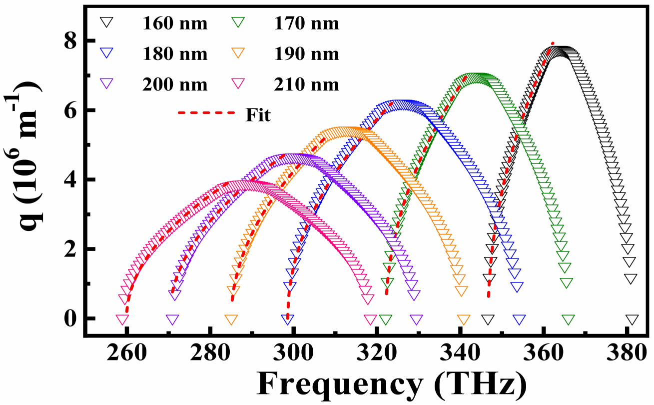

Figure 4.13: Calculated $q(f)$ in the photonic band gap with a = 210 nm and r = 65 nm.

$$q_a = \sqrt{\frac{f - f_a^{cut}}{A_a}} \tag{4.2}$$

Here, A_a is slightly dependent on the period a and where the cut-off frequency f_a^{cut} of the dielectric band-edge mode can be expressed

$$f_a^{cut} = \frac{K}{a} + \overline{f} \tag{4.3}$$

where $\overline{f}$ is a constant derived from period a_0 and and its associated cut-off frequency $f_{a_0}^{cut}$. Figure 4.14 plots the calculated cut-off frequencies for the two band-edge modes of the nano-ridge PC as a function of $\frac{1}{a}$. A linear fit gives K = 5.24×10^4 THz·nm and $\overline{f}$ = 11.38 THz.

Using equation (4.3), we can rewrite equation (4.2) in the following form:

$$q_a(f) = \sqrt{\frac{f - K(\frac{1}{a} - \frac{1}{a_0}) - f_{a_0}^{cut}}{A_a}} \tag{4.4}$$

We determined A_a by fitting the curves in Figure 4.15 to equation (4.2) near the dielectric band-edge mode frequency. $A_a(a)$ varies linearly with a as:

$$A_a(a) = A_a + \alpha(a - a_0) \tag{4.5}$$

where Figure 4.15 shows A_a values with a linear fit, giving A_0 = 0.96 Hz·m^2 and α = 0.027 GHz·m.

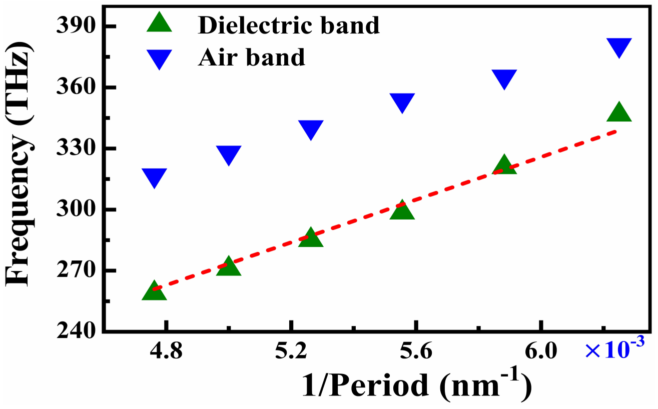

Figure 4.14: Cut-off frequencies of the band-edge modes of the nano-ridge PC as a function of $\frac{1}{a}$.

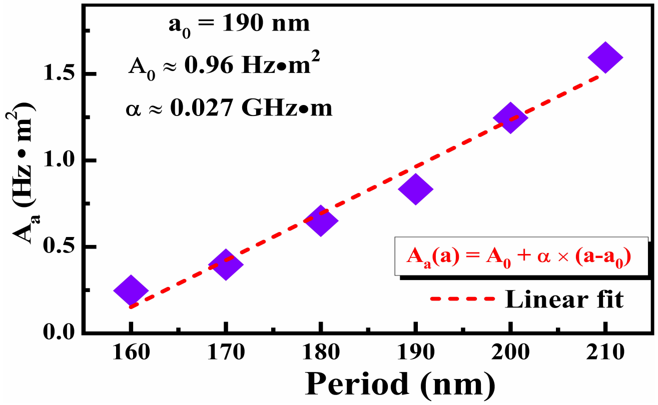

Figure 4.15: Parameter A_a as a function of the period a of the PC inside the nano-ridge.

In conclusion, we analyzed the relationship between the decay factor $q(f)$, frequency, and period a within the nano-ridge photonic band gap. Using these parameters, optimizing $a(x)$ enables us to achieve an apodized PC laser with a Gaussian field profile.

4.3.2.2 Continuous function $a(x)$

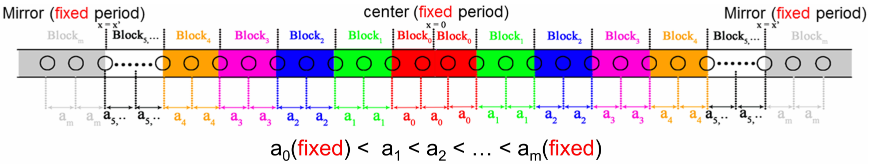

Figure 4.16: Top view of the apodized cavity.

Starting from $x = 0$, we vary the lattice constant $a = a(x)$, as depicted in Figure 4.16, to achieve a linear increase in q with x,

$$q(x) = Bx \tag{4.6}$$

where B is a constant with the unit of m^{-2}. The hole-to-hole distance at cavity center is fixed to a_0 and the cavity frequency f_{cav} is set to the cut-off frequency $f_{a_0}^{cut}$.

The apodized structure is divided into two regions, as depicted in Figure 4.16:

1. A region with a variable lattice constant $a(x)$, composed of 12 blocks with 24 holes starting from the center. The choice of 12 blocks balances the gentle period variation with the maximum stage movement resolution of our system.

2. A mirror block, consisting of 15 holes with a fixed lattice constant on each side.

Applying equation (4.4) at $f = f_{cav}$, the decay factor $q[a(x)]$ is expressed as:

$$q(f_{cav}, x) = \sqrt{\frac{K[\frac{1}{a_0} - \frac{1}{a(x)}]}{A_{a(x)}}} \tag{4.7}$$

Equalizing equation (4.6) and (4.7), the following equation is given:

$$\alpha B^2 x^2 a(x)^2 + (\widetilde{A_0} B^2 x^2 - \frac{K}{a_0}) a(x) + K = 0 \tag{4.8}$$

where $\widetilde{A_0} = A_0 - \alpha a_0$ for simplicity.

- If $\alpha = 0$, the solution of equation (4.8) simplifies to

$$a(x) = \frac{a_0}{1 - \frac{A_0 B^2 a_0}{K} x^2} \tag{4.9}$$

- If $\alpha \neq 0$, then equation (4.8) is a quadratic equation with the determinant:

$$\Delta(x) = (\widetilde{A_0} B^2 x^2 - \frac{K}{a_0})^2 - 4\alpha B^2 x^2 K \tag{4.10}$$

$$\Delta(x) = \widetilde{A_0}^2 B^4 x^4 - 2B^2 K(\frac{\widetilde{A_0}}{a_0} + 2\alpha)x^2 + \frac{K^2}{a_0^2} \tag{4.11}$$

Substituting $X = x^2$, we rewrite the determinant as:

$$\Delta(X) = \widetilde{A_0}^2 B^4 X^2 - 2B^2 K(\frac{\widetilde{A_0}}{a_0} + 2\alpha)X + \frac{K^2}{a_0^2} \tag{4.12}$$

with a new determinant δ_X:

$$\delta_X = 4B^4 K^2 (\frac{\widetilde{A_0}}{a_0} + 2\alpha)^2 - 4\widetilde{A_0}^2 B^4 \frac{K^2}{a_0^2} \tag{4.13}$$

$$\delta_X = 16 B^4 K^2 \alpha(\frac{\widetilde{A_0}}{a_0} + \alpha) > 0 \tag{4.14}$$

This confirms that equation (4.12) has two solutions, X_+ and X_-:

$$X_\pm = \frac{K}{\widetilde{A_0}^2 B^2}[(\frac{\widetilde{A_0}}{a_0} + 2\alpha) \pm 2\sqrt{\alpha(\frac{\widetilde{A_0}}{a_0} + \alpha)}] \tag{4.15}$$

Both solutions are positive, allowing us to express $\Delta(x)$ in terms of x:

$$\Delta(x) = (x - \sqrt{X_+})(x + \sqrt{X_+})(x - \sqrt{X_-})(x + \sqrt{X_-}) \tag{4.16}$$

The quadratic equation in $a(x)$ has solutions for $x \in [0, \sqrt{X_-}]$ and $x \in [\sqrt{X_+}, +\infty]$. Between $\sqrt{X_-}$ and $\sqrt{X_+}$, no solution exists for $a(x)$. Starting from $x = 0$, the values of $a(x)$ will be determined as a function of x values in the range $[0, \sqrt{X_-}]$.

Two solutions a_+ and a_- of equation (4.8), only a_- is physically meaningful, as $a_+ \to +\infty$ when $\alpha \to 0$:

$$a_- = \frac{-(\widetilde{A_0}B^2x^2 - \frac{K}{a_0}) - \sqrt{(\widetilde{A_0}B^2x^2 - \frac{K}{a_0})^2 - 4\alpha B^2x^2K}}{2\alpha B^2x^2} \tag{4.17}$$

Equation (4.17) is the most general solution in our approach.

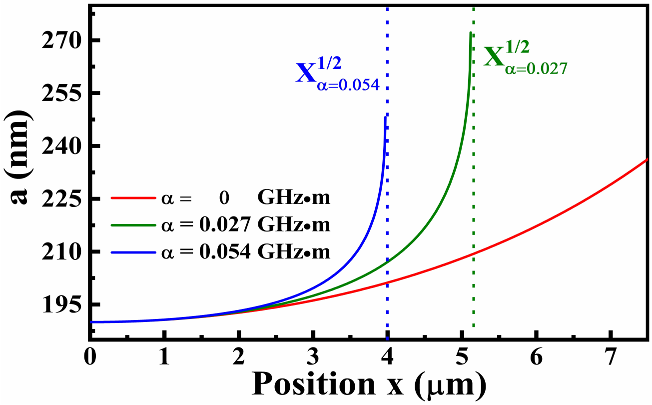

Figure 4.17: Hole-to-hole distance as a function of x for different α. x is defined as the distance from the center of hole to the center of the cavity.

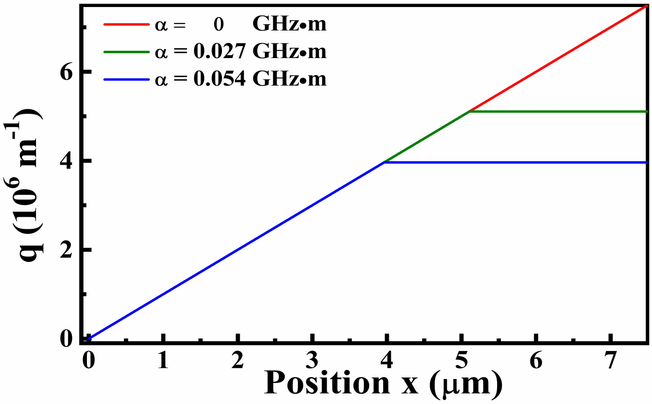

Figure 4.18: Decay factor q as a function of x for different α.

Figure 4.17, 4.18 and 4.19 show examples of the calculated "ideal" variations in lattice constant a, the decay factor q and the field envelope with position x for three values of α. The continuous variation requires a PC with a continuously

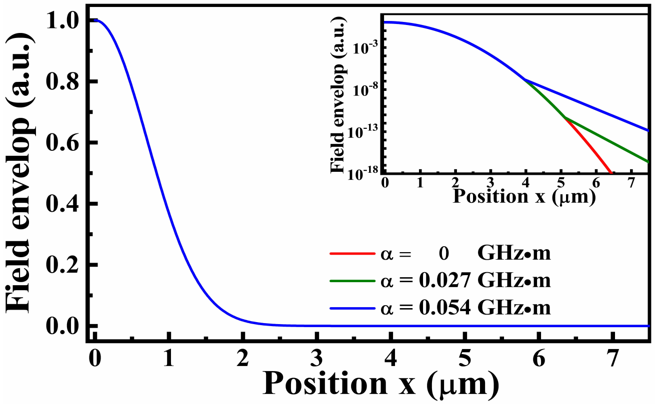

Figure 4.19: Ideal field envelope as a function of x for different α.

changing 'period' along x. However, such a variation is impractical for real-world fabrication.

As we expect, the period a increases more abruptly with x when α becomes larger. The parameter a becomes more constrained as α increases due to the diverge of $a(x)$ at $\sqrt{X_-}$. In practice, the lattice constant remains constant before $\sqrt{X_-}$. This has a noticeable effect on the variations of q: close to 0, q varies proportionally with x as expected but close to $\sqrt{X_-}$, the value of q is clamped to a constant value, which means that the decay of the field transitions from a Gaussian profile to a purely exponential one for $x > \sqrt{X_-}$. These "ideal" field envelopes are plotted in the inset of Figure 4.19 where the red and the green curves become straight lines for $x > \sqrt{X_-}$.

However, even with a large value for α = 0.054 GHz·m, the field envelopes are nearly identical. Hence, in the following, we will simply neglect the effect of α and use equation (4.9) for $a(x)$.

Until this point, we have considered continuous variations of a and q, even though $a(x)$ varies stepwise in a real structure. The variation of q induced by this discretization can significantly differ from the one obtained in a continuously varying model. The challenge in constructing apodized PC cavities is to ensure the value of q closely approximates the "ideal" case.

We will now describe and explain the hole positioning method chosen in this work.

4.3.2.3 Construction method

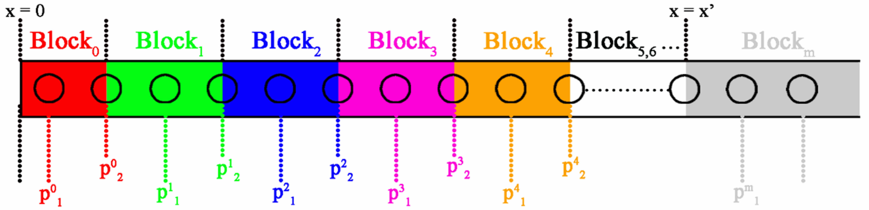

Figure 4.20: The detailed definition of p_k^i

Following the designs proposed by Noda's group [127], the cavity center at x = 0 is positioned between two holes (see Figure 4.16), where the maximum field intensity is also located. Similarly one could design a cavity with a hole in the centre, offering comparable characteristics. However, our design follows the former approach. For simplicity, our discussion focuses on the region $x > 0$, leveraging the symmetry of the structure.

Each region with a given periodicity is termed a "block." Block$_0$, with a lattice constant a_0, spans three periods, with the first two hole positions given by:

$$p_1^0 = \frac{1}{2}a_0$$

$$p_2^0 = \frac{3}{2}a_0$$

Subsequent blocks are two periods long, except for the mirror block. A single-period block could theoretically reduce discretization and enhance the Q-factor, but such a design demands exceptionally precise EBL control — down to a few angstroms — exceeding the capabilities of our EBL system. A two-period block design is a practical compromise, achieving a sufficiently high Q-factor.

In a two-period block, the "1^{st} hole" refers to the central hole of that block. The positions of the two holes (indexed by k) in the i^{th} block are expressed as:

$$p_k^i = \frac{3}{2}a_0 + 2\sum_{j=1}^{i-1} a_j + k * a_i \tag{4.18}$$

or equivalently:

$$p_k^i = \widetilde{C}_i + k * a_i \tag{4.19}$$

where $a_i = a(p_1^i)$ and $\widetilde{C}_i = (\sum_{j=0}^{i-1} 2a_j) - \frac{1}{2}a_0$. Figure 4.20 provides a detailed definition of p_k^i for the region x >0.

Hole positioning strategy

The hole positioning strategy, illustrated in Figure 4.21, aims to achieve blocks with decay factors q_i, taken in the middle of the block. This is not straightforward anymore as it implies finding simultaneously the middle position of the block, which is conveniently placed here at the position p_1^i of the first hole, with its associated lattice constant a_i. Mathematically, this necessitates solving equation (4.9) at $x = p_1^i$, expressed as:

$$a(p_1^i) = \frac{a_0}{1 - \frac{\widetilde{A}_0 B^2 a_0}{K}(p_1^i)^2} \tag{4.20}$$

Solving equation (4.20) involves resolving a cubic equation in a_i. To simplify, we assume that $\frac{\widetilde{A}_0 B^2 a_0}{K}(p_1^i)^2 \ll 1$ then

$$a_i = a_0[1 + \frac{\widetilde{A}_0 B^2 a_0}{K}(\widetilde{C}_i + a_i)^2] \tag{4.21}$$

$$a_i = a_0[1 + \frac{\widetilde{A}_0 B^2 a_0}{K}(\widetilde{C}_i^2 + 2\widetilde{C}_i a_i + a_i^2)] \tag{4.22}$$

which can be rewritten as the following quadratic equation:

$$a_i^2 + a_i(2\widetilde{C}_i - \frac{K}{\widetilde{A}_0 B^2 a_0^2}) + (\widetilde{C}_i^2 + \frac{K}{\widetilde{A}_0 B^2 a_0}) = 0 \tag{4.23}$$

The solutions to this quadratic equation are:

$$a_i^{\pm} = \frac{-(2\widetilde{C}_i - \frac{K}{\widetilde{A}_0 B^2 a_0^2}) \pm \sqrt{(2\widetilde{C}_i - \frac{K}{\widetilde{A}_0 B^2 a_0^2})^2 - 4(\widetilde{C}_i^2 + \frac{K}{\widetilde{A}_0 B^2 a_0})}}{2} \tag{4.24}$$

$$a_i^{\pm} = \frac{-(2\widetilde{C}_i - F) \pm \sqrt{-4\widetilde{C}_i F + F(F - 4a_0)}}{2} \tag{4.25}$$

where $F = \frac{K}{\widetilde{A}_0 B^2 a_0^2}$. The acceptable solution for our model is a_i^- since a_i^+ is significantly larger than a_0, even for block$_0$.

Figure 4.22 compares the hole-to-hole distances and field profile envelopes for continuous and discrete variations of $a(x)$. The approximation used to simplify equation (4.9) to (4.22) slightly reduces the variation in a, yielding a nearly identical ideal field envelope. Using equation (4.25), we iteratively computed and plotted the discrete lattice constant a_i case. For these values, the field envelope was determined by setting $q = q(a_i = constant(i))$ for each block (Figure 4.22(b)). This analysis shows that the discretized envelope exhibits a slightly greater spatial extension than the continuous case, due to the initial "decayless" propagation in Block$_0$, which shifts the onset of envelope attenuation.

The next section discusses the results of 3D FDTD simulations of cavities with Gaussian field envelopes.

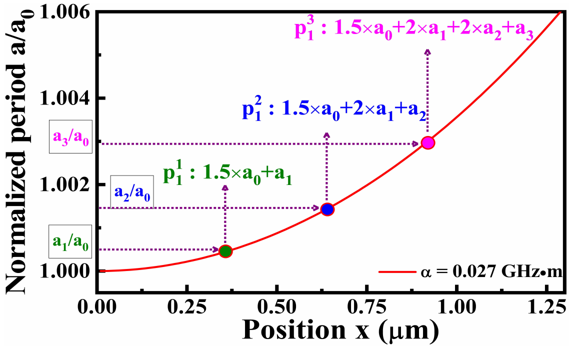

Figure 4.21: Hole positioning strategy: the value of the decay factor in the middle of each block is fixed. a_1^i and p_1^i are given by solving equation (4.20).

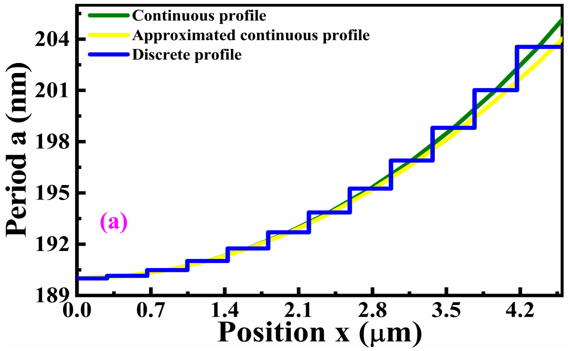

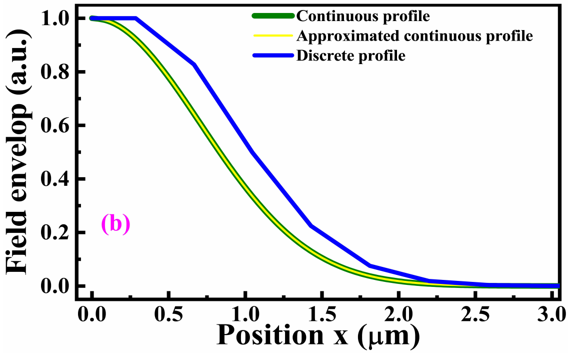

Figure 4.22: (a) Period a and (b) their corresponding field envelope profiles as a function of the position x from the cavity center for the three considered cases.

4.3.3 Cavity simulation

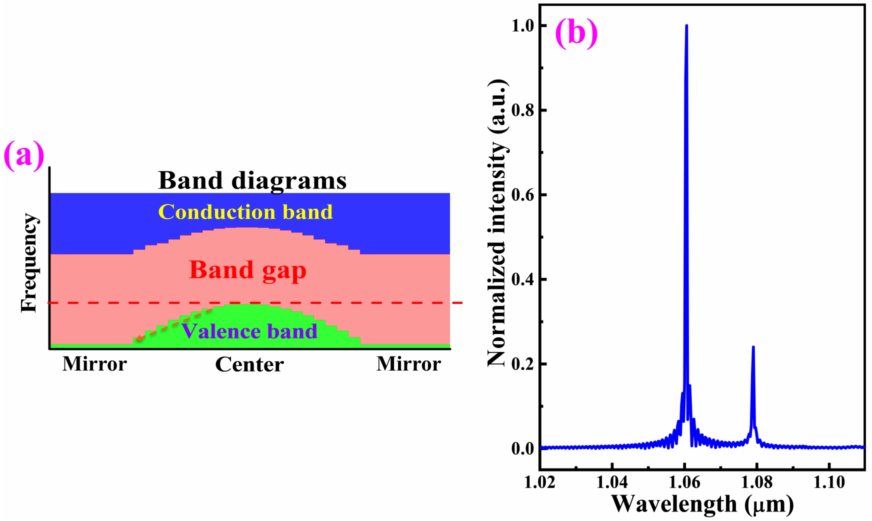

Figure 4.23: (a) Band diagram of the cavity. (b)Simulated spectrum from a PC nano-ridge laser.

The nano-ridge used in this design has dimensions of 546 nm and 505 nm in height and width. The periods in the cavity center, mirror block and the hole radius are a_0 = 189 nm and a_m = 198 nm, r = 65 nm. Figure 4.23(a) presents the cavity band diagram, illustrating the increasing period shifts the band gap downward. Figure 4.23(b) shows the simulated cavity spectrum. It shows two peaks at wavelengths λ = 1060 nm and λ = 1080 nm, corresponding to the first symmetric

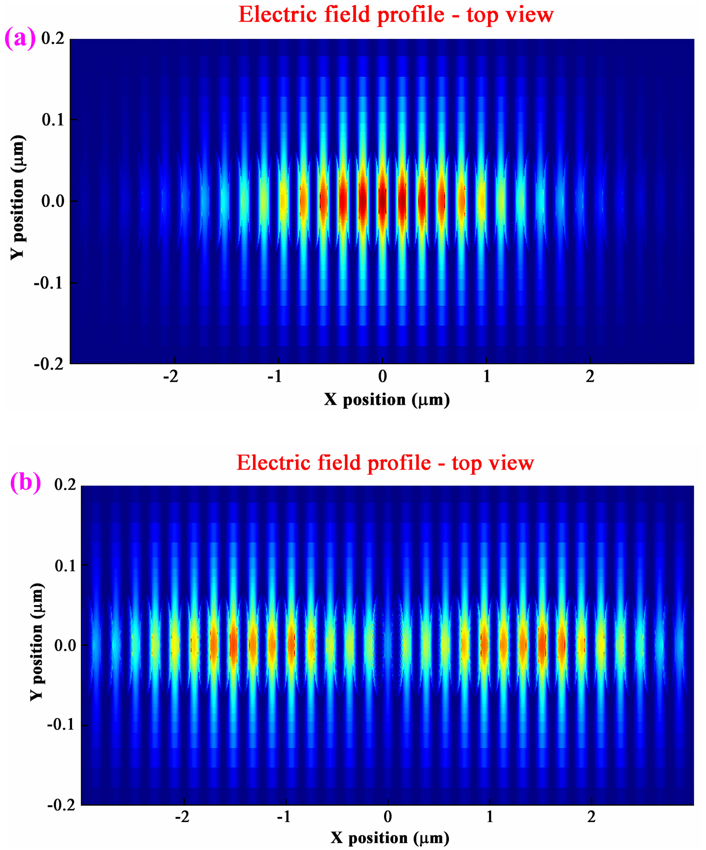

Figure 4.24: Gaussian electric field distribution of (a) the first symmetric mode and (b) the first anti-symmetric mode in the designed PC nano-ridge cavity.

mode and the first anti-symmetric mode. The simulation was performed using a 3D FDTD solver, with PML (perfectly matched layer) boundary conditions applied along the x and z axes and an anti-symmetry boundary condition along the y-axis. The definitions of the x, y, and z axes are provided in Figure 4.10.

Figure 4.24 shows that the electric field distribution for these modes is localized in the high-index material between the holes, which is expected as the cavity wavelength corresponds to the dielectric band-edge modes. The first symmetric mode achieves a Q-factor of approximately 2.7×10^5 at the resonance wavelength of λ = 1060 nm, which is two orders of magnitude larger than that of the cavities with aSi gratings. The first anti-symmetric mode has a higher resonance wavelength λ = 1080 nm but significantly smaller Q-factor of around 7.28×10^3.

The anti-symmetric mode originates from the band-edge states of lateral

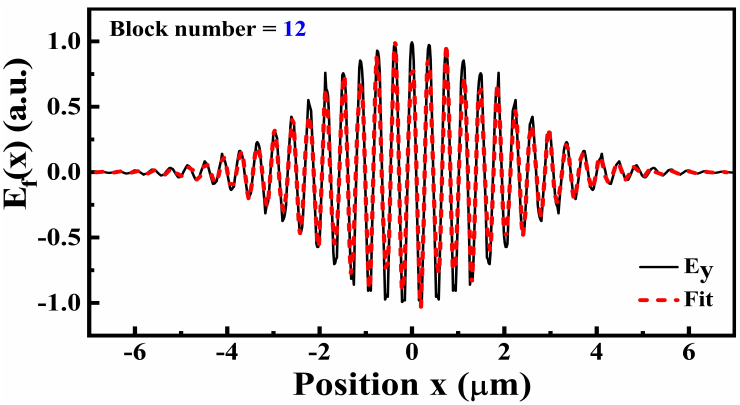

Figure 4.25: E_y field profile of the symmetric cavity mode along the cavity axis, fitted with the product of a Cosine and a Gaussian function.

blocks, which are segments of the cavity defined by their periodic structure and distinct band gap properties. In contrast to the symmetric mode, which is highly localized and represents the primary dielectric band-edge mode of the entire cavity, the anti-symmetric mode is associated with localized states within individual lateral blocks. These states are less confined to the cavity center and extend laterally across the periodic blocks. Subsequently, the anti-symmetric mode demonstrates a different propagation dynamics, oscillating between the blocks in a manner similar to that of a FP cavity. Due to its less localized nature, the anti-symmetric mode exhibits a lower Q-factor. Higher Q-factors for this anti-symmetric mode can be obtained by extending the apodized region with additional blocks. However, for most practical applications, single mode operation is preferred. As such, the fabricated laser has the potential to meet this requirement due to the higher loss associated with the anti-symmetric mode.

Figure 4.25 shows the E_y field profile of the first symmetric cavity mode along the cavity axis. The electric field profile follows almost perfectly a Gaussian envelope, as indicated by the fitting with the product of a Cosine and a Gaussian function.

To further analyze the effect of the mirror block period on the cavity performance, we calculated the Q-factor as a function of the mirror block period. Figure 4.26 plots the simulated Q-factor with the central period fixed at a_0 = 189 nm, while the mirror block period a_m varies from 194 nm to 212 nm in 2-nm increments. The Q-factor peaks at a_m = 198 nm due to a downward shift in the bandgap with increasing value of the period. This means that the reflection of the central block's dielectric-band edge mode first increases and then decreases. Figure 4.27 presents

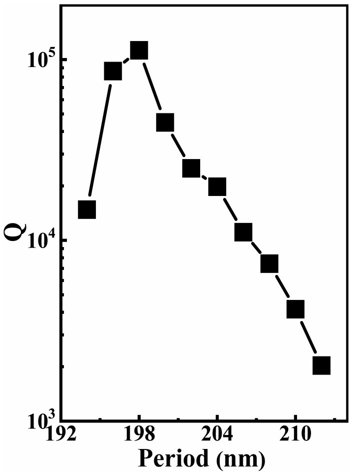

Figure 4.26: Q-factor vs. the period in the mirror block.

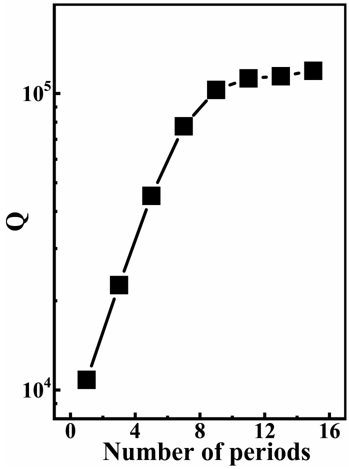

Figure 4.27: Q-factor vs. the number of periods in the mirror block.

the relationship between the simulated Q-factor and the number of holes in the mirror block, with a_0 = 189 nm and a_m = 198 nm fixed. The Q-factor increases and stabilizes for 7 periods in the mirror block, attributed to the less transmission loss with more periods.

4.4 Fabrication process

The fabrication process resembles the workflow outlined in Figure 4.47, with the etching extending through the entire nano-ridge. Patterning holes precisely at the center of the nano-ridge demands extremely accurate alignment during EBL. This issue is addressed by introducing intentional positional deviations in the mask design to compensate the potential misalignment. The proximity effect during exposure causes deviations in structure shapes, which are corrected using a commercial Beamfox software to apply the proximity effect corrections to the mask. Challenges arise from the small feature size of the hole radius and the high aspect ratio of etching (hole diameter to etching depth). These factors complicate PC definition within the nano-ridge due to the sensitivity of the etching gases to the local environment. Further details of the etching process exploration are provided below.

4.4.1 SiN$_x$ etching

	Recipe 1	Recipe 2	Recipe 3
Gases	CHF_3/O_2	CHF_3/O_2	CHF_3/O_2
Flow	52/3	50/5	48/7
Chamber pressure (mTorr)	55	55	55
RF power (W/V)	340 V	340 V	340 V
Temperature(°C)	18	18	18

Table 4.2: Etching series I for defining PC inside the SiN$_x$ hard mask.

	Recipe 4	Recipe 5	Recipe 6
Gases	CHF_3/O_2	CHF_3/O_2	CHF_3/O_2
Flow	52/3	52/3	52/3
Chamber pressure (mTorr)	14	28	75
RF power (W/V)	340 V	340 V	340 V
Temperature(°C)	18	18	18

Table 4.3: Etching series II for defining PC inside the SiN$_x$ hard mask.

Given the low etch selectivity between electron beam resist and GaAs, a SiN$_x$ layer deposited by PECVD is used as a hard mask for PC patterning. The non-

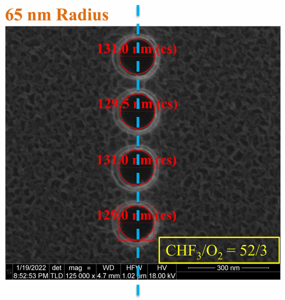

Figure 4.28: Top image of the test sample (130 nm SiN_x - Si substrate) etched with a CHF_3/O_2 ratio of 52/3.

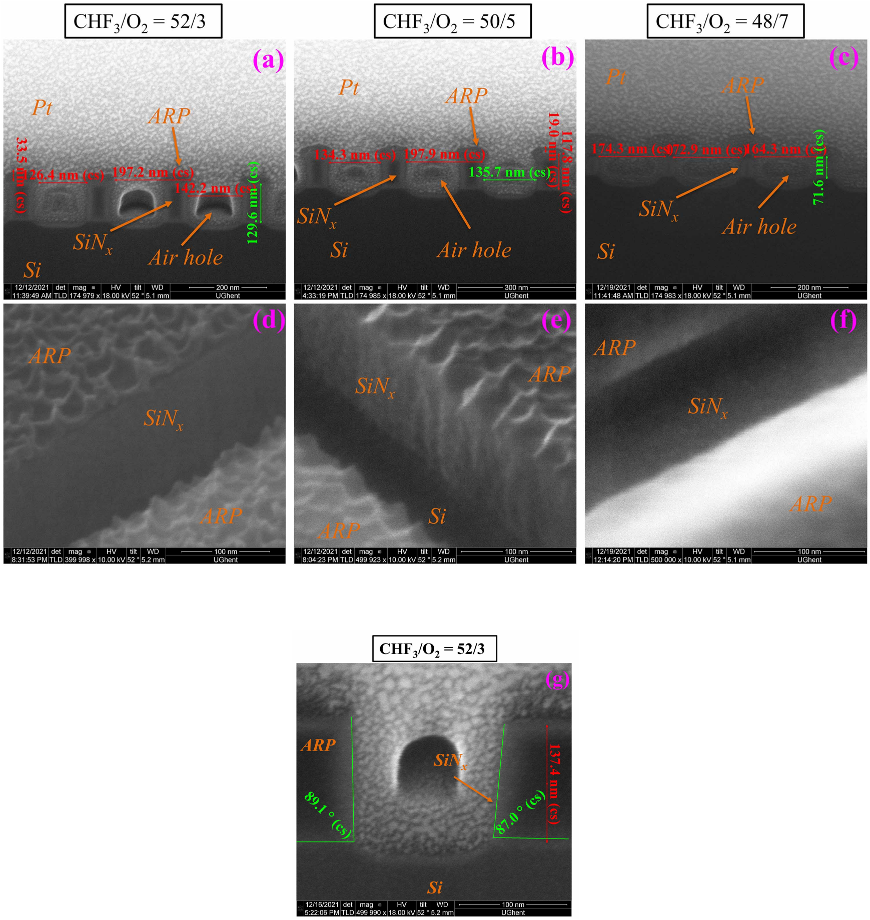

Figure 4.29: (a)-(c) Cross sectional SEM images of the PC, (d)-(f) tilted and (g) cross sectional SEM images of a 100 nm-wide trench, etched with different gas flows.

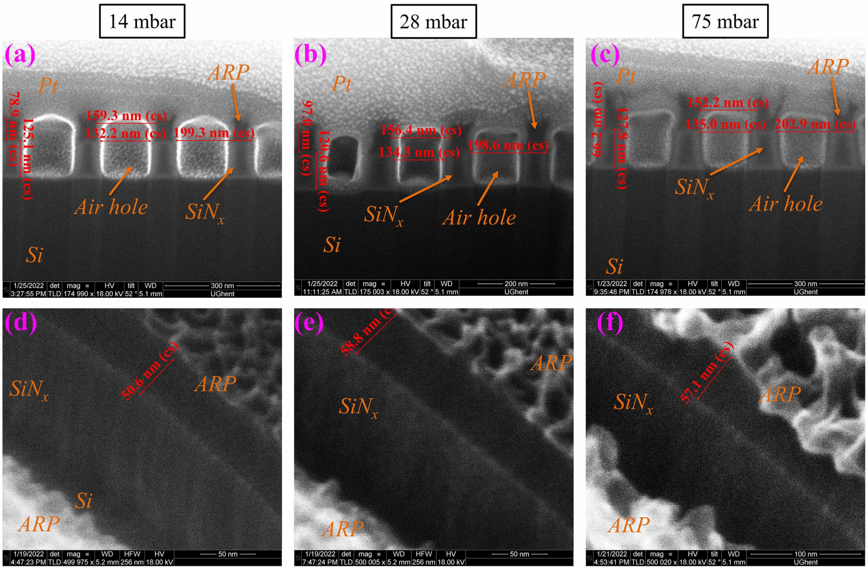

Figure 4.30: (a)-(c) Cross sectional SEM images of the PC, (d)-(f) tilted SEM images of a 100 nm-wide trench, etched with different chamber pressures.

	Recipe 7	Recipe 8	Recipe 9
Gases	CHF_3/O_2	CHF_3/O_2	CHF_3/O_2
Flow	52/3	52/3	52/3
Chamber pressure (mTorr)	55	55	55
RF power (W/V)	230 V	285 V	390 V
Temperature(°C)	18	18	18

Table 4.4: Etching series III for defining PC inside the SiN$_x$ hard mask.

radiative recombination rate in the nano cavity is highly sensitive to the surface quality. Thus, the SiN$_x$ etching is optimized to minimize the surface roughness and prevent the roughness transfer to the PC patterned inside the nano-ridge. Optimization was conducted on a test sample (130 nm SiN$_x$ - Si substrate) with ARP ebeam resist patterns using only the RIE mode in an ICP-RIE tool.

The etch recipes for three sample series are shown in Tables 4.2, 4.3, and 4.4. The results were evaluated via cross-sectional SEM imaging. Figure 4.28 displays a top-view SEM image of holes (r = 65 nm) with ARP resist on SiN$_x$. The blue curve represents the location of the cross-section made using Focused Ion Beam and Scanning Electron Microscopy (FIB-SEM). Figures 4.29(a)–(c) present cross-sectional SEM images showing that higher O_2 flow rates result in thinner SiN$_x$ layers. This thinning is accompanied by enhanced etching isotropy, which is attributed to reduced organic passivation on the sidewalls at elevated O_2

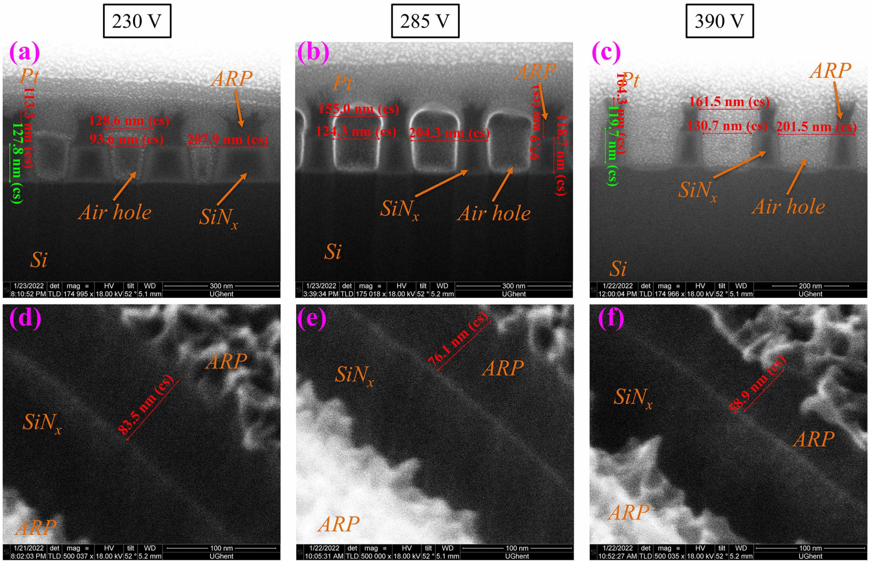

Figure 4.31: (a)-(c) Cross sectional SEM images of the PC and (d)-(f) tilted SEM images of a 100 nm-wide trench etched with different RF powers.

concentrations. Meanwhile, Figures 4.29(d)-(f) display tilted SEM images of 100 nm-wide trenches, revealing that an optimal CHF_3/O_2 ratio (53/3) results in smooth surfaces. Figure 4.29(g) shows nearly vertical trench edges. Figure 4.30 and 4.31 further refine the recipe, varying chamber pressure and RF power. However, vertical stripes persisted on the sidewalls.

The etching rates of SiN_x and the ARP resist, and the SiN_x/ARP selectivity were calculated under varying CHF_3/O_2 gas flows, chamber pressures, and RF powers. The black curve in Figure 4.32 shows a rise in the etching rates for both SiN_x and ARP. During SiN_x etching, increasing O_2 flow reduces CF^{3-} and CF^{2-} passivation layers, while also accelerating the decomposition of ARP (a C-H-based organic compound). As Figure 4.33 shows, the SiN_x/ARP selectivity decreases with increasing O_2 flow, indicating that the ARP resist decomposes faster than SiN_x etches.

Chamber pressure effects are depicted by the red curve in Figure 4.32. Initially, higher pressure enhances reactive plasma density, raising the etching rates. However, beyond 75 mbar, the mean free path of reactive molecules shortens, reducing plasma energy and lowering the etching efficiency and SiN_x/ARP selectivity.

Figure 4.34 shows that increasing RF power continuously raises etching rates for both SiN_x and ARP, attributed to enhanced physical bombardment. This bom-

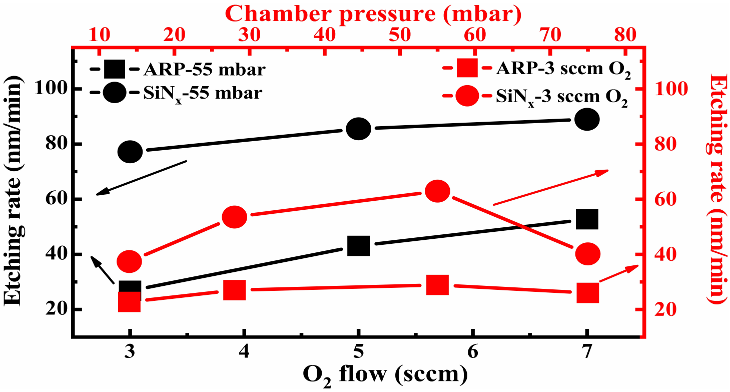

Figure 4.32: Etching rate of ARP and SiN$_x$ with different O$_2$ flows and chamber pressures.

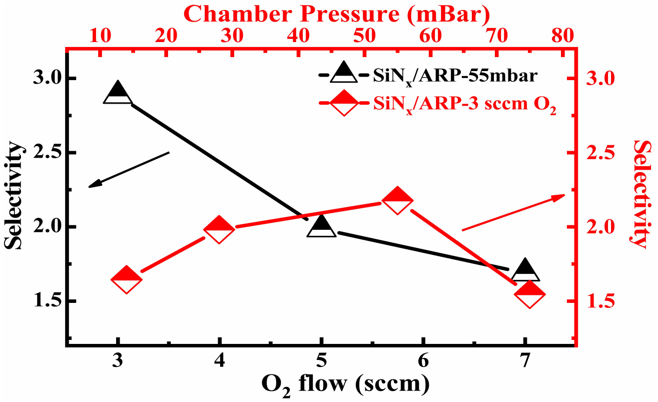

Figure 4.33: Selectivity of SiN$_x$/ARP with different O$_2$ flows and chamber pressures.

bardment affects ARP more significantly than SiN$_x$, further reducing SiN$_x$/ARP selectivity (see Figure 4.35).

Therefore, Recipe 1 was chosen for defining the PC pattern within the SiN$_x$ hard mask, balancing the sidewall roughness and SiN$_x$/ARP selectivity.

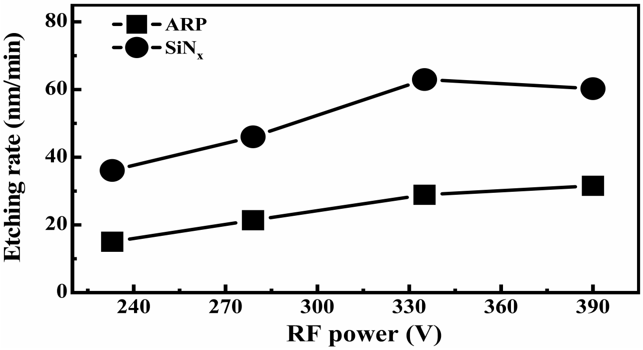

Figure 4.34: Etching rate of ARP and SiN_x with different RF powers.

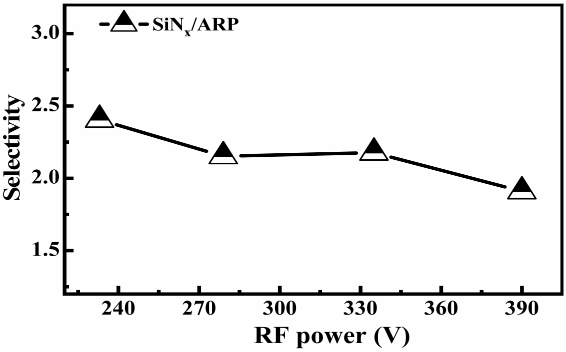

Figure 4.35: Selectivity of SiN_x/ARP with different RF powers.

4.4.2 GaAs and nano-ridge etching

	Recipe 10	Recipe 11	Recipe 12		Recipe 13		Recipe 14	
Gases	BCl_3/N_2	$BCl_3/Ar/N_2$	$BCl_3/Ar/N_2$	Ar	$BCl_3/Ar/N_2$	Ar/SF_6	$BCl_3/Ar/N_2$	Ar/SF_6
Flow	20/12	20/10/4	20/10/4	10	20/10/4	100/5	20/10/4	100/5
Chamber pressure (mTorr)	4	4	4	20	4	20	4	20
RF power (W/V)	150	150	150	42	150	42	150	42
ICP power (W)	400	400	400	400	400	400	400	400
Temperature(°C)	18	18	18	18	18	18	18	18
Etching time per cycle (s)	60	60	30	5	30	5	15	5
Etching cycle	1	1	9		9		9	

Table 4.5: Etching series IV for defining trench in GaAs substrate with the SiN_x hard mask.

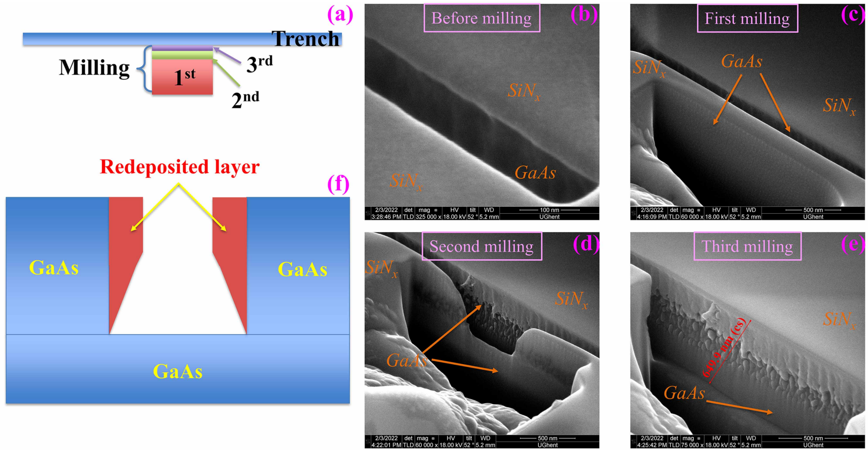

Figure 4.36: (a) Schematic top view of the trench in the test sample with the different milling steps. The tilted SEM images of the trench before(b), and after first(c), second(d), third(e) milling step. (f) Schematic cross sectional view of the trench with the redeposited layer on the side wall surface in the test sample.

Next, the GaAs etch process was optimized using a test sample consisting of a GaAs substrate with a 300 nm SiN_x mask. The test pattern consisted of a elongated trench with the width of 80 nm, defined using EBL. This pattern was transferred in the SiN_x mask using recipe 1 defined in Table 4.2.

The optimization began with Recipe 10 from Table 4.5. To minimize damage or uncertainty to the sidewalls during FIB milling, the process started at a distance from the defined trench and gradually moved closer in steps. Figure 4.36(a) provides a top-view schematic of the trench in the test sample, illustrating the ion milling steps taken to minimize the impact on sidewall surface assessment after etching. Figures 4.36(b)-(d) present tilted SEM images before and after FIB milling, revealing that the redeposition during the etching increases the sidewall roughness. If the

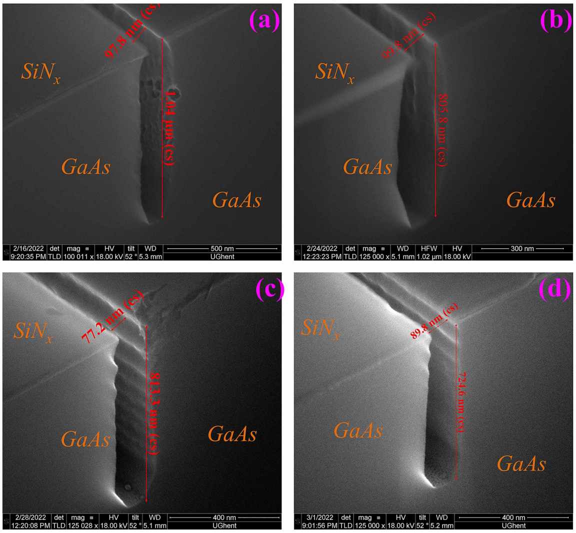

Figure 4.37: The tilted SEM images of the trench with Recipe 11 (a), Recipe 12 (b), Recipe 13 (c) and Recipe 14 (d).

redeposition originated from the milling step, the sidewall surface post-milling would appear rough rather than smooth, as shown in Figure 4.36(c). Figure 4.36(f) illustrates the redeposition on the sidewalls in cross-sectional view.

To remove the redeposited material, physical Ar bombardment during or after GaAs etching (Recipes 11 and 12 in Table 4.5) were tested. Alternatively, Recipe 13 combines a short GaAs etching step followed by chemical etching. Figures 4.37(a)–(b) show that Ar bombardment leaves residual redeposition on the upper sidewall regions, while subsequent etching using SF_6 completely eliminates this residue in Figures 4.37(c)—demonstrating that chemical methods are more effective for redeposition removal. Short etching cycles (15s GaAs etching, 5s redeposition removal from Recipe 14) further improved sidewall smoothness, as shown in Figure 4.37(d).

Finally, the recipe for the hole definition in the GaAs substrate was refined (Table 4.6), accounting for different gas flow requirements between hole and trench structures. Figure 4.38(c) shows that holes etched with Recipe 17 exhibit good top verticality and reduced lateral etching but a long GaAs tail at the bottom, which can be removed through over-etching. As the etching depth increases, gas delivery to the bottom of the holes becomes less efficient, necessitating additional process optimization. To address this, Recipe 18 (outlined in Table 4.7) was developed. The corresponding cross-sectional SEM image in Figure 4.39 confirms that this recipe yields hole structures with strong vertical profiles and minimal lateral etching,

	Recipe 15		Recipe 16		Recipe 17	
Gases	BCl_3/N_2	Ar/SF_6	BCl_3/N_2	Ar/SF_6	BCl_3/N_2	Ar/SF_6
Flow	10/4	100/5	10/8	100/5	10/12	100/5
Chamber pressure (mTorr)	3	20	3	20	3	20
RF power (W/V)	127	42	127	42	127	42
ICP power (W)	400	400	400	400	400	400
Temperature(°C)	18	18	18	18	18	18
Etching time per cycle (s)	15	5	15	5	15	5
Etching cycle	9		9		9	

Table 4.6: Etching series V for defining PC inside GaAs substrate with the SiN_x on top as a hard mask.

indicating successful optimization for deep-hole definition.

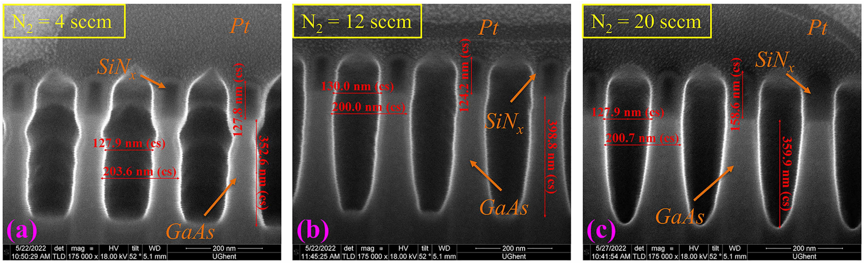

Figure 4.38: Cross sectional SEM images of the holes inside the GaAs substrate with etching Recipe 15 (a), Recipe 16 (b), Recipe 17 (c).

	Recipe 18			
Gases	BCl_3/N_2	Ar/SF_6	BCl_3/N_2	Ar/SF_6
Flow	10/20	100/5	20/4	100/5
Chamber pressure (mTorr)	3	20	3	20
RF power (W/V)	127	42	127	42
ICP power (W)	400	400	400	400
Temperature(°C)	18	18	18	18
Etching time per cycle (s)	15	5	15	5
Etching cycle	2		1	
Total etching cycles	4			

Table 4.7: Etching series VI for defining PC inside GaAs substrate with the SiN_x on top as a hard mask.

To account for the compositional differences within the nano-ridge compared to pure GaAs, the etching process was modified to achieve deeper holes. The detailed steps are provided in Table 4.8, following the sequence (1) + (2) + (1) + (3) + (4). While the cross-sectional SEM image in Figure 4.40 reveals some imperfections, the etching results are sufficiently good for proceeding to the next fabrication stage.

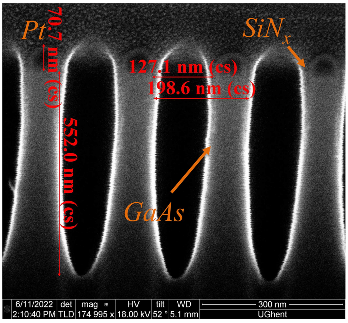

Figure 4.39: Cross sectional SEM image of the holes inside the GaAs substrate with etching Recipe 18.

etching process	(1)		(2)		(3)		(4)	
Gases	BCl_3/N_2	Ar/SF_6	BCl_3/N_2	Ar/SF_6	BCl_3/N_2	Ar/SF_6	BCl_3/N_2	Ar/SF_6
Flow	15/15	100/5	15/15	100/5	12/28	100/5	10/30	100/5
Chamber pressure (mTorr)	3	20	3	20	7	20	9.5	20
RF power (W/V)	127	42	80	42	125	42	180	42
ICP power (W)	400	400	400	400	400	400	400	400
Temperature(°C)	18	18	18	18	18	18	18	18
Etching time per cycle (s)	15	5	15	5	15	5	15	5
Etching cycle	2		1		1		1	

Table 4.8: Definition of etching process for defining PC inside nano-ridge with the SiN_x on top as a hard mask.

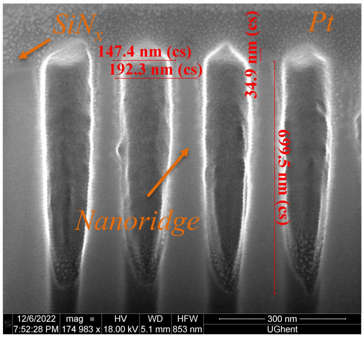

Figure 4.40: Cross sectional SEM image of the holes with the etching process (1)+(2)+(1)+(3)+(4). The definition of the etching processes is given in Table 4.8.

4.4.3 $(NH_4)_2S$ passivation

	Surface oxide removal	Passivation
H_2SO_4 (mL)	1	0
H_2O_2 (mL)	8	0
H_2O (mL)	5000	0
$(NH_4)_2S$	0	New solution
Temperature (°C)	20	50
Time (s)	10	10×60
Rinse	Water	N_2

Table 4.9: The passivation flow.

Series number	New solution	Solution used for being diluted	The volume of solution used for being diluted	DI water volume
1	20 %	40 %(w/w) $(NH_4)_2S$	2 mL	2 mL
2	PH = 10	40 %(w/w) $(NH_4)_2S$	2 mL	100 mL
3	PH = 9	PH = 10	10 mL	100 mL
4	PH = 8	PH = 9	10 mL	50 mL

Table 4.10: The passivation solution with different $(NH_4)_2S$ concentrations.

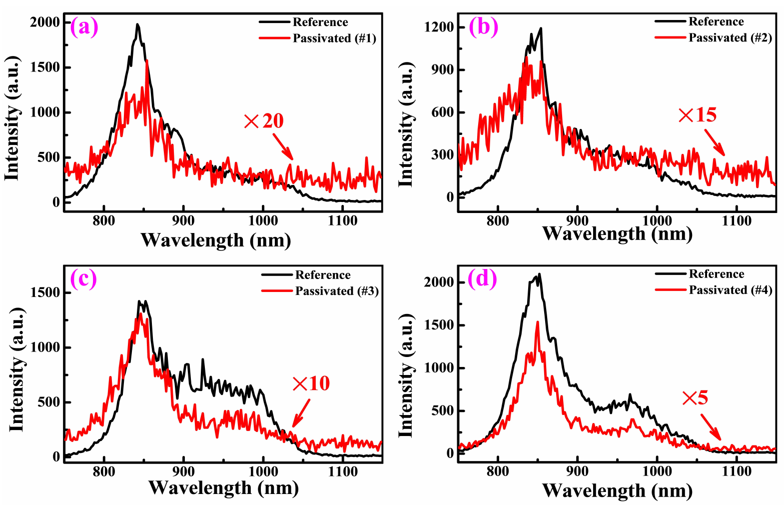

Figure 4.41: PL spectra from the reference samples and samples passivated using the solution with different $(NH_4)_2S$ concentrations.

During PC patterning in a nano-ridge with etching, the QW layers and GaAs barriers are damaged. This introduces surface defects, leading to carrier capture and non-radiative recombination. Effective passivation is essential to mitigate these effects. Previous studies [134–137] demonstrated that $(NH_4)_2S$ passivation, following surface oxide removal using an H_2SO_4:H_2O_2:H_2O solution, effectively reduces surface defects on GaAs surfaces. Here, we evaluate the passivation results using PL and TRPL measurements.

To assess the impact of the $(NH_4)_2S$ concentration on surface passivation, the samples were treated with various concentrations, as detailed in Tables 4.9 and 4.10. Figure 4.41 shows that the PL peak intensities for the passivated samples are significantly lower than those of the reference samples. Figure 4.42 illustrates the low ratio of the integrated PL intensities near the peaks for passivated versus reference samples. This indicates that varying $(NH_4)_2S$ concentrations does not effectively reduce surface defects.

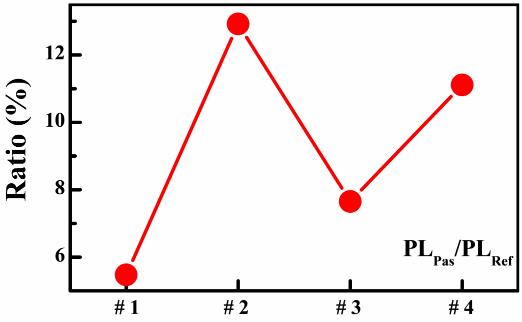

Figure 4.42: Ratio of the integrated PL intensities from the reference samples and samples passivated using solutions with different $(NH_4)_2S$ concentrations.

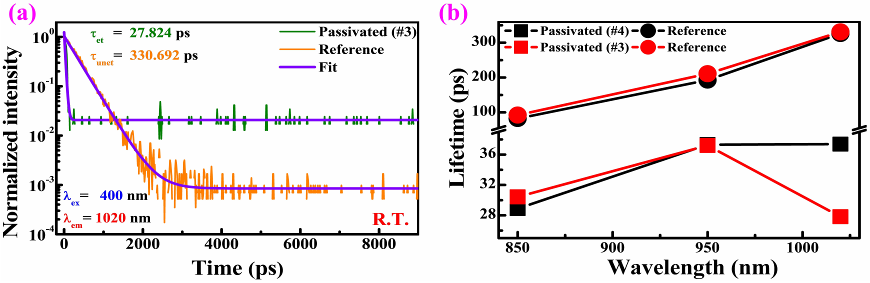

Figure 4.43: (a) Decay traces of the 1020 nm emission from the reference sample and sample passivated using #3 solution. (b) The lifetimes of different wavelength emissions from the reference samples and samples passivated using #3 and #4 solutions.

TRPL measurements under 400 nm excitation were conducted to assess material quality. As shown in Figure 4.43(a), the reference sample exhibits a carrier lifetime approximately ten times longer than that of a sample passivated with #3 solution. Figure 4.43(b) presents lifetimes at 850 nm, 950 nm, and 1020 nm for both passivated and reference samples, corresponding to emission from the GaAs barriers and the QW layers. The shorter lifetimes in passivated samples indicate the non-radiative recombination centers introduced from the etching and ineffective passivation, consistent with the PL results. Figure 4.44 presents 2D plots of the

TRPL signals across various wavelengths for both passivated and reference samples, treated with different concentrations of $(NH_4)_2S$. The observation of shorter carrier lifetimes across most wavelengths in the passivated samples further emphasizes the need for enhanced passivation strategies to improve surface quality and carrier dynamics.

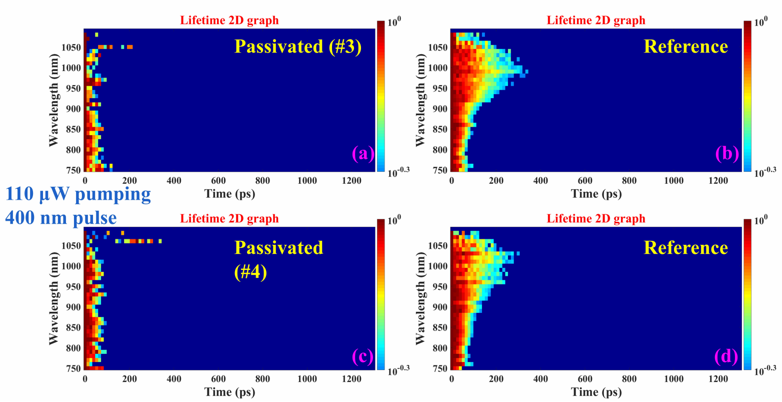

Figure 4.44: 2D graph of TRPL signal from the reference samples and samples passivated using #3 and #4 solutions.

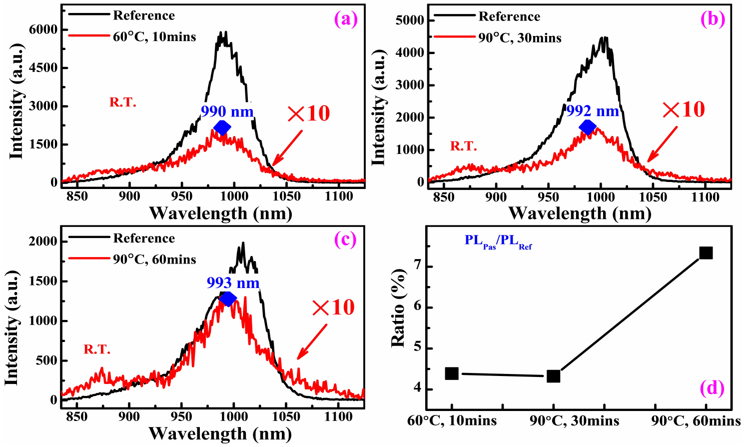

Figure 4.45: PL spectra from the reference samples and samples passivated using #3 solution for (a) 10 mins at 60 °C, (b) 30 mins at 90 °C, (c) 60 mins at 90 °C and (d) the ratio of the integrated PL intensities from these samples.

The poor passivation is likely caused by the insufficient temperature and duration during the process. To address this, both parameters were increased. However, as shown in Figures 4.45(a)-(c), the PL peak intensities of passivated

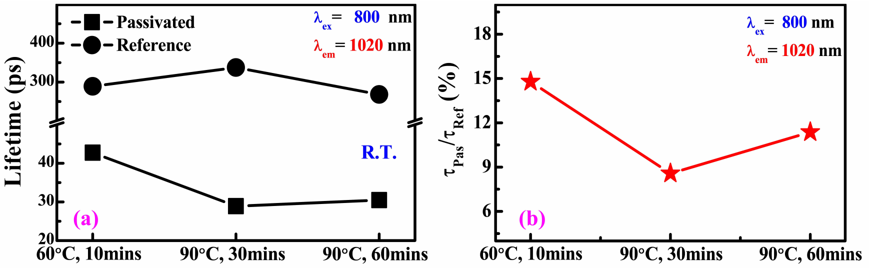

Figure 4.46: (a) Lifetime of 1020 nm emission from the same samples in Figure 4.45. (b) Ratio of lifetime from the reference and passivated samples in (a).

samples remain significantly lower than those of reference samples. Figure 4.45(d) further confirms this with a low ratio of integrated PL intensity between passivated and reference samples, indicating ineffective passivation. Similarly, Figures 4.46(a)-(b) reveal shorter lifetimes and lower lifetime ratios for the passivated samples, further suggesting inadequate passivation.

Plasma passivation [138,139] presents a potential alternative, though it requires further investigation and is not discussed here. Another viable approach for PC nano-ridge lasers involves defining holes that extend from the top of the nano-ridge down to the first QW layer, without penetrating the QW layers. This approach minimizes damage to the active region and eliminates the need for passivation. Consequently, the remainder of this section focuses on nano-ridge lasers with shallow etched holes.

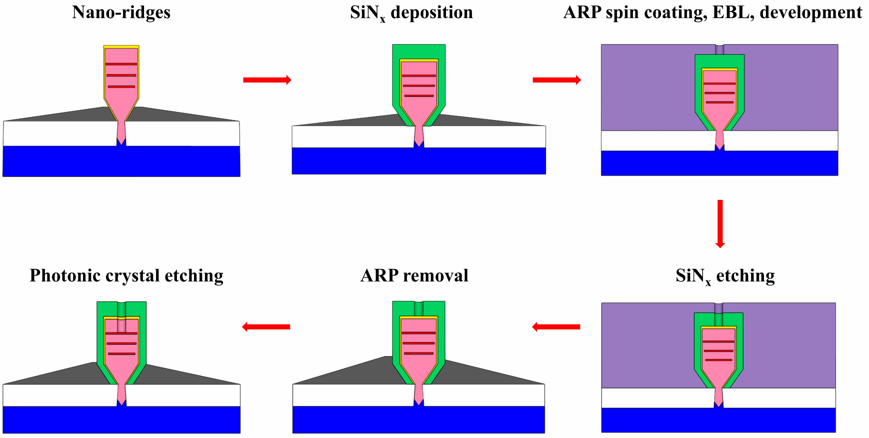

Figure 4.47: Process flow of PC nano-ridge cavity fabrication.

Following the same design principle, a PC nano-ridge laser with the shallow etched holes and Gaussian-shape electric field distribution was created. In this case we used a nano-ridge sample with $\mathrm{In_{0.45}Ga_{0.55}As/In_{0.25}Ga_{0.75}As}$ QWs, targeting a wavelength of 1.31 µm, which is relevant for optical interconnect applications.

The fabrication process, outlined in Figure 4.47, begins with the growth of the $\mathrm{In_{0.25}Ga_{0.75}As}$ nano-ridges containing three $\mathrm{In_{0.45}Ga_{0.55}As}$ QWs, passivated with an InGaP layer. A 100 nm SiN_x hard mask was deposited on the nano-ridge using PECVD, followed by ARP resist spin coating for EBL. PC cavities structures with varying periods were patterned into the ARP resist. These patterns were transferred into the SiN_x hard mask and nano-ridge using ICP-RIE with $\mathrm{CHF_3/O_2}$ and $\mathrm{BCl_3/N_2}$, respectively.

Top-view SEM images of the PC nano-ridge laser, shown in Figure 4.48(a) and (b), exhibit well-aligned, circular-shaped holes, validating the effectiveness of the fabrication process.

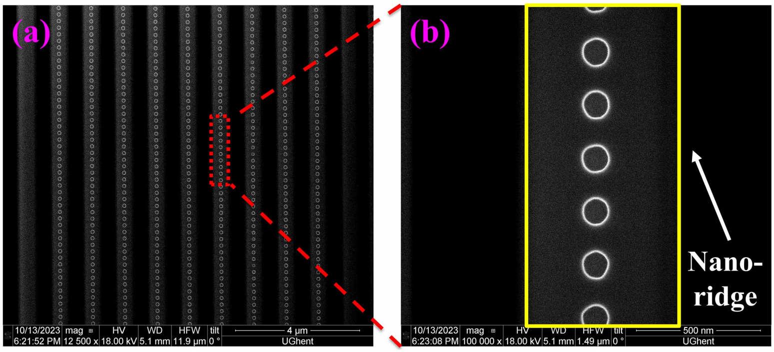

Figure 4.48: (a) Top-view SEM image of PC nano-ridge laser. (b) Enlarged SEM image of the etched holes in a nano-ridge.

4.5 Optical characterization

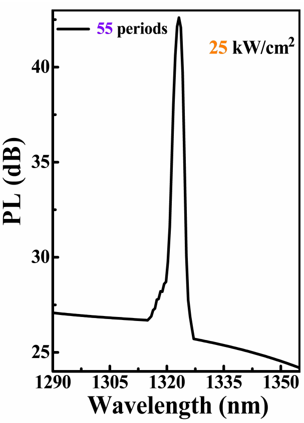

Figure 4.49: PL spectrum on a logarithmic scale from the PC laser with h_{etched} = 130 nm and 55 periods in the mirror block under 25 kW/cm^2 532 nm-pulsed pump power density.

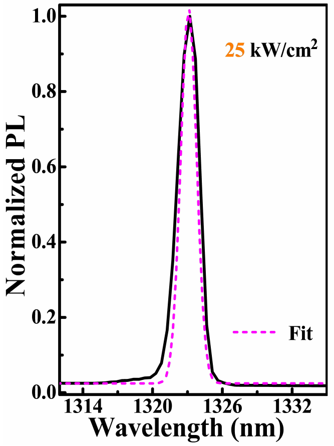

Figure 4.50: Normalized PL spectrum of the PC laser from Figure 4.49, fitted with a Gaussian function.

The devices were characterized under pulsed optical pumping, as detailed in Section 2.6. Figure 4.49 presents the PL spectrum from a PC laser based on a nano-ridge that is 877 nm high and 462 nm wide, featuring an etched hole height (h_{etched}) of 130 nm and comprising 55 periods in the mirror block, under a power density of 25 kW/cm^2. The PC laser exhibits a peak emission at 1323 nm, with a SMSR exceeding 17 dB. The laser's linewidth, derived from Gaussian fitting (Figure 4.50), is 1.61 nm, likely limited by the pulsed operating regime.

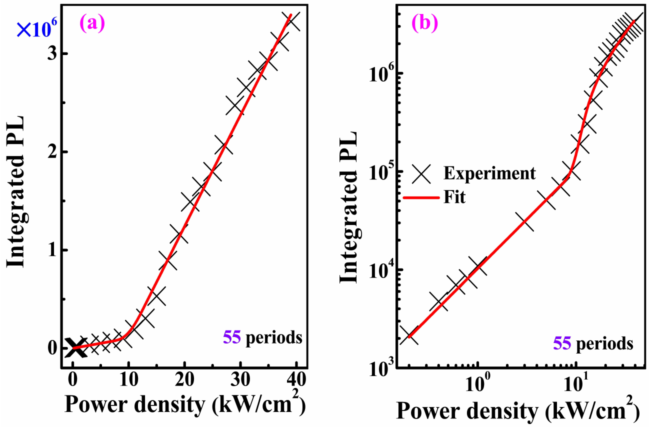

Figure 4.51: Light in - Light out curve on a linear (a) and logarithmic (b) scale of this PC laser.

To further analyze the lasing behavior, we measured the light-in (pump power density) versus light-out (integrated PL) curve from the same device on both logarithmic and linear scales. A clear slope change in Figure 4.51(a) and the characteristic S-shaped curve in Figure 4.51(b) signify the lasing turn-on. Fitting the curve to the rate equations [118, 119] gives a coupling efficiency (β) of approximately 0.9 % from the spontaneous emission to the cavity mode.

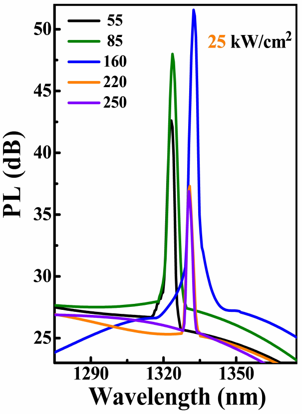

Figure 4.52: PL spectra on a logarithmic scale from PC lasers with various numbers of periods in the mirror block at 25 kW/cm^2.

The optical properties of PC lasers with various numbers of periods in the mirror block were further investigated. The PL spectrum and light-in versus light-out curves (on a linear scale) indicate that all devices achieve lasing at 25 kW/cm^2,

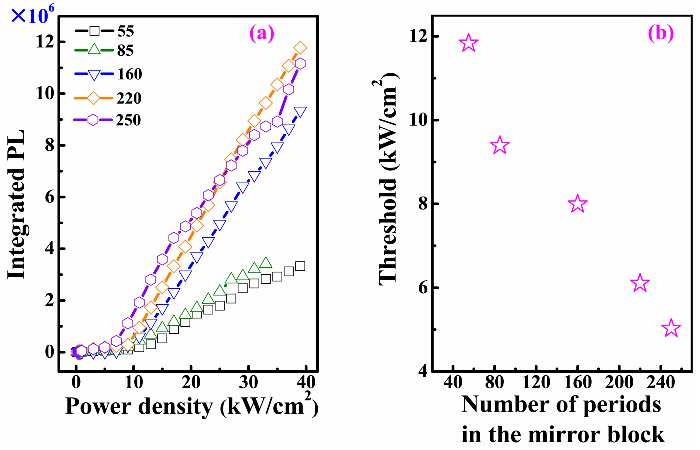

Figure 4.53: (a) Light in - Light out curves on a linear scale and (b) the extracted threshold values of the PC lasers from (a).

with the smallest cavity dimension being 25 µm (corresponding to 55 periods in the mirror block), as shown in Figure 4.52. Threshold values extracted from the linear light-in versus light-out curves (Figure 4.53(a) and 4.53(b)) reveal thresholds of 11.83 kW/cm^2 and 5.03 kW/cm^2 for PC lasers with 55 and 250 periods in the mirror block, corresponding to cavity lengths of 25 µm and 103 µm, respectively. The decrease in threshold values with increasing mirror block periods is attributed to enhanced light confinement provided by the additional periods.

To get insight in the device performance, the important internal parameters including the internal quantum efficiency (IQE, η_i), differential quantum efficiency (EQE, η_d), internal loss α_i, modal gain Γg_0 and transparency power density P_{tr} are investigated.

The original data is plotted as function of the pump power density. To allow the extraction of the internal loss and modal gain using the standard equations from literature, we first have to replot the data as function of the pump power reaching the actual device. In practice this means we have to multiply the pump power by the device length and width (Figure 4.54).

To extract the internal loss and modal gain, we first calculate η_d from the slope of each light-in–light-out curve in Figure 4.54:

$$\eta_d = \frac{d(Counts_{em})}{d(Counts_{ex})} \tag{4.26}$$

where $Counts_{ex}$ and $Counts_{em}$ represent the excited and emitted counts, respec-

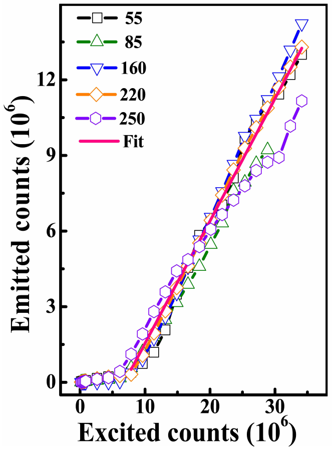

Figure 4.54: Counts$_{ex}$ - Counts$_{em}$ curves of PC lasers with different cavity lengths, fitted with a linear function.

tively. Figure 4.55 plots the inverse DQE ($1/\eta_d$) as a function of cavity length L, fitted using:

$$\frac{1}{\eta_d} = \frac{1}{ln(\frac{1}{R})} \cdot \frac{1}{\eta_i} \cdot \alpha_i \cdot L + \frac{1}{\eta_i} \tag{4.27}$$

where R denotes the grating reflectivity. Using the simulated grating reflectivity of R = 0.74 for 55 periods, we extract η_i = 61.66 % and α_i = 9.49 cm^{-1}.

The threshold gain g_{th} and the material gain coefficient g_0 satisfy:

$$g_{th} = g_0 \cdot ln(\frac{P_{th}}{P_{tr}}) \tag{4.28}$$

The threshold modal gain Γg_{th} is given by:

$$\Gamma g_{th} = \alpha_i + \alpha_m \tag{4.29}$$

where

$$\alpha_m = \frac{1}{L} ln(\frac{1}{R}) \tag{4.30}$$

Combining equations (4.28) - (4.30), the threshold power density is expressed as:

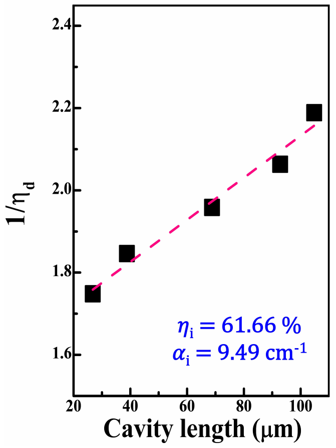

Figure 4.55: Inverse differential quantum efficiency as a function of cavity length, fitted with a linear function.

$$ln(P_{th}) = ln(P_{tr}) + \frac{\alpha_i}{\Gamma g_0} + \frac{1}{\Gamma g_0} \cdot ln(\frac{1}{R}) \cdot \frac{1}{L} \tag{4.31}$$

where P_{tr} is the transparency power density and Γg_0 is the model gain. By fitting the natural logarithm of the threshold values using equation (4.31), as shown in Figure 4.56, we extrapolate the modal gain and transparency power density of PC lasers to be Γg_0 = 111.93 cm^{-1} and P_{tr} = 4.18 kW/cm^2. Given the simulated Γ = 4.88%, we extrapolated g_0 = 2292.6 cm^{-1} and g_{th} = 2385.16 cm^{-1}, respectively, where g_{th} is calculated using equation (4.28).

The material gain or threshold material gain in various QW lasers such as InGaAs, InGaN and InGaAsP typically ranges from approximately 500 cm^{-1} to 3000 cm^{-1} [140–143]. However, theoretical calculations often predict higher values [144–146]. By utilizing hybrid quantum well-dots, the material gain range can exceed 10^4 cm^{-1} [147, 148]. It is important to note that these experimental values depend on factors such as barrier material composition, strain, wavelength, specific device designs, and operating conditions. Therefore, direct comparisons between our material and these values are not straightforward.

In this data analysis, we assume 100 % light absorption. The calibration accounts for emitted counts while considering the simulated PC reflectivity (74 %), the simulated grating coupling efficiency (5.42 %), objective lens collection efficiency (16.9 %), dichroic mirror transmission efficiency ($\sim$ 100 %), focal lens collection efficiency before the monochromator (2.55%), diffraction grating efficiency (70 %), and detector efficiency (7.42 %).

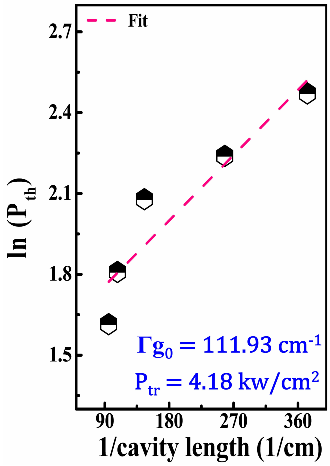

Figure 4.56: Natural logarithm of threshold power density as a function of the reciprocal cavity length, fitted with a linear function.

However, this model is only strictly valid for FP lasers and there is a large uncertainty on the actually absorbed pump power. Nevertheless, these results still provide valuable insight into the device's performance.

In PL spectra, the vertical axis (”counts”) reflects the CCD-detected signal, proportional to the number of photons collected. Emitted optical energy can be estimated via:

$$E_{em} = Counts_{em} \cdot E_{photon} = Counts_{em} \cdot \frac{hc}{\lambda_{pump}}$$

where E_{em} is the emitted energy, $Counts_{em}$ is the CCD-detected signal, E_{photon} is the photon energy, h is Planck's constant, c is the speed of light, and λ_{pump} is the pump wavelength. This assumes linear CCD response and uniform spectral sensitivity across the measured range. For accurate interpretation, the calibration must incorporate the total light collection efficiency along the entire optical path, as detailed above.

4.6 Conclusion

In conclusion, the design principles of a photonic crystal laser achieving a Gaussian distribution profile have been presented. However, fabrication challenges remain, particularly in etching the nano-ridge and passivating the active region. The extension of etching through the entire nano-ridge and ineffective passivation result in damage to the quantum well layers, degrading the material's optical performance. This motivates the exploration of photonic crystals with shallower etched depths within the nano-ridge. However, designs featuring deep-etched holes can serve as high-reflection mirrors for single-photon sources or as individual photonic crystal lasers with holes defined in passive structures.

Lasers with varying hole periods in the mirror block and an etched height of 130 nm were defined within the $In_{0.45}Ga_{0.55}As/In_{0.25}Ga_{0.75}As$ nano-ridge, grown directly on a standard 300 mm silicon wafer. This design enables lasing with a cavity length of only 25 µm, a threshold of 11.83 kW/cm^2, a side-mode suppression ratio of 17 dB, and a linewidth of 1.61 nm from Gaussian fitting at 25 kW/cm^2. Under pulsed optical pump, the lowest lasing threshold of approximately 5.03 kW/cm^2 was observed in a PC laser with 250 mirror block periods. This demonstration highlights the high quality of III-V-on-silicon epitaxial material and marks a significant step toward electrically driven devices with low power consumption and a small footprint for silicon photonic platforms.

5

Conclusion and outlook

5.1 Conclusion of the presented work

This thesis explores three different cavity designs for realizing low-threshold, compact nano-ridge laser devices, monolithically grown on 300 mm silicon substrates. These lasers advance the potential of the electrically driven applications.

First, a novel design incorporating an amorphous silicon grating atop the nano-ridge was investigated, to reduce the lasing threshold compared to the conventional etched gratings. Simulations indicate that the TE-like fundamental optical mode exhibits the highest confinement factor. A distributed feedback cavity with a $\lambda/4$ shift section in the center was optimized to balance the light interaction with the grating with the mode confinement within the quantum well layers. A grating period of 161 nm enabled lasing at the center of the photoluminescence spectrum ($\sim$ 1044 nm). A crucial fabrication step involves incorporating a cured benzocyclobutene (BCB) protection layer, to avoid interaction between the amorphous silicon layer and the developer for the electron beam resist, HSQ. Room-temperature measurements confirmed the single-mode lasing at 1044 nm, with a side-mode suppression ratio exceeding 35 dB, a linewidth of 1.5 nm, and a threshold of 7.84 kW/cm^2—five times lower than devices with an etched grating. This threshold reduction is attributed to the amorphous silicon grating process, which minimizes the introduced surface defects and active region damage.

Secondly, we explore nano-ridge lasers with amorphous silicon gratings deposited on the sides, targeting at the device miniaturization. Similarly, simulations indicate the potential of lasing for the TE-like fundamental optical mode due to its larger confinement factor. Again, a distributed feedback cavity with a $\lambda/4$ shift is optimized by balancing the light interaction with the amorphous silicon grating and the mode confinement in the quantum well layers. The optical properties of devices with varying numbers of grating periods are characterized using room temperature PL spectra. The device featuring a 100-period amorphous silicon grating demonstrates lasing with a remarkably compact cavity length of only $\sim$ 16 µm, achieving a lasing threshold of $\sim$ 9.9 kW/cm^2. Additionally, the PL spectrum confirms single-mode laser operation with a side-mode suppression ratio exceeding 24 dB and a linewidth of 1.25 nm, determined through a Gaussian fitting at 25 kW/cm^2. The linewidth is limited by the pulsed optical pumping.

Finally, an apodized photonic crystal cavity with holes etched throughout the nano-ridge was proposed, to achieve both low threshold and small footprint. By fixing the hole radius and optimizing the period, a Gaussian electric field envelope was created along the photonic crytal axis. The calculation for the band structure and the design principles apodized cavity were derived. However, fabrication challenges remain, particularly in etching the nano-ridge and passivating the active region. The extension of etching through the entire nano-ridge and ineffective passivation with the ammonium sulfide result in damage to the quantum well layers and degrade the material's optical performance. To mitigate the active region damage, the hole etching was halted at the top of the first quantum well layer, without penetrating any quantum well layers. To address currently used fiber-optic datacom systems, nano-ridges with 45 % indium content for the quantum well layers and 25 % for the barriers were chosen, enabling emission in the O-band. apodized photonic crystal cavities were optimized for the TE-like ground mode for O-band emission. Lasers with a minimum cavity length of $\sim$ 25 µm and an etched height of 130 nm demonstrated a threshold of 11.83 kW/cm^2, a side-mode suppression ratio of 17 dB, and a linewidth of 1.61 nm. Under pulsed optical pumping, a lasing threshold of 5.03 kW/cm^2 was observed for a device with cavity length of 103 µm.

The successful demonstration of these laser designs confirms the high quality of the nano-ridge structures and establishes a foundation for large-scale manufacturing of silicon photonic integrated circuits, including the III-V lasers and amplifiers.

5.2 Outlook

Since initiating work on this platform in 2019, we have proposed three promising demonstrations of optically pumped lasers. However, significant advancements are still required to be able to deliver practical lasers for the commercial market. The requirements for fully exploiting epitaxial nano-ridges include, but are not limited to:

1. Realizing a continuous-wave (CW) pumped laser
2. Achieving electrical injection
3. Extending the operating wavelength to the O-band or C-band while improving the material quality of these nano-ridges

Thus far, we have demonstrated a low-threshold, small-footprint device under pulsed optical pumping. To estimate the equivalent electrical threshold current I_{th} from the measured optical threshold power P_{th}, the rate of electron-hole pair generation under optical pumping is first determined and then related to an equivalent electrical injection current. The number of absorbed photons per second is given by:

$$R_{photon} = \frac{P_{th}\eta_{abs}}{E_{photon}} = \frac{P_{th}\eta_{abs}\lambda_{pump}}{hc}$$

where η_{abs}, E_{photon}, h, c and λ_{pump} are the absorption efficiency, photon energy, Planck's constant, light speed and pump wavelength. To convert this into an equivalent electrical current, the photon generation rate is multiplied by the elementary charge q:

$$I_{th} = q \cdot R_{photon} = \frac{q\lambda_{pump}}{hc} P_{th}\eta_{abs}$$

With considering the side grating cavity $q = 1.6 \times 10^{-19}C$, $\lambda_{pump} = 532 \times 10^{-9}m$, $h = 6.626 \times 10^{-34}$, $c = 2.99792458 \times 10^{8}m/s$, $P_{th} = 9.9kW/cm^2$, $\eta_{abs} = 100\%$, the electrical threshold current density can be estimated as $I_{th} = 42.4kA/cm^2$. This first-order estimate assumes ideal conditions such as perfect carrier injection. Compared to typical InGaAs or InP quantum well lasers operating at near-infrared wavelengths, which generally exhibit threshold current densities in the range of $1 - 20kA/cm^2$ [110,149,150], the estimated value here is significantly higher. This discrepancy is likely attributed to the use of non-optimized materials, particularly when compared to the recently demonstrated GaAs nano-ridge structures employed in laser diode fabrication [125]. In reality, factors like nonradiative recombination, limited carrier capture, and lateral current spreading increase the actual electrical threshold. Nonetheless, this calculation provides a useful baseline for correlating optical and electrical pumping, informing future device design.

Realizing a practical CW-pumped laser with reduced dimensions requires further improvements, such as achieving an even lower threshold and, importantly, enhancing heat dissipation efficiency. Further optimizing the laser design and fabrication processes is crucial. Possible pathways include better control of the interaction of the field with the gratings, implementing a more gentle modulation of the periodicity in the photonic crystal cavity, and reducing optical loss by decreasing etched sidewall roughness.

Thermal management remains a major challenge for micro- and nanoscale active devices due to significant heat generation in confined volumes. Although the thermal impedance of the nano-ridge structures has not been directly quantified, insightful observations can be made based on device geometry and known thermal behavior [151–154]. Several factors contribute to thermal resistance in nano-ridge lasers:

- Small active volumes result in high power densities and poor lateral heat spreading.
- Heat dissipation is constrained to narrow trenches connecting the active region to the silicon substrate.
- Air cladding and trench isolation from fabrication steps further impede heat extraction.

These constraints indicate that the current nano-ridge design presents a pronounced thermal bottleneck—particularly under continuous-wave or electrically pumped conditions—even in the absence of simulation or direct measurements. Moreover, the high-temperature operational stability of optically pumped nano-ridge lasers has not yet been experimentally assessed in this work. Nonetheless, recent studies on GaAs-based nano-ridge laser diodes have shown promising results, including continuous-wave operation up to 60 °C and a thermally induced redshift in emission wavelength. To address these thermal limitations, future device iterations should prioritize thermal design enhancements. Promising approaches include integrating heat-spreading layers, improving thermal coupling to the substrate, and incorporating planarization materials such as SiN_x or SiO_2 to facilitate more efficient heat extraction.

Electrical injection is a crucial milestone for commercializing this laser plat-

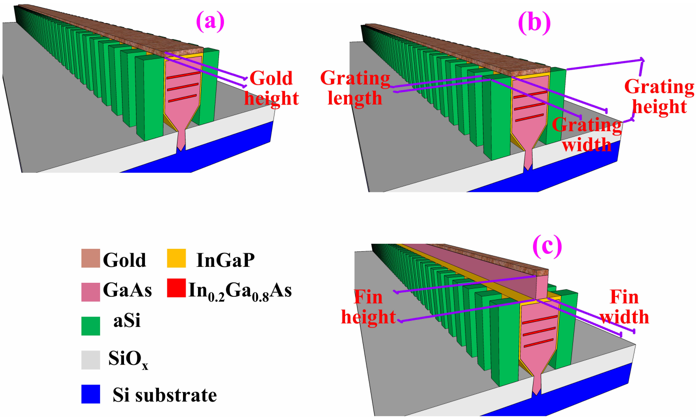

Figure 5.1: Electrically-driven device model with side aSi gratings, targeting at optimizing the p contact thickness (a), shortening side aSi grating height (b) and designing the dimensions of the FIN structure (c).

form but presents several challenges. Achieving a uniform p- and n-doping profile while preserving the intrinsic quantum well region to form a p-i-n junction is particularly difficult. This challenge is exacerbated by uncontrollable dopant diffusion and segregation, which require further advancements to address [155, 156]. Establishing good ohmic contacts between III-V materials and metal pads requires careful selection of dopants and concentrations. However, metal pads on nano-ridge lasers significantly contribute to optical losses [157], necessitating a trade-off between efficient carrier injection and optical performance. Two design approaches aim to mitigate this trade-off: one uses a continuous p-contact atop the nano-ridge with aSi gratings on the sides; the other adopts a FIN structure, as shown in Figure 5.1(a) and (c). Optimizing the p-contact thickness in Figure 5.1(a), reducing the aSi grating height in Figure 5.1(b), and tuning the dimensions of the FIN structure in Figure 5.1(c)—together with a continuous p-contact—can enhance carrier injection while minimizing optical loss. The n-contact is positioned next to the nano-ridge and connected to the n-doped silicon substrate, enabling current to flow through the nano-ridge structure.

Once electrical injection is achieved, high-speed characterization should be performed to evaluate the feasibility of nano-ridge lasers for fiber-optic communication systems.

Reliability is another critical concern for the nano-ridge lasers, as demonstrated in studies of the InGaAs/GaAs nano-ridge p-i-n diodes [125]. Ping-Yi et al. [151, 152] identified that the current crowding and Joule heating near the p-contact lead to the defect formation and Ti diffusion within the GaAs nano-ridge.

These issues disrupt the gain medium and result in the device degradation and breakdown. The sintering process reduces p-contact resistance and enhances electrical injection [153]. However, the further investigation into the diffusion mechanism and optimization of the p-contact design is necessary.

Further enhancements to the $In_{0.45}Ga_{0.55}As/In_{0.25}Ga_{0.75}As$ nano-ridge are essential for high-performance O-band emission. These include increasing the aspect ratio of STI trenches, incorporating strain-compensating layers [158], and optimizing annealing processes. An alternative approach to extend the operating wavelength is using self-assembled quantum dots [159]. However, switching from InGaAs quantum wells to GaAs or InAs quantum dots would indeed have a significant impact on both device design and fabrication strategy.

- First, QDs exhibit an inhomogeneously broadened gain spectrum. This means we would need to carefully adapt the grating period or photonic crystal cavity parameters to ensure good overlap between the cavity mode and the broader gain profile.

- Second, QDs are more robust against defects and temperature variations [160]. This increased tolerance allows us to explore more aggressive cavity geometries—for instance, we could consider deeper photonic crystal etching. While some dots would be etched away, the remaining QDs are more defect-tolerant, so lasing might still be achievable without extensive surface passivation.

- Third, although quantum dots offer several advantages, there is a challenge—particularly in achieving high dot density and uniformity requiring growth parameter optimization [161].

So, switching to quantum dots would require rethinking the optical design—but in return, we could see benefits for threshold reduction and temperature stability, which are key benefits for on-chip integration.

The wafer scale process pose another challenge for the commercial application. Recent studies from IMEC on GaAs-based nano-ridge laser diodes have already demonstrated the feasibility of wafer-scale nano-ridge growth, laser definition, and characterization using a 300 mm CMOS pilot line. However, this PhD project relies on a compact grating structure to define the laser cavity, which currently necessitates high-resolution patterning via EBL. Additionally, the multi-pass ICP-RIE etching process for aSi must also be required.

While EBL is suitable for performance exploration and prototyping, its serial and time-intensive nature makes it unsuitable for large-scale manufacturing. A more scalable alternative is immersion lithography, commonly used in deep ultraviolet (DUV) lithography systems. This method is well-established for 300 mm wafer processing and has the potential to realize high-resolution aSi gratings.

However, scaling the multi-pass ICP-RIE etching process to full-wafer aSi gratings presents challenges, particularly the loading effect in areas with different feature sizes. These issues must be addressed through further process optimization—especially for the fabrication of dense laser arrays.

Although the current aSi grating fabrication flow has been optimized for research-scale prototyping, it establishes a solid foundation. The transition to immersion lithography offers a promising pathway toward scalable, high-performance manufacturing.

References

[1] Krishna C. Saraswat and Farrokh Mohammadi. *Effect of Scaling of Interconnections on the Time Delay of VLSL Circuits.* IEEE Transactions On Electron Devices, 4(29):645–650, 1982.

[2] Joseph W. Goodman, Frederick I. Leonberger, Sun yuan Kung, and Ravindra A. Athale. *Optical Interconnections for VLSL system.* Proceedings of the IEEE, 72(7):850–866, 1984.

[3] Yasuhiko Arakawa, Takahiro Nakamura, Yutaka Urino, and Tomoyuki Fujita. *Silicon Photonics for Next Generation System Integration Platform.* IEEE Communications Magazine, 3(51):72–77, 2013.

[4] Bahram Jalali and Sasan Fathpour. *Silicon Photonics.* Journal Of Lightwave Technology, 24(12):4600–4615, 2006.

[5] Richard A. Soref. *The Past, Present, and Future of Silicon Photonics.* IEEE Journal of Selected Topics in Quantum Electronics, 12(6):1678–1687, 2006.

[6] Richard A. Soref and J.P. Lorenzo. *Electronic letters-Single crystal silicon a new material for 1.3 and 1.6 um integrated optical components.* Electronic Letters, 21(21):953–954, 1985.

[7] Richard A. Soref. *All-Silicon Active and Passive Guided-Wave Components for* λ *= 1.3 and 1.6um.* IEEE Journal Of Quantum Electronics, 22(6):873–879, 1986.

[8] Kevin K. Lee, Desmond R. Lim, Lionel C. Kimerling, Jangho Shin, and Franco Cerrina. *Fabrication of ultralow-loss Si-*SiO_2 *waveguides by roughness reduction.* Optics Letters, 26(23):1888–1890, 2001.

[9] Jaime Cardenas, Carl B. Poitras, Jacob T. Robinson, Kyle Preston, Long Chen, and Michal Lipson. *Low loss etchless silicon photonic waveguides.* Optics Express, 17(6):4752–4757, 2009.

[10] Daniel K. Sparacin, Steven J. Spector, and Lionel C. Kimerling. *Silicon waveguide sidewall smoothing by wet chemical oxidation.* Journal of Lightwave Technology, 23(8):2455–2461, 2005.

[11] F. Gao, Y.Wang, G. Cao, X. Jia, and F. Zhang. *Improvement of sidewall surface roughness in silicon-on-insulator rib waveguides.* Applied Physics B - Lasers and Optics, 81:691–694, 2005.

[12] Cyril Bellegarde, Erwine Pargon, Corrado Sciancalepore, Camille Petit-Etienne, Vincent Hugues, Daniel Robin-Brosse, Jean-Michel Hartmann, and Philippe Lyan. *Improvement of Sidewall Roughness of Submicron SOI Waveguides by Hydrogen Plasma and Annealing.* IEEE Photonics Technology Letters, 30(7):591–594, 2018.

[13] Po Dong, Wei Qian, Shirong Liao, Hong Liang, Cheng-Chih Kung, Ning-Ning Feng, Roshanak Shafiiha, Joan Fong, Dazeng Feng, Ashok V. Krishnamoorthy, and Mehdi Asghari. *Low loss shallow-ridge silicon waveguides.* Optics Express, 18(14):14474–14479, 2010.

[14] Shihan Hong, Long Zhang, Yi Wang, Ming Zhang, Yiwei Xie, and Daoxin Dai. *Ultralow-loss compact silicon photonic waveguide spirals and delay lines.* Photonic Research, 10(1):1–7, 2022.

[15] Angelo Bozzola, Lee Carroll, Dario Gerace, Ilaria Cristiani, and Lucio Claudio Andreani. *Optimising apodized grating couplers in a pure SOI platform to -0.5 dB coupling efficiency* . Optics Express, 23(13):16289–16304, 2015.

[16] Zhi Liu, Jiashun Zhang, Xiuli Li, Liangliang Wang, Jianguang Li, Chunlai Xue, Junming An, and Buwen Cheng. *25×50 Gbps wavelength division multiplexing silicon photonics receiver chip based on a silicon nanowire-arrayed waveguide grating.* Photonics Research, 7(6):659–663, 2019.

[17] Zhiyu Chen, Lianshan Yan, Yan Pan, Lin Jiang, Anlin Yi, Wei Pan, and Bin Luo. *Use of polarization freedom beyond polarization-division multiplexing to support high-speed and spectral-efficient data transmission.* Light: Science & Applications, 6:16207:1–7, 2017.

[18] Yousef Fazea and Vitaliy Mezhuye. *Selective mode excitation techniques for mode-division multiplexing: a critical review.* Optical Fiber Technology, 45:280–288, 2018.

[19] Shipeng Wang, Hao Wu, Ming Zhang, and Daoxin Dai. *A 32-channel hybrid wavelength-/mode-division (de) Multiplexer on silicon.* IEEE Photonics Technology Letters, 30(13):1194–1197, 2018.

[20] Weifeng Jiang, Jinye Miao, and Tao Li. *Compact silicon 10-mode multi/demultiplexer for hybrid mode- and polarisation-division multiplexing system.* Scientific Reports, 9:13223:1–15, 2019.

[21] Kasper Van Gasse, Ruijun Wang, and Gunther Roelkens. *27 dB gain III-V-on-silicon semiconductor optical amplifier with 17 dB output power.* Optics Express, 27(1):293–302, 2019.

[22] Tomoyuki Akiyama, Mitsuru Sugawara, and Yasuhiko Arakawa. *Quantum-Dot Semiconductor Optical Amplifiers.* Proceedings of the IEEE, 95(5):1757–1766, 2007.

[23] Richard A. Soref and Brian R. Bennett. *Electrooptical effects in silicon.* IEEE Journal of Quantum Electronics, 23(1):123–129, 1987.

[24] Graham T. Reed and Andrew P. Knights. *Silicon photonics: an introduction chapter.* John Wiley & Sons, Inc., October 2004.

[25] G. T. Reed, G. Mashanovich, F. Y. Gardes, and D. J. Thomson. *Silicon optical modulators.* Nature Photonics, 4:518–526, 2010.

[26] Gorazd Poberaj, Hui Hu, Wolfgang Sohler, and Peter Gunter. *Lithium niobate on insulator (LNOI) for micro-photonic devices.* Laser & Photonics Reviews, 6(4):488–503, 2012.

[27] Andrew J. Mercante, Shouyuan Shi, Peng Yao, Linli Xie, Robert M. Weikle, and Dennis W. Prather. *Thin film lithium niobate electro-optic modulator with terahertz operating bandwidth.* Optics Express, 26(11):14810–14816, 2018.

[28] Cheng Wang, Mian Zhang, Xi Chen, Maxime Bertrand, Amirhassan Shams-Ansari, Sethumadhavan Chandrasekhar, Peter Winzer, and Marko Lončar. *Integrated lithium niobate electro-optic modulators operating at CMOS-compatible voltages.* Nature, 562:101–106, 2018.

[29] Koen Alexander, John P. George, Jochem Verbist, Kristiaan Neyts, Bart Kuyken, Dries Van Thourhout, and Jeroen Beeckman. *Nanophotonic Pockels modulators on a silicon nitride platform.* Nature Communication, 9:3444:1–6, 2018.

[30] S. Lischke, A. Peczek, J. S. Morgan, K. Sun, D. Steckler, Y. Yamamoto, F. Korndörfer, C. Mai, S. Marschmeyer, M. Fraschke, A. Krüger, A. Beling, and L. Zimmermann. *Ultra-fast germanium photodiode with 3-dB bandwidth of 265GHz.* Nature Photonics, 15:925–931, 2021.

[31] Ying Xue, Yu Han, Yi Wang, Jie Li, Jingyi Wang, Zunyue Zhang, Xinlun Cai, Hon Ki Tsang, and Kei May Lau. *High-speed and low dark current silicon-waveguide-coupled III-V photodetectors selectively grown on SOI*. Optica, 9(11):1219–1226, 2022.

[32] Robert Sherbin. *NVIDIA to Acquire Mellanox for $6.9 Billion*. https://nvidianews.nvidia.com/news/nvidia-to-acquire-mellanox-for-6-9-billion#:~:text=Pursuant%20to%20the%20agreement%2C%20NVIDIA,value%20of%20approximately%20%246.9%20billion.

[33] Robert Sherbin. *NVIDIA LinkX Cables and Transceivers*. https://docs.nvidia.com/networking/display/cablemanagfaq/cable+and+conn\ector+definitions,https://www.nvidia.com/en-us/networking/interconnect/.

[34] Robin Holt. *CES 2021: Mobileye Innovation Will Bring AVs to Everyone, Everywhere*. https://www.intc.com/news-events/press-releases/detail/1435/ces-2021-mobileye-innovation-will-bring-avs-to-everyone.

[35] Intel. *Mobileye Autonomous Cars Piloting in Paris*. https://www.intel.com/content/www/us/en/newsroom/news/mobileye-autonomous-cars-piloting-paris.html#gs.b5753g.

[36] *Enjoy a touchless, programmable optical network*. https://www.cisco.com/c/en/us/products/optical-networking/network-convergence-system-2000-series/index.html.

[37] Sicoya GmbH. *SILICON PHOTONIC COMPONENTS*. https://sicoya.com/silicon-photonic-components/#1646379699785-806d9135-cd25.

[38] Martin A. Green, Jianhua Zhao, Aihua Wang, Peter J. Reece, and Michael Gal. *Efficient silicon light-emitting diodes*. Nature, 412:805–808, 2001.

[39] Wai Lek Ng, M. A. Lourenco, R. M. Gwilliam, S. Ledain, G. Shao, and K. P. Homewood. *An efficient room-temperature silicon-based light-emitting diode*. Nature, 410:192–194, 2001.

[40] Yang Liu, Zheru Qiu, Xinru Ji, Andrea Bancora, Grigory Lihachev, Johann Riemensberger, Rui Ning Wang, and Andrey Voloshin Tobias J. Kippenberg. *A fully hybrid integrated erbium-based laser*. Nature Photonics, 18:829–835, 2023.

[41] Yang Liu, Zheru Qiu, Xinru Ji, Anton Lukashchuk, Jijun He, Johann Riemensberger, Martin Hafermann, Rui Ning Wang, Junqiu Liu, Carsten Ronning, and Tobias J. Kippenberg. *A photonic integrated circuit–based erbium-doped amplifier*. Science, 376:1309–1313, 2022.

[42] Rodolfo E. Camacho-Aguilera, Yan Cai, Neil Patel, Jonathan T. Bessette, Marco Romagnoli, Lionel C. Kimerling, and Jurgen Michel. *An electrically pumped germanium laser*. Optics Express, 20(10):11316–11320, 2012.

[43] WS. Wirths, R. Geiger, N. Von Den Driesch, G. Mussler, T. Stoica, S.Mantl, Z. Ikonic, M. Luysberg, S. Chiussi, J. M. Hartmann, H. Sigg, J. Faist, D. Buca1, and D. Grützmacher. *Lasing in direct-bandgap GeSn alloy grown on Si*. Nature Photonics, 9:88–92, 2015.

[44] Yubo Wang, Jorge A. Holguín-Lerma, Mattia Vezzoli, Yu Guo, and Hong X. Tang. *Photonic-circuit-integrated titaniumsapphire laser* . Nature Photonics, 17:338–345, 2022.

[45] Joshua Yang, Kasper Van Gasse, Daniil M. Lukin, Melissa A. Guidry, Geun Ho Ahn, Alexander D. White, and Jelena Vučković. *Titanium-sapphire-on-insulator integrated lasers and amplifiers* . Nature, 1:853–859, 2024.

[46] Yusheng Bian, Koushik Ramachandran, and Bo Peng et. al. *Integrated laser attach technology on a monolithic silicon photonics platform*. 2021. Presentation; 2021 IEEE 71st Electronic Components and Technology Conference (ECTC) ; Conference date: 01-06-2021 Through 04-07-2021.

[47] Shiyun Lin, Xuezhe Zheng, Jin Yao, Stevan S. Djordjevic, John E. Cunningham, Jin-Hyoung Lee, Ivan Shubin, Ying Luo, Jock Bovington, Daniel Y. Lee, Hiren D. Thacker, Kannan Raj, and Ashok V. Krishnamoorthy. *Efficient, tunable flip-chip-integrated III-V/Si hybrid external-cavity laser array*. Optics Express, 24(19):21454–21462, 2016.

[48] K. Mori, K. Tokutome, and S. Sugou. *Low-threshold pulsed operation of long-wavelength lasers on Si fabricated by direct bonding*. Electronics Letters, 31:284–285, 1995.

[49] Alexander W. Fang, Alexander W. Fang, Hyundai Park, Richard Jones, Oded Cohen, Mario J. Paniccia, and John E. Bowers. *A continuous-wave hybrid AlGaInAs-Silicon evanescent laser*. IEEE Photonics Technology Letters, 18(10):1143–1145, 2006.

[50] Hsu-Hao Chang, Alexander W. Fang, Matthew N. Sysak, Hyundai Park, Richard Jones, Oded Cohen, Omri Raday, Mario J. Paniccia, and John E.

Bowers. *1310 nm silicon evanescent laser*. Optics Express, 15(8):11466–11471, 2007.

[51] Intel. *The world's first silicon-based optical data connection with integrated lasers*. https://www.intel.com/content/dam/www/public/us/en/documents/intel-research/Intel_SiliconPhotonics50gLink_FINAL.pdf.

[52] Intel. *Intel demonstrates a tightly controlled eight-wavelength laser array on a silicon wafer with matched power and uniform spacing*. https://www.intc.com/news-events/press-releases/detail/1555/intel-labs-announces-integrated-photonics-research.

[53] Joan Juvert, Tommaso Cassese, Sarah Uvin, Andreas de Groote, Brad Snyder, Lieve Bogaerts, Geraldine Jamieson, Joris Van Campenhout, Günther Roelkens, and Dries Van Thourhout. *Integration of etched facet, electrically pumped, C-band Fabry-Pérot lasers on a silicon photonic integrated circuit by transfer printing*. Optics Express, 26(17):21443–21454, 2018.

[54] Jeroen Goyvaerts, Alexander Grabowski, Johan Gustavsson, Sulakshna Kumari, Andim Stassen, and Roel Baets. *Enabling VCSEL-on-silicon nitride photonic integrated circuits with micro-transfer-printing*. Optica, 8(12):1573–1580, 2021.

[55] Bahawal Haq, Javad Rahimi Vaskasi, Jing Zhang, Agnieszka Gocalinska, Emanuele Pelucchi, Brian Corbett, and Gunther Roelkens. *Micro-transfer-printed III-V-on-silicon C-band distributed feedback lasers*. Optics Express, 28(22):32793–32801, 2020.

[56] Akiyama, Masahiro, Yoshihiro Kawarada, and Katsuzo Kaminishi. *Growth of GaAs on Si by MOVCD*. Journal of Crystal Growth, 68:21–26, 1984.

[57] W. I. Wang. *Molecular beam epitaxial growth and material properties of GaAs and AlGaAs on Si (100)*. Applied Physics Letters, 44(12):1149–1151, 1984.

[58] Kawabe Mitsuo and Toshio Ueda. *Molecular beam epitaxy of controlled single domain GaAs on Si (100)*. Japanese Journal of Applied Physics, 25(4):L285–L287, 1986.

[59] R. Alcotte, M. Martin, J. Moeyaert, R. Cipro, S. David, F. Bassani, F. Ducroquet, Y. Bogumilowicz, E. Sanchez, Z. Ye, X. Y. Bao, J. B. Pin, and T. Baron. *Epitaxial growth of antiphase boundary free GaAs layer on 300 mm Si (001) substrate by metalorganic chemical vapour deposition with high mobility*. APL Materials, 4(4):046101:1–6, 2016.

[60] Hidefumi Mori, Masami Tachikawa, Mitsuru Sugo, and Yoshio ltoh. *GaAs heteroepitaxy on an epitaxial Si surface with a low-temperature process*. Applied Physics Letters, 63(14):1963–1965, 1993.

[61] Kerstin Volz, Andreas Beyer, Wiebke Witte, Jens Ohlmann, Igor Nemeth, Bernardette Kunert, and Wolfgang Stolz. *GaP-nucleation on exact Si (001) substrates for III/V device integration*. Journal of Crystal Growth, 315:37–47, 2011.

[62] Keshuang Li, Junjie Yang, Ying Lu, Mingchu Tang, Pamela Jurczak, Zizhuo Liu, Xuezhe Yu, Jae-Seong Park, Huiwen Deng, Hui Jia, Manyu Dang, Ana M. Sanchez, Richard Beanland, Wei Li, Xiaodong Han, Jin-Chuan Zhang, Huan Wang, Fengqi Liu, Siming Chen, Alwyn Seeds, Peter Smowton, and Huiyun Liu. *Inversion boundary annihilation in GaAs monolithically grown on On-Axis silicon (001)*. Advanced Optical Materials, 8:2000970:1–8, 2020.

[63] Jinkwan Kwoen, Joohang Lee, Katsuyuki Watanabe, and Yasuhiko Arakawa. *Elimination of anti-phase boundaries in a GaAs layer directly-grown on an on-axis Si (001) substrate by optimizing an AlGaAs nucleation layer*. Japanese Journal of Applied Physics 58, 58:SBBE07:1–5, 2019.

[64] Jinkwan Kwoen, Bongyong Jang, Joohang Lee, Takeo Kageyama, Katsuyuki Watanabe, and Yasuhiko Arakawa. *All MBE grown InAs/GaAs quantum dot lasers on on-axis Si (001)*. Optics express, 26(9):11568–11576, 2018.

[65] Zizhuo Liu, Constanze Hantschmann, Mingchu Tang, Ying Lu, Jae-Seong Park, Mengya Liao, Shujie Pan, Ana Sanchez, Richard Beanland, Mickael Martin, Thierry Baron, Siming Chen, Alwyn Seeds, Richard Penty, Ian White, and Huiyun Liu. *Origin of defect tolerance in InAs/GaAs quantum dot lasers grown on silicon*. Journal of Lightwave Technology, 38(2):240–248, 2019.

[66] Akiyama Masahiro, Yoshihiro Kawarada, and Katsuzo Kaminishi. *Growth of single domain GaAs layer on (100)-oriented Si substrate by MOCVD*. Japanese Journal of Applied Physics, 23(11):L843–845, 1984.

[67] Masahiro Akiyama, Yoshihiro Kawarada, Takashi Ueda, Seiji Nishi, and Katsuzo Kaminishi. *Growth of high quality GaAs layers on Si substrates by MOCVD*. Journal of Crystal Growth, 77:490–497, 1986.

[68] Bolkhovityanov, Yu B., and Oleg Petrovich Pchelyakov. *GaAs epitaxy on Si substrates: Modern status of research and engineering*. Physics-Uspekhi, 51(5):437–456, 2008.

[69] Yifan Wang, Qi Wang, Zhigang Jia, Xiaoyi Li, Can Deng, Xiaomin Ren, Shiwei Cai, and Yongqing Huang Wang. *Three-step growth of metamorphic GaAs on Si (001) by low-pressure metal organic chemical vapor deposition*. Journal of Vacuum Science & Technology B, 31(5):051211:1–5, 2013.

[70] Jun Wang, Xiaomin Ren, Can Deng, Yunrui He Haiyang Hu, Zhuo Cheng, Haoyuan Ma, Qi Wang, Yongqing Huang, Xiaofeng Duan, and Xin Yan. *Extremely low-threshold current density InGaAs/AlGaAs quantum-well lasers on silicon*. Journal of Lightwave Technology, 33(15):3163–3169, 2015.

[71] Michael E. Groenert, Christopher W. Leitz, Arthur J. Pitera, Vicky Yang, Harry Lee, Rajeev J. Ram, and Eugene A. Fitzgerald. *Monolithic integration of room-temperature cw GaAs/AlGaAs lasers on Si substrates via relaxed graded GeSi buffer layers*. Journal of Applied Physics, 93(1):362–367, 2003.

[72] David Kohen, Xuan Sang Nguyen, Riko I. Made, Christopher Heidelberger, Kwang Hong Lee, Kenneth Eng Kian Lee, and Eugene A. Fitzgerald. *Preventing phase separation in MOCVD-grown InAlAs compositionally graded buffer on silicon substrate using InGaAs interlayers*. Journal of Crystal Growth, 478:64–70, 2017.

[73] Rowel Go, H. Krysiak, M. Fetters, Pedro Figueiredo, Matthew Suttinger, X. M. Fang, A. Eisenbach, J. M. Fastenau, D. Lubyshev, A. W. K. Liu, N. G. Huy, A. O. Morgan, S. A. Edwards, M. J. Furlong, and Arkadiy Lyakh. *InP-based quantum cascade lasers monolithically integrated onto silicon*. Optics Express, 26(17):22389–22393, 2018.

[74] Shi Bei and Jonathan Klamkin. *Defect engineering for high quality InP epitaxially grown on on-axis (001) Si*. Journal of Applied Physics, 127:033102:1–10, 2020.

[75] J. W. Matthews, A. E. Blakeslee, and S. Mader. *Use of misfit strain to remove dislocations from epitaxial thin films*. Thin Solid Films, 33:253–266, 1976.

[76] M. A. Tischler, T. Katsuyama, N. A. ElMasry, and S. M. Bedair. *Defect reduction in GaAs epitaxial layers using a GaAsP-InGaAs strained-layer superlattice*. Applied Physics Letters, 46(3):294–296, 1985.

[77] S. M. Bedair, T. P. Humphreys, N. A. ElMasry, Y. Lo, N. Hamaguchi, C. D. Lamp, A. A. Tuttle, D. L. Dreifus, and P. Russell. *Defect reduction in GaAs grown by molecular beam epitaxy using different superlattice structures*. Applied Physics Letters, 49(15):942–944, 1986.

[78] G. C. Osbourn, P. L. Gourley, I. J. Fritz, R. M. Biefild, L. R. Dawson, and T. E. Zipperian. *Principles and applications of semiconductor strained-layer superlattices*. Semiconductors and Semimetals, 24:459–503, 1987.

[79] Shi Bei, Qiang Li, and Kei May Lau. *Epitaxial growth of high quality InP on Si substrates: The role of InAs/InP quantum dots as effective dislocation filters*. Journal of Applied Physics, 123(19):193104:1–8, 2018.

[80] Siming Chen, Wei Li, JiangWu, Qi Jiang, Mingchu Tang, Samuel Shutts, Stella N. Elliott, Angela Sobiesierski, Alwyn J. Seeds, Ian Ross, Peter M. Smowton, and Huiyun Liu. *Electrically pumped continuous-wave III-V quantum dot lasers on silicon*. Nature Photonics, 10:307–311, 2016.

[81] Manyu Dang, Huiwen Deng, Suguo Huo, Raghavendra R Juluri, Ana M Sanchez, Alwyn J Seeds, Huiyun Liu, and Mingchu Tang. *The growth of low-threading-dislocation-density GaAs buffer layers on Si substrates*. Journal of Physics D: Applied Physics, 56(40):405108:1–7, 2023.

[82] I. J. Luxmoore, R. Toro1, O. Del Pozo-Zamudio, N. A. Wasley, E. A. Chekhovich, A. M. Sanchez, R. Beanland, A. M. Fox, M. S. Skolnick, H. Y. Liu, and A. I. Tartakovskii. *III–V quantum light source and cavity-QED on Silicon*. Scientific reports, 3(1239):1–5, 2013.

[83] Eamonn T. Hughes, Gunnar Kusch, Jennifer Selvidge, Bastien Bonef, Justin Norman, hen Shang, John E. Bowers, Rachel A. Oliver, and Kunal Mukherjee. *Dislocation-Induced Structural and Luminescence Degradation in InAs Quantum Dot Emitters on Silicon*. Physica Status Solidi, 220(2300114):1–10, 2023.

[84] Chen Shang, Kaiyin Feng, Eamonn T. Hughes, Andrew Clark, Mukul Debnath, Rosalyn Koscica, Gerald Leake, Joshua Herman, David Harame, Peter Ludewig, Yating Wan, and John E. Bowers. *Electrically pumped quantum-dot lasers grown on 300mm patterned Si photonic wafers*. Light: Science & Applications, 11(299):1–8, 2022.

[85] Justin C. Norman, Daehwan Jung, Zeyu Zhang, Yating Wan, Songtao Liu, Chen Shang, Robert W. Herrick, Weng W. Chow, Arthur C. Gossard, and John E. Bowers. *A Review of High-Performance Quantum Dot Lasers on Silicon*. IEEE Journal Of Quantum Electronics, 59(2):2000511:1–11, 2019.

[86] Jae-Seong Park, Mingchu Tang, Siming Chen, and Huiyun Liu. *Heteroepitaxial growth of III-V semiconductors on silicon*. Crystals, 10:1163:1–36, 2020.

[87] Zaman Iqbal Kazi, Periyasamy Thilakan, Takashi Egawa, Masayoshi Umeno, and Takashi Jimbo. *Realization of GaAs/AlGaAs lasers on Si substrates using epitaxial lateral overgrowth by metalorganic chemical vapor deposition*. Japanese Journal of Applied Physics, 40(8):4903–4906, 2001.

[88] Yoshinobu Kawaguchi, Kentaro Murakawa, Motohisa Usagawa, Yuuta Aoki, Kazuma Takeuchi, and Takeshi Kamikawa. *100 μm-cavity GaN-based edge emitting laser diodes by the automatic cleavage technique using GaN-on-Si epitaxial lateral overgrowth*. Crystal Growth & Design, 23:3572–3578, 2023.

[89] Plessey. *Plessey Releases Single Chip High Power 7070 LEDs*. https://www.led-professional.com/products/leds_led_modules/plessey-releases-single-chip-high-power-7070-leds.

[90] Plessey. *Plessey produces a GaN-on-Silicon four-megapixel microLED display with a 2.5-micron pixel pitch*. https://www.ebom.com/plessey-produces-a-gan-on-silicon-four-megapixel-microled-display-with-a-2-5-micron-pixel-pitch-2/.

[91] H. Schmid, M. Borg, K. Moselund, L. Gignac, C. M. Breslin, J. Bruley, D. Cutaia, and H. Riel. *Template-assisted selective epitaxy of III-V nanoscale devices for co-planar heterogeneous integration with Si*. Applied Physics Letters, 106:233101:1–5, 2015.

[92] Stephan Wirths, Benedikt F. Mayer, Heinz Schmid, Marilyne Sousa, Johannes Gooth, Heike Riel, and Kirsten E. Moselund. *Room-temperature lasing from monolithically integrated GaAs microdisks on silicon*. ACS Nano, 12:2169–2175, 2018.

[93] S. Mauthe, B. Mayer, M. Sousa, G. Villares, P. Staudinger, H. Schmid, and K. Moselund. *Monolithically integrated InGaAs microdisk lasers on silicon using template-assisted selective epitaxy*. May 2018. Presentation; SPIE Photonics Europe, 2018 ; Conference date: 15-04-2018 Through 18-04-2018.

[94] Preksha Tiwari, Anna Fischer, Svenja Mauthe, Enrico Brugnolotto, Noelia Vico Triviño, Marilyne Sousa, Daniele Caimi, Heinz Schmid, and Kirsten E. Moselund. *InGaAs microdisk cavities monolithically integrated on Si with room temperature emission at 1530 nm*. 2021. Presentation; The European Conference on Lasers and Electro-Optics, 2021 ; Conference date: 21-06-2021 Through 25-06-2021.

[95] Bernardette Kunert, Yves Mols, Marina Baryshniskova, Niamh Waldron, Andreas Schulze, and Robert Langer. *How to control defect formation in monolithic III/V hetero-epitaxy on (100) Si? A critical review on current approaches*. Semiconductor Science and Technology, 33:093002:1–20, 2018.

[96] Qiang Li and Kei May Lau. *Epitaxial growth of highly mismatched III-V materials on (001) silicon for electronics and optoelectronics.* Progress in Crystal Growth and Characterization of Materials, 63:105–120, 2017.

[97] Tommaso Orzali, Alexey Vert, Brendan O'Brien, Joshua L. Herman, Saikumar Vivekanand, Richard J. W. Hill, Zia Karim, and Satyavolu S. Papa Rao. *GaAs on Si epitaxy by aspect ratio trapping: Analysis and reduction of defects propagating along the trench direction.* Journal of Applied Physics, 118:105307:1–9, 2015.

[98] Yu Han, Wai Kit Ng, Ying Xue, Qiang Li, Kam Sing Wong, and Kei May Lau. *Telecom InP/InGaAs nanolaser array directly grown on (001) silicon-on-insulator.* Optics Letters, 44(4):767–770, 2019.

[99] Ying Xue, Jie Li, Yi Wang, Ke Xu, Zengshan Xing, Kam Sing Wong, Hon Ki Tsang, and Kei May Lau. *In-plane 1.5 μm distributed feedback lasers selectively grown on (001) SOI.* Laser & Photonics Reviews, 18:2300549:1–8, 2024.

[100] Yu Han, Ying Xue, and Kei May Lau. *Selective lateral epitaxy of dislocation-free InP on silicon-on-insulator.* Applied Physics Letters, 114:192105:1–5, 2019.

[101] Yong Du, Buqing Xu, Guilei Wang, Yuanhao Miao, Ben Li, Zhenzhen Kong, Yan Dong, Wenwu Wang, and Henry H. Radamson. *Review of highly mismatched III-V heteroepitaxy growth on (001) silicon.* Nanomaterials, 12:741:1–46, 2022.

[102] Bernardette Kunert, Robert Langer, Marianna Pantouvaki, Joris Van Campenhout, and Dries Van Thourhout. *Gaining an edge with nano-ridges.* Compound Semiconductor, 24(5):36–41, 2018.

[103] Yuting Shi, Zhechao Wang, Joris Van Campenhout, Marianna Pantouvaki, Weiming Guo, Bernardette Kunert, and Dries Van Thourhout. *Optical pumped InGaAs/GaAs nano-ridge laser epitaxially grown on a standard 300-mm Si wafer.* Optica, 4(12):1468–1473, 2017.

[104] Yuting Shi, Marianna Pantouvaki, Joris Van Campenhout, Davide Colucci, Marinab Aryshnikova, Bernardette Kunert, and Dries Van Thourhout. *Loss-coupled DFB nano-ridge laser monolithically grown on a standard 300-mm Si wafer.* Optics Express, 29(10):14649–14657, 2021.

[105] Davide Colucci, Marina Baryshnikova, Yuting Shi, Yves Mols, Muhammad Muneeb, Yannick De Koninck, Didit Yudistira, Marianna Pantouvaki, Joris Van Campenhout, Robert Langer, Dries Van Thourhout, and Bernardette

Kunert. *Unique design approach to realize an O-band laser monolithically integrated on 300 mm Si substrate by nano-ridge engineering*. Optics Express, 30(8):13510–13521, 2022.

[106] Y. Mols, J. Bogdanowicz, P. Favia, P. Lagrain, W. Guo, H. Bender, and B. Kunert. *Structural analysis and resistivity measurements of InAs and GaSb fins on 300 mm Si for vertical (T) FET*. Journal of Applied Physics, 125:245107:1–10, 2019.

[107] Marina Baryshnikova, Yves Mols, Yoshiyuki Ishii, Reynald Alcotte, Han Han, Thomas Hantschel, Olivier Richard, Marianna Pantouvaki, Joris Van Campenhout, Dries Van Thourhout, Robert Langer, and Bernardette Kunert. *Nano-ridge engineering of GaSb for the integration of InAs/GaSb heterostructures on 300 mm (001) Si*. Crystals, 10:330:1–19, 2020.

[108] Bernardette Kunert, Weiming Guo, Yves Mols, Bing Tian, Zhechao Wang, Yuting Shi, Dries Van Thourhout, Marianna Pantouvaki, Joris Van Campenhout, Robert Langer, and K. Barla. *III/V nano ridge structures for optical applications on patterned 300 mm silicon substrate*. Applied Physics Letters, 109(9):091101:1–5, 2016.

[109] Yuting Shi, Bernardette Kunert, Yannick De Koninck, Marianna Pantouvaki, Joris Van Campenhout, and Dries Van Thourhout. *Novel adiabatic coupler for III-V nano-ridge laser grown on a Si photonics platform*. Optics Express, 27(26):37781–37794, 2019.

[110] Si Zhu, Bei Shi, Qiang Li, and Kei May Lau. *Room-temperature electrically-pumped 1.5 μm InGaAs/InAlGaAs laser monolithically grown on on-axis (001) Si*. Optics Express, 26(11):14514–14523, 2018.

[111] Yuting Shi, Lisa C. Kreuzer, Nils C. Gerhardt, Marianna Pantouvaki, Joris Van Campenhout, Marina Baryshnikova, Robert Langer, Dries Van Thourhout, and Bernardette Kunert. *Time-resolved photoluminescence characterization of InGaAs/GaAs nano-ridges monolithically grown on 300 mm Si substrates*. Journal of Applied Physics, 127(10):1–8, 2020.

[112] Timothy H Gfroerer. *Photoluminescence in analysis of surfaces and interfaces, Encyclopedia of analytical chemistry: applications, theory and instrumentation*. 67:3810:1–20, 2006.

[113] Yuting and Shi. *GaAs Nano-Ridge Lasers Epitaxially Grown on Silicon*. PhD thesis, Universiteit Gent, 2020.

[114] James Clerk Maxwell. *The Scientific Papers of James Clerk Maxwell*. Dover publications, INC, November 2013.

[115] *Lumerical official website*. https://www.lumerical.com.

[116] *Chegg*. https://www.chegg.com/homework-help/questions-and-answers/etch-rate-silicon-depends-orientation-type-concentration-wet-etching-solution-temperature--q52964255.

[117] Ning and Cun-Zheng. *What is laser threshold*. IEEE Journal of Selected Topics in Quantum Electronics, 19(4):1503604–1503604, 2013.

[118] Yokoyama H. and S. D. Brorson. *Rate equation analysis of microcavity lasers*. Journal of Applied Physics, 66(10):4801–4805, 1989.

[119] Shore K. A. and M. Ogura. *Threshold characteristics of microcavity semiconductor lasers*. Optical and Quantum Electronics, 24:S209–S213, 1992.

[120] Zhechao Wang, Bin Tian, Marianna Pantouvaki, Weiming Guo, Philippe Absil, Joris Van Campenhout, Clement Merckling, and Dries Van Thourhout. *Room-temperature InP distributed feedback laser array directly grown on silicon*. Nature Photonics, 9(12):837–842, 2015.

[121] Bin Tian, Zhechao Wang, Marianna Pantouvaki, Philippe Absil, Joris Van Campenhout, Clement Merckling, and Dries Van Thourhout. *Room temperature O-band DFB laser array directly grown on (001) silicon*. Nano letters, 17(1):559–564, 2017.

[122] Yu Han, Wai Kit Ng, Ying Xue, Kam Sing Wong, and Kei May Lau. *Room temperature III–V nanolasers with distributed Bragg reflectors epitaxially grown on (001) silicon-on-insulators*. Photonics Research, 7(9):1081–1086, 2019.

[123] Yu Han, Zhao Yan, Wai Kit Ng, Ying Xue, Kam Sing Wong, and Kei May Lau. *Bufferless 1.5 µm III-V lasers grown on Si-photonics 220 nm silicon-on-insulator platforms*. Optica, 7(2):148–153, 2020.

[124] G. Morthier and P. Vankwikelberge. *Handbook of Distributed Feedback Laser Diodes*. Artech House., 2013.

[125] Yannick De Koninck, Charles Caer, Didit Yudistira, Marina Baryshnikova1, Huseyin Sar, Ping-Yi Hsieh, Cenk Ibrahim Özdemir, Saroj Kanta Patra, Nadezda Kuznetsova, Davide Colucci, Alexey Milenin, Andualem Ali Yimam, Geert Morthier, Dries Van Thourhout, Peter Verheyen, Marianna Pantouvaki, Bernardette Kunert, and Joris Van Campenhout. *GaAs nano-ridge laser diodes fully fabricated in a 300-mm CMOS pilot line*. Nature, 637:63–89, 2025.

[126] Bernardette Kunert, Reynald Alcotte, Yves Mols, Marina Baryshnikova, Niamh Waldron, Nadine Collaert, and Robert Langer. *Application of an Sb Surfactant in InGaAs Nano-ridge Engineering on 300 mm Silicon Substrates.* Crystal Growth and Design, 21:1657–1665, 2021.

[127] Yoshinori Tanaka, Takashi Asano, and Susumu Noda. *Design of Photonic Crystal Nanocavity With Q-Factor of* 10^9. Journal of Lightwave Technology, 26(11):1532–1539, 2008.

[128] Kartik Srinivasan and Oskar Painter. *Momentum space design of high-Q photonic crystal optical cavities.* Optics Express, 10(15):670–684, 2002.

[129] Yoshihiro Akahane, Takashi Asano, Bong-Shik Song, and Susumu Noda. *High-Q photonic nanocavity in a two-dimensional photonic crystal.* Nature, 425:944–947, 2003.

[130] Byeong-Hyeon Ahn, Ju-Hyung Kang, Myung-Ki Kim, Jung-Hwan Song, Bumki Min, Ki-Soo Kim, and Yong-Hee Lee. *One-dimensional parabolic-beam photonic crystal laser.* Optics Express, 18(6):5654–5660, 2010.

[131] M. Notomi, E. Kuramochi, and H. Taniyama. *Ultrahigh-Q nanocavity with 1D photonic gap.* Optics Express, 16(15):11095–11102, 2008.

[132] Eiichi Kuramochi, Hideaki Taniyama, Takasumi Tanabe, Kohei Kawasaki, Young-Geun Roh, and Masaya Notomi. *Ultrahigh-Q one-dimensional photonic crystal nanocavities with modulated mode-gap barriers on* SiO_2 *claddings and on air claddings.* Optics express, 18(15):15859–15869, 2010.

[133] Qimin Quan, Parag B. Deotare, and Marko Loncar. *Photonic crystal nanobeam cavity strongly coupled to the feeding waveguide.* Applied Physics Letters, 96:203102:1–4, 2010.

[134] E. Yablonovitch, C. J. Sandroff, R. Bhat, and T. Gmitter. *Nearly ideal electronic properties of sulfide coated GaAs surfaces.* Applied Physics Letters, 51(6):439–441, 1987.

[135] Yasuo Nannichi, Jia fa Fan, Haruhiro Oigawa, and Atsushi Koma. *A model to explain the effective passivation of the GaAs surface by* $(NH_4)_2S_x$ *treatment.* Japanese Journal of Applied Physics, 27(12):L2367, 1988.

[136] Haruhiro Oigawa, Jia-Fa Fan, Yasuo Nannichi, Koji Ando, Koichiro Saiki, and Atsushi Koma. *Studies on an* $(NH_4)_2S_x$*-treated GaAs surface using AES, LEELS and RHEED.* Japanese Journal of Applied Physics, 28(3):L340, 1989.

[137] Haruhiro Oigawa, Jia-Fa Fan, Yasuo Nannichi, Hirohiko Sugahara, and Masaharu Oshima. *Universal passivation effect of* $(NH_4)_2S_x$ *treatment on the surface of III-V compound semiconductors*. Japanese Journal of Applied Physics, 30(3):L322, 1991.

[138] W. C. Dautremont-Smith, J. C. Nabity, V. Swaminathan, Michael Stavola, J. Chevallier, C. W. Tu, and S. J. Pearton. *Passivation of deep level defects in molecular beam epitaxial GaAs by hydrogen plasma exposure*. Applied Physics Letters, 49:1098–1100, 1986.

[139] K. K. Ko and S. W. Pang. *Plasma passivation of etch-induced surface damage on GaAs*. Journal of Vacuum Science & Technology B, 13:2376–2380, 1995.

[140] Hanlin Fu, Wei Sun, Onoriode Ogidi-Ekoko, Justin C. Goodrich, and Nelson Tansu. *Gain characteristics of InGaN quantum wells with AlGaInN barriers*. AIP Advances, 9(045013):1–7, 2019.

[141] Peng Zhang, Yanrong Song, Jinrong Tian, Xinping Zhang, and Zhigang Zhang. *Gain characteristics of the InGaAs strained quantum wells with GaAs, AlGaAs, and GaAsP barriers in vertical-external-cavity surface-emitting lasers*. Journal Of Applied Physics, 105(053103):1–8, 2009.

[142] Gene Tsvid, Jeremy Kirch, Luke J. Mawst, Manoj Kanskar, Jason Cai, Ronald A. Arif, Nelson Tansu, Peter M. Smowton, and Peter Blood. *Spontaneous Radiative Efficiency and Gain Characteristics of Strained-Layer InGaAs–GaAs Quantum-Well Lasers*. IEEE Journal Of Quantum Electronics, 44(8):732–739, 2008.

[143] H. Carrère, X. Marie, L. Lombez, and T. Amand. *Optical gain of InGaAsN-InP quantum wells for laser applications*. Applied Physics Letters, 89(181115):1–3, 2006.

[144] Lingling Hua, Heyang Guoyu, Peng Zhang, Jinrong Tian, and Yanrong Song. *Theoretical analysis of band structure and material gain of InGaAs quantum wells in a semiconductor disk laser*. 2018. Presentation; 2018 The International Society for Optics and Photonics (SPIE) ; Conference date: 24-04-2018 Through 25-04-2018.

[145] S.G.Anjum, M.J.Siddiqui, A.B.Khan, and M.M.Singh. *Investigation of Material Gain of InGaAs-InGaAsP-InP Lasing Heterostructure*. 2016. Presentation; 2016 International Conference on Microelectronics, Computing and Communications (MicroCom); Conference date: 23-01-2016 Through 25-01-2016.

[146] Sheng-Horng Yen, Mei-Ling Chen, and Yen-Kuang Kuo. *Gain and threshold properties of InGaAsN-GaAsN material system for 1.3-mm semiconductor lasers.* Optics & Laser Technology, 39:1432–1436, 2007.

[147] Nikita Yu Gordeev, Mikhail V Maximov, Alexey S Payusov, Artem A Serin, Yuri M Shernyakov, Sergey A Mintairov, Nikolay A Kalyuzhnyy, Alexey M Nadtochiy, and Alexey E Zhukov. *Material gain of InGaAs-GaAs quantum well-dots.* Semiconductor Science and Technology, 36(015008):1–5, 2020.

[148] M Maximov, N Gordeev, A Payusov, Yu Shernyakov, S Mintairov, N Kalyuzhnyy, M Kulagina, A Nadtochiy, V Nevedomskiy, and A Zhukov. *Modification of InGaAs-GaAs heterostructure density of states and optical gain using hybrid quantum well-dots* . Laser Physics Letters, 17(095801):1–4, 2020.

[149] Nikolay Baidus, Vladimir Aleshkin, Alexander Dubinov, Konstantin Kudryavtsev, Sergei Nekorkin, Alexey Novikov, Dmiriy Pavlov, Artem Rykov, Artem Sushkov, Mikhail Shaleev, Pavel Yunin, Dmitriy Yurasov, and Zakhariy Krasilnik. *MOCVD Growth of InGaAs/GaAs/AlGaAs Laser Structures with Quantum Wells on Ge-Si Substrates.* Crystals, 8(311):1–16, 2018.

[150] Bei Shi, Hongwei Zhao, Lei Wang, Bowen Song, Simone Tommaso Suran Brunelli, and Jonathan Klamkin. *Continuous-wave electrically pumped 1550 nm lasers epitaxially grown on on-axis (001) silicon.* Optica, 6(12):2334–2536, 2019.

[151] Ping-Yi Hsieh, Barry O'Sullivan, Artemisia Tsiara, Brecht Truijen, Pieter Lagrain, Lennaert Wouters, Didit Yudistira, Bernardette Kunert, Joris Van Campenhout, and Ingrid De Wolf. *Advanced Current–Voltage Model of Electrical Contacts to GaAs- and Ge-Based Active Silicon Photonic Devices.* IEEE Transactions On Electron Devices, 70(8):4274–4279, 2023.

[152] Ping-Yi Hsieh, Artemisia Tsiara, Barry O'Sullivan, Anjanashree MR Sharma, David Coenen, Didit Yudistira, Bernardette Kunert, Joris Van Campenhout, and Ingrid De Wolf. *Degradation Mechanisms of Monolithic GaAs-on-Si Nano-Ridge Quantum Well Lasers.* IEEE Journal of Lightwave Technology, 2025.

[153] Ping-Yi Hsieh, Artemisia Tsiara, Barry O'Sullivan, Didit Yudistira, Marina Baryshnikova, Guido Groeseneken, Bernardette Kunert, Marianna Pantouvaki, Joris Van Campenhout, and Ingrid De Wolf. *Wafer-Level Aging of InGaAs/GaAs Nano-Ridge p-i-n Diodes Monolithically Integrated on Silicon.* 2022. Presentation; 2022 IEEE International Reliability Physics Symposium (IRPS); Conference date: 27-03-2022 Through 31-03-2022.

[154] Ping-Yi Hsieh, Artemisia Tsiara, Barry O'Sullivan, Sara El Akel, Huseyin Sar, Debi Prasad Panda, Peter Swekis, Didit Yudistira, Bernardette Kunert, Joris Van Campenhout, and Ingrid De Wolf. *Lifetime Model for Enabling Reliable InGaAs/GaAs Nano-Ridge Lasers Monolithically Integrated on 300 mm Silicon*. 2022. Presentation; Optical Fiber Communication Conference (OFC) 2025; Conference date: 30-03-2025 Through 03-04-2025.

[155] Chunyi Huang, Didem Dede, Nicholas Morgan, Valerio Piazza, Xiaobing Hu, Anna Fontcuberta i Morral, and Lincoln J. Lauhon. *Trapping Layers Prevent Dopant Segregation and Enable Remote Doping of Templated Self-Assembled InGaAs Nanowires*. Nano Letters, 23:6284–6291, 2023.

[156] Ayse Ozcan-Atar, Agnieszka Gocalinska, Paweł P. Michałowski, Mack Johnson, John O'Hara, Brian Corbett, Adrianna Rejmer, Frank Peters, Dimitri D. Vvedensky, Andrew Zangwill, Gediminas Juska, and Emanuele Pelucchi. *Why Zn diffusion is not always diffusion Surface physics and a 40-year-old epitaxy problem*. Applied Surface Science, 688(162360):1–12, 2025.

[157] Emlyn Huw Rhoderick. *Metal-semiconductor contacts*. IEE Proceedings I-Solid-State and Electron Devices, 129(1):1, 1982.

[158] J. L. Regolini, S. Bodnar, J. C. Oberlin, F. Ferrieu, M. Gauneau, B. Lambert, and P. Boucaud. *Strain compensated heterostructures in the $Si_{1-x-y}Ge_xC_y$ ternary system*. Journal of Vacuum Science & Technology A: Vacuum, Surfaces and Films, 12(4):1015–1019, 1994.

[159] Lars Samuelson. *Self-forming nanoscale devices*. Materials today, 6(10):22–31, 2003.

[160] Liu A Y and Bowers J. *Photonic integration with epitaxial III–V on silicon*. Journal of Selected Topics in Quantum Electronics, 24(6):1–12, 2018.

[161] D. J. Norris, Al. L. Efros, M. Rosen, and M. G. Bawendi. *Size dependence of exciton fine structure in CdSe quantum dots*. Physical Review B, 53(24):16347–16354, 1996.